Advancing Calibrated Functional MRI Through Biophysical Signal Modelling

Avery J.L. Berman, M.Sc.
Department of Biomedical Engineering
McGill University, Montréal

June 2017

A thesis submitted to McGill University in partial fulfillment of the requirements of the degree of Doctor of Philosophy

Contents

List of Figures

List of Tables

Abstract

THIS thesis presents novel theoretical modelling and experimental studies of the biophysics of blood oxygenation level-dependent (BOLD) functional magnetic resonance imaging (fMRI) with the central aim of advancing calibrated fMRI. Calibrated fMRI is an imaging technique that measures the changing hemodynamic and metabolic factors that contribute to the BOLD signal, and is reliant on a preliminary calibration procedure that uses hypercapnic or hyperoxic gas challenges. However, the need for specialized gas delivery and monitoring equipment and associated biophysical confounds of the gas challenges have hampered the widespread adoption of calibrated fMRI. One such confound is the magnetic susceptibility of dissolved oxygen, which, like deoxyhemoglobin, is paramagnetic. A theoretical model for calculating the susceptibility of dissolved oxygen in blood was derived and experimentally validated in ex vivo plasma samples, showing excellent agreement between theory and measurement. These findings indicate that the susceptibility of dissolved oxygen has a negligible contribution to the overall susceptibility of blood and are consistent with deoxyhemoglobin being the predominant source of contrast during hyperoxic BOLD studies.

Intravascular signal is known to significantly contribute to the BOLD signal, however, it is difficult to incorporate into BOLD signal simulations due to the vast number of red blood cells

in vessels. To address this, a model to describe intravascular signal evolution during free induction decay, a spin echo sequence, or a multi-echo spin echo sequence was derived using a validated analytical model of diffusion-induced decay in weak field inhomogeneities. The derived model was in excellent agreement with simulations under a range of conditions including field offset strength, inhomogeneity extent, and pulse sequence. With its ability to accurately predict the full dephasing and refocusing time course of blood, this model could be applied to better understand intravascular BOLD effects, including during gas-free calibration, and more general blood relaxation properties.

Finally, a gas challenge-free alternative to fMRI calibration was investigated. This was based on measuring the reversible component of signal decay resulting from the field inhomogeneities surrounding deoxygenated blood vessels. Simulations showed that diffusion in the extravascular space resulted in an underestimation of the calibration constant of approximately 15–40%, depending on the underlying vessel-size distribution. A method for characterizing and correcting this underestimation was proposed and validated in silico and in vivo. This work could greatly simplify calibrated fMRI by removing the need for a gas challenge.

Résumé

CETTE thèse présente de nouvelles modélisations théoriques et des études expérimentales de la biophysique du signal qui dépend du niveau de l'oxygénation du sang (BOLD), issu de l'imagerie par résonance magnétique fonctionnelle (IRMf), avec l'objectif central d'avancer l'IRMf calibré. L'IRMf calibré est une technique d'imagerie qui mesure les facteurs hémodynamiques et métaboliques changeants qui contribuent au signal BOLD et repose sur une procédure de calibration préliminaire qui utilise des tests de gaz hypercapniques ou hyperoxiques. Cependant, la nécessité d'un équipement spécialisé de livraison et de surveillance des gaz et des confins biophysiques associés aux tests de gaz, a empêché l'adoption généralisée de l'IRMf calibré. Une des sources de confusion est la susceptibilité magnétique de l'oxygène dissous qui, comme la désoxyhemoglobine, est paramagnétique. Un modèle théorique pour calculer la sensibilité de l'oxygène dissous dans le sang a été dérivé et validé expérimentalement dans des spécimens de plasma ex vivo, démontrant un excellent accord entre la théorie et la mesure. Ces résultats indiquent que la susceptibilité de l'oxygène dissous a une contribution négligeable à la susceptibilité globale du sang et supportent le fait que la désoxyhemoglobine est la principale source de contraste lors des études hyperpoxiques BOLD.

On sait que le signal intravasculaire contribue de manière significative au signal BOLD, mais il est difficile d'incorporer ce signal dans des simulations du signal BOLD en raison du grand nombre de globules rouges dans les vaisseaux. Pour remédier à cela, un modèle pour décrire l'évolution du signal intravasculaire lors de la décroissance d'induction libre, une séquence d'écho de spin ou une séquence d'écho de spin à écho multiples a été dérivée en utilisant un modèle analytique validé de la décroissance du signal par diffusion dans des inhomogénéités de champ magnétique faible. Le modèle dérivé était en excellent accord avec des simulations dans une gamme de conditions, y compris la puissance du champ, l'étendue de l'inhomogénéité et la séquence des impulsions radiofréquences. Avec sa capacité à prédire avec précision le déphasage complet et le recentrage du signal dans le sang, ce modèle pourrait être appliqué pour mieux comprendre les effets intravasculaires BOLD, y compris lors de la calibration sans gaz, et des propriétés plus générales de relaxation du sang.

Enfin, une alternative pour la calibration sans l'utilisation de gaz a été étudiée. Ceci était basé sur la mesure de la composante réversible de la décroissance du signal résultant des inhomogénéités du champ entourant les vaisseaux sanguins désoxygénés. Les simulations ont montré que la diffusion dans l'espace extravasculaire a entraîné une sous-estimation de la constante de calibration d'environ 15 à 40%, selon la distribution de la taille du vaisseau. Une méthode pour caractériser et corriger cette sous-estimation a été proposée et validée en silico et in vivo. Ce travail pourrait simplifier considérablement l'IRFF calibré en supprimant le besoin d'un défi gazeux.

Acknowledgements

THIS Ph.D. has been a cerebral and geographical journey. First and foremost, I would like to thank my supervisor, Dr. Bruce Pike, who has thoughtfully guided me through this. Bruce's passion for research, commitment to his students, and seemingly unlimited knowledge are truly remarkable. Through his inspired mentorship, he showed confidence in me to delve into new scientific problems and the reassurance to see them through.

I am grateful for all my past and present lab mates for their friendship, for encouraging and enabling all of us to do our best work, and for making coming in to work something to look forward to each day. I am thankful for Dr. Erin Mazerolle's devoted efforts nearly single-handedly setting up our new lab in Calgary and for answering so many of my questions on fMRI analyses. Thank you to Dr. Ethan MacDonald for our discussions on the art of programming, for the epic ski adventures, and for introducing me to the WestGrid computing cluster – it was a game-changer. Thank you to Dr. Bec Williams for answering my many questions on analyses and stats and for her dependable Aussie sense of humour. Merci à Ilana Leppert pour sa diligence dans la traduction de mon *Résumé*. And thank you to Yuhan Ma for her sage advice and getting me onto the disc golf course.

This research would not have been possible without the support of the staff at the McConnell Brain Imaging Centre, in Montreal, and the Seaman Family MR Centre, in Calgary. A big thank you, especially to the MR technologists in both cities who were always willing to help with setting up, ensuring subject comfort, answering my questions, and keeping scans running smoothly and with a smile. Given the computational nature of much of this thesis, I am indebted for the support from the I.T. teams at both sites, including Andre Robichaud, Mike Ferreira, Alex Sivitsky, and Sylvain Milot. For helping me get started with EPIC pulse sequence programming and overcoming its hurdles, I would like to thank Drs. Louis Lauzon, Marc Lebel, and Ethan MacDonald. Throughout my degree, the administrative staff across departments and institutions, including Christa Collie, Jennifer Chew, Pina Sorrini, Nancy Abate, Daniel Caron, and Fran Raymond, have always gone above and beyond for their students and made us feel welcomed from day 1. I would also like to thank the members of my supervisory committee, Drs. Amir Shmuel and Louis Collins, for their critical feedback throughout my entire degree that always helped bring perspective to my work.

To my wife, Beth, her unwavering love and support have been a wellspring of energy and motivation for me. For years, she patiently put up with my practice talks and ramblings of gases and simulations. I hope that during our academic pursuits I have been able to give back to her as she has done for me. It is hard to thank my family enough for all their support throughout my degree. They were pivotal in my decision to pursue my academics and have encouraged me throughout with their care packages, phone calls, and visits.

Finally, I would like to acknowledge support from my funding sources, including the Canadian Institutes of Health Research, McGill University, and the Department of Biomedical Engineering.

Preface

This thesis is composed of three original manuscripts of which I am the first author. In the capacity of doctoral student, my contributions towards these manuscripts included development of theoretical concepts, experiment design, design and implementation of the FLAIR-asymmetric spin echo sequence, data acquisition and analyses, and writing of all the manuscripts. The contributions of the co-authors are as follows:

- **G. Bruce Pike, PhD:** As supervisor, Professor Pike provided overall guidance of the Ph.D. project and revised all manuscripts extensively.
- **Yuhan Ma:** Collaborated on phantom design, data acquisition, and revision of the manuscript (Chapter 4).
- **Richard D. Hoge, PhD:** Aided in the development of theoretical concepts (Chapter 4).
- **Erin L. Mazerolle, PhD:** Developed the scanning protocol for the hypercapnia challenge, provided guidance on data analyses, and revision of the manuscript (Chapter 6).
- **M. Ethan MacDonald, PhD:** Provided guidance with pulse sequence programming and data analyses, and assisted with data acquisition and revision of the manuscript (Chapter 6).
- **Nicholas P. Blockley, PhD:** Provided guidance on experimental design, analyses, and revision of the manuscript (Chapter 6).

- **Wen-Ming Luh, PhD:** Developed the pseudo-continuous arterial spin labelling pulse sequence (Chapter 6).

Other Publications

Below is a list of other peer-reviewed publications and conference abstracts that were produced over the course of this project but were not included in this thesis.

Papers

i. ME MacDonald, RJ Williams, ND Forkert, AJL Berman, CR McCreary, R Frayne, and GB Pike. Inter-Database Variability in Cortical Thickness Measurements. *Cerebral Cortex*, Submitted.

ii. ME MacDonald, AJL Berman, EL Mazerolle, RJ Williams, GB Pike. Modelling the dynamic passage of oxygen to estimate cerebral blood flow, volume and mean transit time. *NeuroImage*, Under Review.

iii. Y Ma, AJL Berman, and GB Pike. The effect of dissolved oxygen on the relaxation rates of blood plasma: Implications for hyperoxia calibrated BOLD. *Magnetic Resonance in Medicine*, 76(6):1905–11, 2016.

Conference Abstracts

i. AJL Berman, EL Mazerolle, ME MacDonald, NP Blockley, W-M Luh, and GB Pike. Correcting for imperfect spin echo refocusing in gas-free fMRI calibration. *Proceedings of the 25th Scientific Meeting of the International Society of Magnetic Resonance in Medicine*, Honolulu, 2017.

ii. ME MacDonald, RJ Williams, ND Forkert, AJL Berman, CR McCreary, R Frayne, and GB Pike. Consistency of Inter-Database Cortical Thinning with Age. *Proceedings of the 25th Scientific Meeting of the International Society of Magnetic Resonance in Medicine*, Honolulu, 2017.

iii. MG Bright, EL Mazerolle, O Sobczyk, AP Fan, MJP van Osch, CI Mark, L Huber, AJL Berman, DP Bulte, GB Pike, CJ Gauthier, and NP Blockley. Clinical mapping of cerebrovascular reactivity using MRI: a framework for reaching consensus. *Proceedings of the 25th Scientific Meeting of the International Society of Magnetic Resonance in Medicine*, Honolulu, 2017.

iv. EL Mazerolle, M McLean, RJ Williams, AJL Berman and GB Pike. Revisiting the effect of visual attention on the flow-metabolism ratio. *Proceedings of the 22nd Scientific Meeting of the Organization for Human Brain Mapping*, Geneva, 2016.

v. AJL Berman and GB Pike. Breaking β: Understanding the β-value in calibrated functional MRI. *Proceedings of the 24th Scientific Meeting of the International Society of Magnetic Resonance in Medicine*, Singapore, 2016.

vi. AJL Berman and GB Pike. A general solution for transverse signal decay under the weak field approximation: Theory and validation with spherical perturbers. *Proceedings of the 24th Scientific Meeting International Society of the Magnetic Resonance in Medicine*, Singapore, 2016.

vii. ME MacDonald, AJL Berman, EL Mazerolle, RJ Williams, GB Pike. Modeling resting cerebral perfusion from BOLD signal dynamics during hyperoxia. *Proceedings of the 24th Scientific Meeting of the International Society of Magnetic Resonance in Medicine*, Singapore, 2016.

viii. ME MacDonald, AJL Berman, RJ Williams, EL Mazerolle, GB Pike. Blood oxygenation level dependent (BOLD)-quantitative susceptibility mapping (QSM) with different head orientations. *Proceedings of the 23rd Scientific Meeting of the International Society of Magnetic Resonance in Medicine*, Toronto, 2015.

ix. AJL Berman, Y Ma, RD Hoge, GB Pike. The susceptibility of dissolved oxygen. *Proceedings of the 23rd Scientific Meeting of the International Society of Magnetic Resonance in Medicine*, Toronto, 2015.

x. AJL Berman, Y Ma, RD Hoge, GB Pike, The susceptibility of dissolved oxygen: modelling and measurements, *Proceedings of the 2nd Workshop on Imaging Cerebral Physiology: Manipulating Magnetic Resonance Contrast through Respiratory Challenges*, Leipzig, 2014.

xi. Y Ma, AJL Berman, GB Pike. The effect of dissolved oxygen on the relaxation rates of blood plasma. *Proceedings of the 22nd Scientific Meeting of the International Society of Magnetic Resonance in Medicine*, Milan, 2014.

xii. AJL Berman, Y Ma, RD Hoge, GB Pike. The effect of dissolved oxygen on the magnetic susceptibility of blood. *Proceedings of the 2nd Workshop on MRI Phase Contrast & Quantitative Susceptibility Mapping*, Ithaca, NY, 2013.

xiii. AJL Berman, RD Hoge, GB Pike. The impact of dissolved oxygen in blood on hyperoxia-based BOLD calibration. *Proceedings of the 21st of the Scientific Meeting of the International Society of Magnetic Resonance in Medicine*, Salt Lake City, 2013.

List of Abbreviations

ADC	apparent diffusion coefficient
ASE	asymmetric spin echo
ASL	arterial spin labelling
ATP	adenosine triphosphate
BOLD	blood oxygenation level-dependent
CBF	cerebral blood flow
CBV	cerebral blood volume
CFS	closed-form solution (of the weak field approximation)
$CMRO_2$	cerebral metabolic rate of oxygen
C_xO_2	concentration of oxygen in blood, where x is one of a: arterial, v: venous
CPMG	Carr-Purcell-Meiboom-Gill (T_2 relaxometry sequence)
CSF	cerebrospinal fluid
deoxyHb/dHb	deoxyhemoglobin
EPI	echo planar imaging
EV	extravascular
GE	gradient echo
GM	grey matter
Hb	hemoglobin
Hct	hematocrit
IGM	ideal gas model
IV	intravascular
MC	Monte Carlo

MR/MRI	magnetic resonance / magnetic resonance imaging
OEF	oxygen extraction fraction
pO_2	partial pressure of oxygen
q-ASE	quadratic asymmetric spin echo model
RMSE	root mean square error
SD	standard deviation *or* Schwarzbauer and Deichmann (Chapter 4)
SE	spin echo
SNR	signal-to-noise ratio
SO_2	oxygen saturation of hemoglobin
TE	echo time
TI	inversion time
WFA	weak field approximation
WM	white matter
B_0	static magnetic field
D	diffusion coefficient
G_0	mean-square field inhomogeneity (of the weak field approximation)
R_1	longitudinal relaxation rate
R_2^*	apparent transverse relaxation rate
R_2	irreversible (or intrinsic) transverse relaxation rate
R_2'	reversible transverse relaxation rate
$(R_{2,diff})^2$	diffusion-induced transverse decay rate (of the quadratic ASE model)
r_c	characteristic perturber length (of the weak field approximation)
T_1	longitudinal relaxation time
T_2	irreversible (or intrinsic) transverse relaxation time
T_2^*	apparent transverse relaxation time
T_2'	reversible transverse relaxation time
2D	two-dimensional
3D	three-dimensional
α	the blood flow-volume coupling exponent
β	the transverse relaxation rate-susceptibility proportionality exponent
χ	magnetic susceptibility

τ	asymmetric spin echo offset
τ_{180}	CPMG refocusing interval
τ_D	characteristic diffusion time
τ_{ex}	intra-/extra-cellular water exchange lifetime
ω_0	Larmor frequency

Original Contributions

The original scientific contributions made during this Ph.D. project are:

i. Theoretically derived and validated an expression for the susceptibility of dissolved oxygen in blood, showing that dissolved oxygen's impact is negligible and deoxyhemoglobin is the principal contributor to the BOLD signal during hyperoxia. This corrected a previous theoretical claim that dissolved oxygen would significantly impact the BOLD signal during hyperoxia.

ii. Theoretically derived a closed-form solution for transverse signal evolution using the weak field approximation model for diffusion through weak field inhomogeneities. Validated the closed-form solution under various pulse sequences (free induction decay, spin echo, and multi-echo spin echo) against simulations and determined the theoretical range of validity of perturber sizes.

iii. Proposed the closed-form solution above as an analytical model for intravascular signal evolution and validated it against simulations over ranges of volume fractions (i.e. hematocrit) and inhomogeneity strengths (i.e. blood oxygen saturations). Demonstrated, for the first time, how the parameters of the weak field approximation deviate from their analytically predicted values as the volume fraction is increased. Furthermore, showed how this deviation can be predicted empirically, enabling more realistic geometries for red blood cells to be used in future studies.

iv. Using simulations, characterized the attenuation of spin echo and asymmetric spin echo signals resulting from diffusion surrounding the microvasculature. Proposed the

attenuation could be described by a quadratic exponential decay, referred to as the quadratic asymmetric spin echo (q-ASE) model.

v. Demonstrated with simulations and in vivo in healthy subjects that the q-ASE model could be used to correct for the underestimation of the fMRI calibration constant during gas-free calibration using asymmetric spin echo imaging.

Chapter 1

Introduction

MAGNETIC resonance imaging (MRI) is fundamentally impacted by inhomogeneities in the polarizing magnetic field (B_0) at all spatial scales [1]. Inhomogeneities at the *macroscopic* scale span across many imaging voxels and arise from magnet imperfections, gradient and shim coils, and from susceptibility differences between large structures such as air and tissue. Besides some notable exceptions, such as quantitative susceptibility mapping [2], these variations are typically considered a nuisance, resulting in broad areas of signal dropout and geometric distortion, without adding physiological information. At the *microscopic* scale, fluctuations in the magnetic field from atomic and molecular motion result in longitudinal and transverse relaxation [3]. Variations in relaxation across tissues give MRI its vast array of contrasts for tissue identification and are largely responsible for the profound impact MRI has had on medicine [4]. In between, at the *mesoscopic* scale, susceptibility differences in structures smaller than a voxel, such as cells, result in changes in the signal that are dependent on physiological parameters of interest, such as blood volume or trabecular bone structure [5]. Mesoscopic

inhomogeneity has been especially important for the development and understanding of functional MRI (fMRI) based on the blood oxygenation level-dependent (BOLD) signal [6-8]. This manifests itself as inhomogeneities around the red blood cells, directly affecting intravascular water, and as inhomogeneities surrounding vessels, affecting extravascular water, with both intra and extravascular compartments known to significantly impact the BOLD signal [9,10].

The use of the BOLD signal to map regions of correlated neural activity has become ubiquitous in cognitive neurosciences. The BOLD signal is sensitive to the volume of blood in tissue and the concentration of paramagnetic deoxyhemoglobin in blood [11]; the latter being determined by the balance of oxygen delivered through blood flow and the oxygen consumed by oxidative metabolism. Upon stimulation, changes in neural activity are accompanied by increases in cerebral blood flow and metabolism [12-15]. Thus, the BOLD signal is an indirect and qualitative measure of neural activity and is very sensitive to the flow-metabolism relationship.

Calibrated fMRI is an imaging method used to disentangle and quantify the metabolic and hemodynamic changes inherent in standard BOLD fMRI [15]. This has made it a powerful tool for comparing functional responses across groups where vascular or metabolic physiology may differ, such as in aging or neurovascular diseases [16]. However, current fMRI calibration methods require gas challenges that use specialized gas delivery and monitoring equipment that can be time consuming to set up and administer and uncomfortable for the subject. Furthermore, intravascular signal is often ignored in biophysical models and simulations of the BOLD signal, including calibrated fMRI [15,17,18]. One reason for this is that, currently, there is no satisfactory model for incorporating intravascular signal into simulations in a way that is computationally tractable and that can accurately describe the dephasing and refocusing of blood signal during gradient echo or spin echo sequences [19,20].

One common gas challenge for calibrated fMRI is the inhalation of oxygen enriched air (inducing hyperoxia) [21,22]. This method has come under scrutiny recently due to a study suggesting that the concentration of dissolved oxygen in *arterial* blood plasma is sufficiently high during hyperoxia to significantly alter the magnetic susceptibility of blood and, as a result, the BOLD signal [23]. This is in contradiction to the conventional assumption that only changes in the concentration of deoxyhemoglobin in *venous* blood lead to BOLD signal differences during hyperoxia. The objectives of this thesis, therefore, are:

1. To determine how dissolved oxygen in blood affects hyperoxia-based BOLD fMRI studies, such as fMRI calibration.
2. To derive an analytical signal model that can describe the complete transverse signal evolution from blood under gradient echo, spin echo, and multi-echo sequences.
3. To simplify calibrated fMRI by developing a calibration technique that does not require a gas inhalation experiment.

To achieve these objectives, BOLD relaxation properties were studied using analytical signal models and simulations. Where advancements in the theoretical models were made, an emphasis was placed on using experiments to validate their predictions or demonstrate their proof-of-principle. In all, it is hoped that this work underscores the role that analytical modelling and simulations can play in improving our understanding of the biophysics of the BOLD signal and in guiding imaging strategies to probe brain physiology.

This thesis is composed of three manuscripts and is laid out as follows. The thesis begins with a review of the relevant literature in Chapter 2, including background on cerebral physiology, the BOLD effect, and intravascular signal modelling. Chapter 3 describes the simulation

methodology used in the thesis, including its development and its implementation. To address the controversy surrounding the effect of dissolved oxygen on BOLD fMRI, oxygen's susceptibility in blood is theoretically derived and experimentally validated. Chapter 4 presents this work and is a paper published in *Magnetic Resonance in Medicine* (Vol. 75(1):363–71). Chapter 5 presents an extended analytical model for intravascular signal evolution that can be applied to simplifying the calculation of intravascular signal in BOLD simulations or to fitting experimental relaxometry data. This chapter is a manuscript prepared for submission to *Journal of Magnetic Resonance*. Amongst other applications in this thesis, the simulations gave useful insights into gas-free calibration and the quantification of the reversible transverse relaxation rate, R_2', where earlier studies performing this were unable to address the impact of diffusion-induced loss of phase coherence [24-28]. In Chapter 6, an empirical signal model, based on the simulation results, is proposed for gas-free calibration and is compared against conventional hypercapnia-based calibration techniques in vivo. This chapter is a manuscript that has been submitted to *NeuroImage*. Finally, Chapter 7 discusses the overall thesis outcomes and areas of future work.

Chapter 2

Background

FUNCTIONAL MRI (fMRI) based on the blood oxygenation level-dependent (BOLD) signal is predicated on the coupling between neural activity and cerebral blood flow (CBF), as well as the physical relationship between the oxygenation state of hemoglobin and its magnetic susceptibility. This chapter explores these biophysical relationships and how they give rise to the BOLD effect and how physiological parameters of interest may be inferred from the BOLD signal.

2.1 Neurovascular Coupling

2.1.1 Neural Energetics

In all neurons, an electric potential exists across the cell membrane; it is produced by an unequal distribution of ions, primarily K^+ and Na^+, in the intra- and extra-cellular spaces. When a neuron receives an electrical or chemical signal at its dendrites, ion channels across the cell membrane

open or close in a coordinated fashion allowing ions to flow in or out of the cell depending on the electrochemical gradients. This electrochemical signal will propagate down the dendrites to the neuronal body, or soma. If the soma is depolarized beyond a cell-specific threshold, an electric impulse will propagate along the cell axon via an action potential. Each neuron's action potentials are of the same magnitude; therefore, the *amplitude* of the soma's depolarization is transmitted by the *frequency* of action potential firing [29]. When an action potential reaches an axon synapse, neurotransmitters are released, allowing the signal to propagate to post-synaptic neurons. From a thermodynamic perspective, neuronal signalling is an energetically downhill process [30]; returning the neuronal ionic and neurotransmitter gradients to their basal levels requires energy metabolism. This is fuelled by adenosine triphosphate (ATP) consumption and the ATP is replenished primarily by oxidative metabolism of glucose [31].

The brain does not have large reserves of glucose or oxygen, requiring the two to be constantly delivered to the brain through the blood supply. Glucose is dissolved in plasma and it diffuses down its gradient from blood into tissue when it enters the capillary bed. Oxygen, on the other hand, has very low solubility in plasma; to compensate, the vast majority of oxygen is transported bound to hemoglobin (Hb) in red blood cells [32]. The volume fraction of red blood cells in blood, referred to as the hematocrit, is on the order of 40–45% [33]. This allows for a substantial amount of oxygen to be delivered to tissue once in the capillary bed. The resulting fraction of oxygen that is extracted from blood in the brain (the oxygen extraction fraction – OEF) has been found to be approximately 35–40% and is very uniform across the brain, as determined by both MRI and positron emission tomography [34-37].

With the use of a variety of imaging techniques, it has been well established that cerebral blood flow (CBF), the cerebral metabolic rate of glucose, and the cerebral metabolic rate of oxygen

($CMRO_2$) all increase in activated regions of the healthy brain [12,15,31]. To meet the neuronal demands for glucose and oxygen, smooth muscle surrounding arterioles will relax or contract, driven by various signalling mechanisms, thereby controlling CBF via arteriolar diameter. This relationship between neural activity, energy metabolism, and CBF is known as *neurovascular coupling* and it provides the physiological foundation for most functional neuroimaging.

2.1.2 Cortical Cerebrovascular Physiology

The majority of neuronal signalling and cell metabolism of the central nervous system is localized to grey matter (GM). White matter (WM) consists primarily of the myelinated axon bundles that conduct neural signals between brain regions and their supporting glial cells. Accordingly, cerebral blood volume (CBV) in GM is approximately twice that of WM, with CBV being ~4–5.5% in GM [34,38]. Fresh oxygenated blood is delivered to the brain by arteries. Pial arteries divide across the surface of the brain and eventually dive into the cortex becoming penetrating arterioles. Penetrating arterioles become parenchymal arterioles and branch off at different depths throughout the cortex, as shown in Figure 2.1. All arteries and arterioles are surrounded to some degree by smooth muscle, allowing them to dilate or constrict to control blood flow [39].

Glucose and oxygen extraction and water and waste exchange are generally thought to occur primarily at the level of the capillaries. However, recent experimental evidence from two-photon microscopy with a partial pressure of oxygen (pO_2) tracer has shown that a significant fraction of baseline oxygen extraction occurs at the precapillary arterioles and suggests that the role of capillaries may be to supply oxygen during focal increases in neural activity [40,41]. Capillaries have no smooth muscle but are instead composed of specialized endothelial cells and are surrounded by pericytes and astrocytic end feet, which have debated vasoactive properties and

may play a role in transcellular water and ion exchange, respectively [39]. Capillaries form a dense web of interconnected vessels, increasing their surface area and granting them close proximity to neurons. The density of capillaries also varies with cortical depth, as shown in Figure 2.2, and is highly correlated with neuronal synaptic density [42,43].

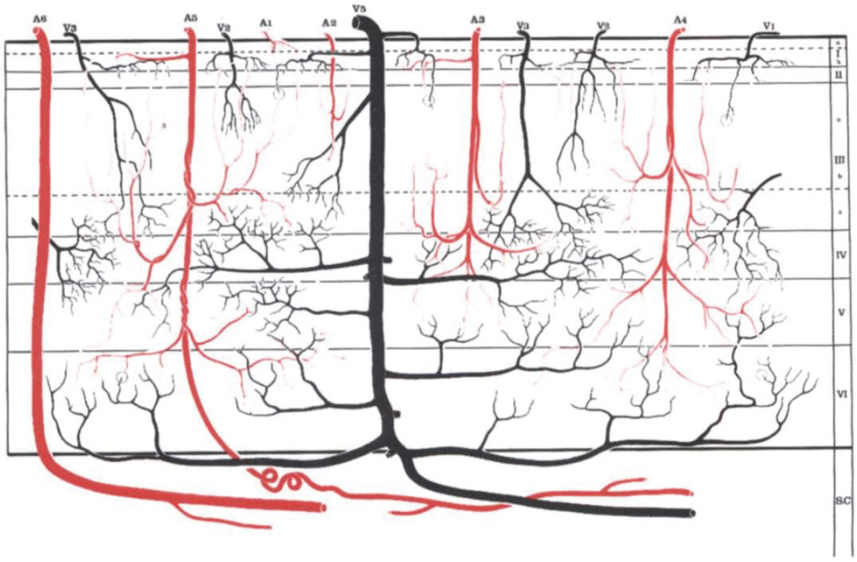

Figure 2.1: Drawing of intracortical penetrating arterioles and draining venules.

Each arteriole (venule) is labeled according to its depth of penetration (drainage) with 1 being the shallowest layers and 6 being the deepest, as proposed by Duvernoy et al. [42]. Arterioles are red and labeled 'A', and venules are black and labeled 'V'. The scale on the right corresponds to the six cortical cellular layers and subcortical (SC) white matter. Adapted from [42].

Veins drain blood and metabolic waste products, such as carbon dioxide, from the brain. In contrast to arteries, veins are thin-walled, valve-less, and only large pial veins possess smooth muscle [39]. As a result, post-capillary veins do not appear to actively participate in the control of blood flow and are thought to passively change their volume in response to increased driving blood pressure [13,44]. Superficial cortical veins in the pia matter drain the cortex and subcortical WM.

Like penetrating arterioles, cortical veins and venules drain blood from different ranges of cortical depths, as shown in Figure 2.1.

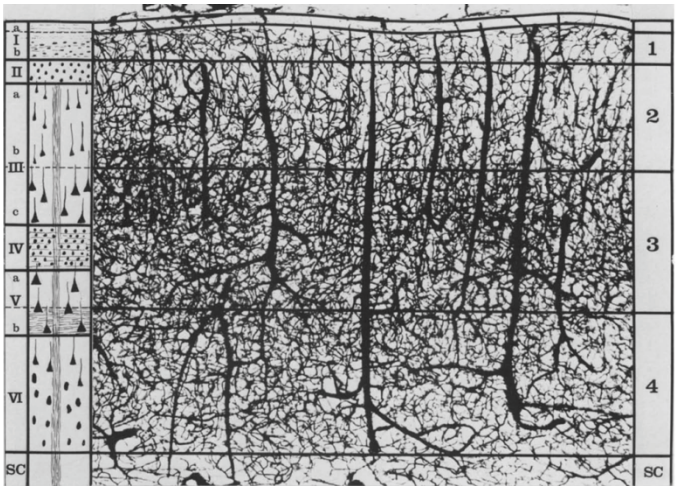

Figure 2.2: Section of cortical vessels.

Stereoscopic microscope images of Indian ink injected and fixed section of cortex. The variable density of capillaries tangentially and across depths is evident. The scale on the left shows the six cortical cellular layers and subcortical (SC) white matter, and the drawings show the cell and fibre types. The scale on the right shows the cortical vascular layers, as proposed by Duvernoy et al. [42]. Adapted from [42].

The distribution of blood volume amongst the three compartments (arterial, capillary, venous) is not equal. Different studies have put the arterial CBV at approximately 10–20% of total CBV, and capillary and venous CBV in the range of 30–50% of CBV (such that the sum of the three adds up to 100%) [19,43,45,46]. The radii of the largest penetrating arteries range from 25–120 μm, and the smaller penetrating and parenchymal arterioles range in size from 5–20 μm [42]. Capillary radii are generally around 1.5–5 μm [19,40,46-48]. Due to fixation and embedding methods used in ex vivo samples, veins often get deformed [42,46]. After accounting for this, estimates of the radii of draining cortical veins are greater than those of arteries, on average, and

are ~10–60 μm [42]. The distributions of vessel sizes have been fit to statistical distributions using different imaging modalities. Germuska et al. [49] have estimated the median vessel sizes using vessel-size index MRI with gadolinium diethylenetriaminepentaacetic acid (Gd-DTPA) contrast agent and have reported that the distribution of sizes can be described by a Frechet distribution with a median radius of 10.1 μm. Similarly, Lauwers et al. [46] have described the distribution of vessel sizes from confocal laser microscopy on Indian ink injected ex vivo human brain. They found that the inverse of the square root of the radius of all vessels followed a normal distribution. The mean radius of capillaries was 3.25 μm and the mean radius of all vessels was 3.9 μm, much smaller than the median radius of 10.1 μm obtained by Germuska et al. [49]. These distributions are explicitly shown in Chapter 6. The discrepancy between the two distributions may be due to i) shrinkage of the ex vivo samples due to their preparation [46], ii) surface vessels being excluded from ex vivo analyses, and iii) a distinct lack of larger vessels due to the ex vivo samples originating in a sulcus [42]. This highlights the challenge in obtaining a "true" distribution of cerebral microvascular sizes.

2.2 BOLD Imaging

2.2.1 Origins of the BOLD Signal

The biophysical basis of BOLD fMRI is dependent on the fact that oxygen in the body is transported bound to hemoglobin within blood. Hb is a large protein with four heme prosthetic groups with an iron ion in the ferrous oxidation state (Fe^{2+}) at each of their centres that can bind oxygen. The binding of oxygen to Hb changes its magnetic susceptibility, χ, from paramagnetic in

the deoxygenated state to diamagnetic in the oxygenated state [50]. The susceptibilities of blood and the surrounding tissue are close to matched when the blood oxygen saturation level (SO_2: the fraction of Hb molecules in the oxygenated state) is near 100% [51]. Where susceptibilities differ, offsets in the local B_0 field arise, which lead to quicker dephasing of the transverse magnetization, i.e., shortened irreversible and apparent transverse magnetization relaxation times (T_2 and T_2^*).

The dependence of the B_0 inhomogeneity on susceptibility differences across blood vessels can be expressed analytically by solving Maxwell's equations if the vessels are approximated as infinitely long cylinders of uniform susceptibility. Based on the orientation of the blood vessel relative to B_0 and the susceptibility difference, $\Delta\chi$, between the vessel and the surrounding medium (tissue), the field offset, ΔB_0, is given by [52]

$$\Delta B_0 = \frac{1}{6}\Delta\chi B_0 \times \begin{cases} 3\left(\frac{R}{r}\right)^2 \sin^2(\theta)\cos(2\phi) & \text{outside the cylinder} \\ 3\cos^2(\theta) - 1 & \text{inside the cylinder} \end{cases}, \qquad (2.1)$$

where the geometry and variables are as defined in Figure 2.3a. This solution describes a characteristic dipole field about the cylinder (Figure 2.3b).

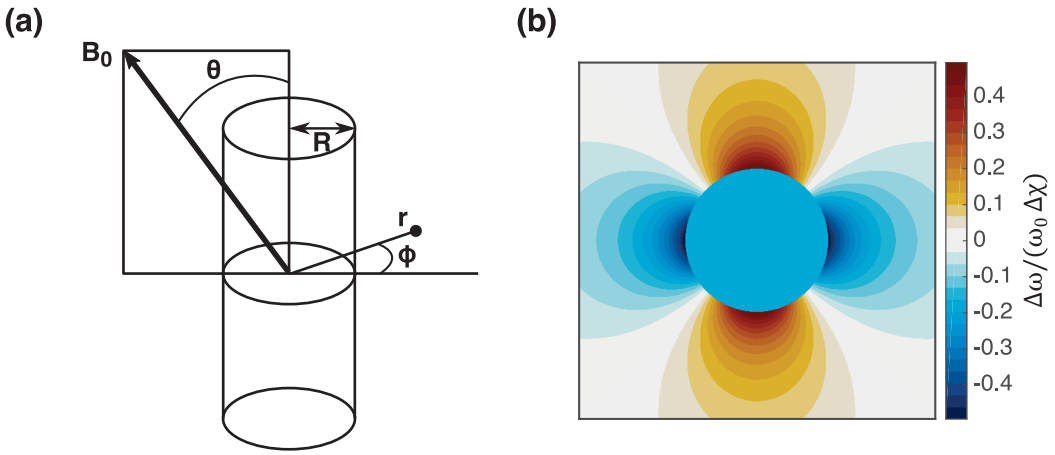

Figure 2.3: Field offsets produced by an infinite cylinder.

(a) Geometry used to describe the orientation of B_0 relative to the cylinder (adapted from [53]). (b) Normalized frequency offset produced when B_0 is perpendicular to the cylinder.

What enables the use of the BOLD signal as a surrogate of neural activity is that increases in neural activity lead to increases in CBF, to allow for more nutrients to be delivered to the activated tissues. Furthermore, there is a significantly larger increase in CBF than in $CMRO_2$ [14], resulting in a *decrease* in the venous concentration of deoxygenated Hb (deoxyHb), an *increase* in T_2^*, and, therefore, an *increase* in the measured BOLD signal [6-8]. In summary, increased neural activity leads to an increased BOLD signal, under normal physiological conditions.

The concentration of deoxyHb in venous blood, or conversely, the concentration of oxygen in venous blood, is related to $CMRO_2$ and CBF through Fick's principle of conservation of mass:

$$CMRO_2 = CBF\, C_aO_2\, OEF \tag{2.2}$$

$$= \mathrm{CBF}\ \mathrm{C_aO_2}\frac{\mathrm{C_aO_2} - \mathrm{C_vO_2}}{\mathrm{C_aO_2}}$$
$$\cong \mathrm{CBF}\ \mathrm{C_aO_2}\frac{\mathrm{S_aO_2} - \mathrm{S_vO_2}}{\mathrm{S_aO_2}}$$
$$\cong \mathrm{CBF}\ \mathrm{C_aO_2}\ (1 - \mathrm{S_vO_2}),$$

where C_xO_2 is the concentration of oxygen in arterial blood (x = a) or venous blood (x = v) and S_xO_2 is the saturation of hemoglobin in arterial or venous blood. The first approximation in Eq. (2.2) comes from the assumption that the majority of oxygen in blood is bound to hemoglobin and that the dissolved oxygen content is negligible [32]. The second approximation comes from the assumption that arterial blood is fully saturated such that $SaO_2 \approx 1$. When these assumptions are violated, such as under hyperoxia, then the first two expressions must be used.

2.2.2 Vessel-Size Sensitivity

Since the early days of BOLD fMRI, it has been appreciated that the sensitivity of the BOLD signal is not uniform across vessel sizes [17,52,54,55]. The sensitivities are often assessed by the changes in either the apparent transverse relaxation rate (R_2^*) for gradient echo (GE) BOLD or the irreversible transverse relaxation rate (R_2) for spin echo (SE) BOLD. The origin of this vessel-size sensitivity is the diffusion of water molecules through the field inhomogeneities resulting from the blood-tissue $\Delta\chi$. Diffusion of water molecules through tissue can be described by a Gaussian probability distribution function along each dimension [56]:

$$P(X,t)dx = \frac{dx}{(4Dt)^{1/2}}\exp\left(-\frac{X^2}{4Dt}\right), \tag{2.3}$$

where $P(X, t)dx$ is the probability of molecules diffusing a distance X along one dimension in a time t, and D is the diffusion coefficient. Due to cell boundaries that restrict mobility, diffusion

can vary greatly across tissues in the brain, and what is measured in vivo is referred to as the apparent diffusion coefficient (ADC). The ADC of cortex is relatively isotropic and is approximately 0.75–1.0 $\mu m^2/ms$ [57-59].

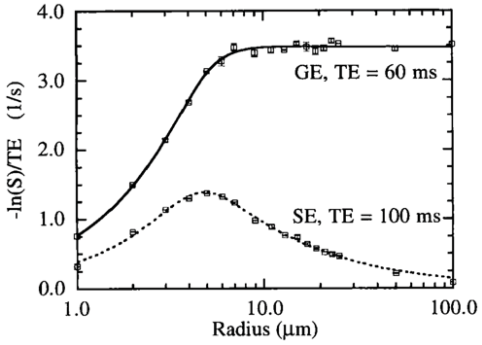

Figure 2.4: GE and SE BOLD vessel-size sensitivities.

Vessel-size dependence of the effective gradient echo (solid line) and spin echo (dashed line) relaxation rates. Reproduced from [17].

Depending on the relative proportions of the characteristic diffusion distance and the dephasing induced by the field inhomogeneities, the system of spins is said to be in one of three dephasing regimes: motional narrowing, intermediate, or static dephasing [60]. Motional narrowing corresponds to the case where diffusion is large relative to the field inhomogeneities, such as surrounding small vessels. Static dephasing corresponds to the opposite, such as surrounding large vessels, where diffusion is small relative to the field inhomogeneities. And the intermediate dephasing regime is observed in between these extremes. Figure 2.4 shows how these regimes manifest themselves in the GE and SE BOLD relaxation rates. These curves can be explained by two competing processes: the ability to dephase, and the ability to refocus. For smaller vessels, nuclei are exposed to a range of field inhomogeneities as they diffuse. This exposure to a wide range of field inhomogeneities results in each spin accumulating a smaller net phase but also a loss of phase memory and irreversible signal loss. As the vessel size increases,

the amount of dephasing increases since more nuclei become consistently exposed to large field offsets. By the same argument, the ability to refocus the dephasing with a 180° pulse also increases with vessel size since the likelihood of nuclei being exposed to the same fields prior to and after the pulse increases. This explains why R_2 and R_2^* are almost equal for the smallest vessels, because refocusing was less effective and because there was less decay to begin with (motional narrowing regime: small R_2^*, small R_2). For large vessels, decay is quite strong and so is the refocusing (static dephasing regime: large R_2^*, small R_2). For intermediate vessels, the amount of decay starts to become more significant but the refocusing is still not effective enough to undo all the dephasing (intermediate dephasing regime: medium R_2^*, medium R_2).

Because of these features, GE BOLD is particularly sensitive to blood oxygenation changes in large draining veins, such as on the pial surface, and SE BOLD is more sensitive to blood oxygenation changes around capillaries. Given the correlation between capillary and synaptic density discussed in section 2.1.2, SE BOLD is considered more spatially specific to changes in neural activity than GE BOLD [17,61,62]. However, GE BOLD is much more commonly employed since it has higher sensitivity because of its larger R_2^*.

The reliance of R_2^* on the concentration of deoxyHb ([dHb]) can be described by [15]

$$\begin{aligned} R_2^* &= R_{2|0}^* + R_{2,\mathrm{dHb}}^* \\ &= R_{2|0}^* + k\ \mathrm{CBV_V}\ [\mathrm{dHb}]^{\beta}, \end{aligned} \tag{2.4}$$

where $R_{2|0}^*$ is the R_2^* from non-deoxyHb sources, k is a field strength and sample-dependent scaling factor, $\mathrm{CBV_V}$ is the venous CBV (or volume of deoxygenated blood), and β, the non-linear dependence of R_2^* on [dHb], is a parameter that reflects diffusion-induced dephasing. From extra-vascular simulations, β is approximately 2 for small vessels, 1 for large vessels, and somewhere in

between 1 and 2 for distributions of vessel sizes [15,17,52]. Recent studies have also aimed to measure β in vivo: maps of β across the brains of rats have been generated with the administration of the contrast agent, feraheme, and the changes in R_2' were related to the change in contrast agent concentration to measure β [63]. However, using a contrast agent that substantially alters the susceptibility of blood and the dephasing regime of extra-vascular water, may not be appropriate for estimating β, as β is itself dependent on the dephasing regime [64]. β has also been measured in humans in grey matter by increasing the participants' inspired oxygen levels while measuring changes in R_2^* [65]. This latter technique may be more appropriate for measuring β because, like the BOLD signal, it is localized to deoxygenated CBV and it only slightly alters the susceptibility of blood by changing S_vO_2.

2.2.3 Calibrated fMRI

The physiological changes underlying the BOLD signal can be ascertained through biophysical signal modelling. With the use of Fick's principle and by combining results from simulations and experiment, Davis et al. [15] created a simple model of how hemodynamic and metabolic changes influence the BOLD signal, known as the *calibrated fMRI model*. This model is represented by the equation below

$$\frac{\Delta\text{BOLD}}{\text{BOLD}_0} = M\left(1 - \left(\frac{\text{CBF}}{\text{CBF}_0}\right)^{\alpha-\beta}\left(\frac{\text{CMRO}_2}{\text{CMRO}_{2|0}}\right)^{-\beta}\right), \qquad (2.5)$$

where the subscript '0' refers to a value at baseline. α accounts for coupling between changes in CBV_V and CBF, arising from an empirical power law relation between the two, and is known as the Grubb constant [13,66,67]. This value is approximately 0.2 – as measured by changes in CBF and deoxygenated CBV induced by hyper- and hypocapnia [67] and visual and sensorimotor

stimulation [13]. β is as described in the previous section. M, known as the BOLD *calibration constant*, is proportional to the resting concentration of deoxyHb in blood and it represents the maximum fractional increase in the BOLD signal, which would theoretically occur upon removal of all deoxyHb in blood (i.e. venous $SO_2 \rightarrow 100\%$) [15]. M is related to the resting physiology and relaxation rate in Eq. (2.4) by the following [14]

$$\begin{aligned} M &= R^*_{2,\mathrm{dHb}|0}\,\mathrm{TE} \\ &= k\,\mathrm{CBV}_{\mathrm{V},0}\,[\mathrm{dHb}]_0^{\beta}\,\mathrm{TE}. \end{aligned} \tag{2.6}$$

If M is known, Eq. (2.5) can be inverted to measure fractional changes in $CMRO_2$ from task-induced BOLD and CBF signals. The goal, therefore, of an fMRI calibration experiment is to measure M across the brain. Several techniques exist for measuring M, including increasing inspired CO_2 (inducing hypercapnia) while acquiring BOLD and CBF images [15] or increasing inspired O_2 (inducing hyperoxia) while acquiring BOLD images and measurements of arterial pO_2 [21]. By removing the need for estimating CBF changes with lower signal-to-noise ratio arterial spin labelling images, hyperoxic M estimates have greater precision than hypercapnic estimates [22], however, they require the assumption of baseline hematocrit and OEF, which can lead to increased bias [26]. By combining the two gas challenges, it is possible to estimate baseline OEF and $CMRO_2$ and, hence, reduce some of the bias of hyperoxic calibration [36,68]. Recent controversy surrounding the magnetic susceptibility of dissolved oxygen in blood did bring into question the use of hyperoxia in BOLD studies, however, this issue is resolved via the work presented in Chapter 4.

Shortly after the introduction of calibrated fMRI [14,15], Kida et al. [24] proposed a gas-free calibration technique based on the measurement of the transverse relaxation rates, R_2 and R_2'. R_2 and R_2^* were measured using multi-echo spin echo and gradient echo echo planar imaging sequences, from which R_2' was determined via the relation $R_2^* = R_2 + R_2'$. These relaxation rates and CBF were sequentially measured in rats under anesthesia and under additional neural activity modulating agents to infer the metabolic and hemodynamic-induced changes in R_2 and R_2' and to compare them to an MR spectroscopic measure of $\Delta CMRO_2$. This required long total acquisition times that were feasible with the paradigm of pharmacological agents employed in animals but would not easily translate to tasks of shorter duration often employed in humans. A key finding, however, was that R_2' was ~3 times more sensitive to changes in venous oxygenation than R_2, suggesting that R_2' alone may be sufficient to assess vessel oxygenation. Fujita et al. [25] later used this finding to perform gas-free calibration in healthy human subjects by quantifying R_2' *at rest only* using the GESFIDE (gradient echo sampling of FID and echo) sequence [69], and substituting $R^*_{2,\mathrm{dHb}|0}$ in Eq. (2.6) with $R'_{2|0}$. Other methods for gas-free calibration have since been proposed and this is the topic of Chapter 6.

2.2.4 Intravascular BOLD Signal

In developing the calibrated fMRI model in Eq. (2.5), intravascular (IV) contributions to the BOLD signal were ignored [14,15]. However, due to the strong field offsets generated by deoxyHb, intravascular nuclei, while small in number relative to extravascular (EV) nuclei, can make up approximately 50% of the BOLD signal at 1.5 T, 30% at 3 T and 10% at 7 T for conventional acquisition parameters [9]. Given this non-negligible contribution, it is important to consider IV

contributions when modelling the BOLD signal. From a simulation perspective, a straightforward way to incorporate IV signal is by populating the vessels to the desired hematocrit by modelling red blood cells as spherical perturbers (for which the field offsets can be described analytically) or another, more realistic, geometry [10,70]. However, this method is extremely computationally demanding given the enormous number of red blood cells that populate each vessel. A simpler alternative is to analytically calculate the IV signal and to incorporate it into a purely EV signal model, although this has typically only been done assuming monoexponential decay while ignoring the dephasing and refocusing of IV signal during a spin echo [19,71-73].

The relaxation rate of blood itself has predominantly been described by theories of chemical exchange or molecular diffusion [74]. In exchange theory [75], water molecules are in fast exchange between red blood cells and plasma, with a susceptibility-induced Larmor frequency shift between the two sites, such that the transverse magnetization dephases over time. In molecular diffusion theory, the diffusion of water molecules through the distribution of field offsets produced by red blood cells results in the net dephasing of transverse magnetization over time [76]. Given that red blood cells are compact (generally described by a biconcave disc with a diameter of ~8 μm and thickness of 2.5 μm [77]) and diffusion in plasma is relatively high, blood is typically considered to be in the motional narrowing regime [60]. In this case, the molecular diffusion theory can be described by the so-called *weak field approximation* of Jensen and Chandra [76].

The relaxation rate of blood ($R_{2,\mathrm{blood}}$) from both exchange and diffusion theories can be described by the general expression [78]

$$R_{2,blood} = R_{2,0} + \Delta R_2, \tag{2.7}$$

where $R_{2,0}$ reflects the intrinsic relaxation rates in red blood cells and plasma and will have a dependence on the hematocrit and the oxygenation of red blood cells, and ΔR_2 is the added relaxation rate from either exchange or diffusion. ΔR_2 depends on the pulse sequence (GE or SE) and the spacing between 180° pulses if a multi-echo SE sequence is used to measure R_2. The dependence of ΔR_2 on B_0 and the physiological parameters from both theories is $\Delta R_2 \propto$ Hct (1 – Hct) ((1 – SO_2) $B_0)^2$, where Hct is the hematocrit [45,76,79]. The weak field approximation explicitly models the dependence on the inhomogeneity length scale (i.e. the red blood cell size), whereas, in exchange theory, this size dependence is subsumed in the exchange lifetime of water.

The molecular diffusion theory would appear to be a more intuitive description of the process leading to dephasing since there is a range of field offsets that nuclei are exposed to in and around red blood cells. In fact, studies at multiple field strengths from 1.5 to 7 T have found that the weak field approximation produces better fits to measured relaxation rates in blood samples than the exchange model [78,80,81]. However, not all studies find this trend [82], and in reality, the differences between the two models' predictions may be small enough to not be of practical concern [78].

Chapter 3

Deterministic Diffusion Simulations

A substantial amount of the work in this thesis consisted of simulating the evolution of transverse magnetization in the presence of magnetic field perturbations, such as those produced by red blood cells or blood vessels. The method of simulation employed is referred to as the *deterministic diffusion* method [83]. A brief background on this method is provided, followed by a more detailed description of how it was implemented in this thesis.

3.1 Background

The deterministic diffusion method was originally developed by Bandettini and Wong [83] to efficiently simulate the extravascular MR signal where blood vessels were modelled as infinite cylinders. This method differs from Monte Carlo (MC) simulations – where the phases are calculated for individual hydrogen nuclei following a random walk throughout the field inhomogeneities – in two notable ways:

1. Diffusion of nuclei is modelled as a blurring of the transverse magnetization across space.
2. The transverse magnetization and the field inhomogeneities are calculated across a discretized grid in either two-dimensional (2D) or three-dimensional (3D) space.

The first point was justified by the fact that, as discussed in Section 2.2.2, the unhindered diffusion of water molecules across space will follow an isotropic Gaussian probability distribution over time. In this case, the diffusion of transverse magnetization can be modelled as the convolution of the magnetization with a Gaussian smoothing kernel. Discretizing the magnetization across space enables the practical implementation of the convolution.

In addition to these differences, Bandettini and Wong's original implementation of the deterministic diffusion method calculated the signal from an ensemble of randomly oriented vessels in a radically different manner – in keeping with the aim of improving the computational efficiency of the simulations. Unlike earlier MC simulations, where blood vessels (or cylinders) were typically randomly distributed and randomly oriented in 3D [10,17,52,55,84], the deterministic diffusion method only considered the transverse magnetization in a 2D plane with a single infinite cylinder placed at its centre and normal to the plane, as shown in Figure 2.3. The ratio of the cylinder's radius and the simulation plane's width were chosen to give the desired CBV. The simulations were repeated with the B_0 angle stepped through a range of azimuthal and polar angles and the final MR signal from an ensemble of randomly oriented vessels was obtained by averaging the simulations from each B_0 angle. Later, Schwarzbauer and Deichmann [23] showed that the simulations were rotationally invariant under changes in ϕ, thereby further reducing the simulation time by eliminating the need to step through azimuthal angles.

The above approach substantially reduced the time required to simulate the signal from an ensemble of vessels as compared to 3D Monte Carlo (MC) simulations, however, it is limited to modelling infinite cylinders and does not give an estimate of the variability of the simulations like one gets from MC simulations, where the simulations are repeated with multiple random walks of spins. These limitations can be removed by performing the simulations in 3D with multiple vessels all randomly oriented in space, just as in 3D MC simulations [71]. Each vessel can take on a different radius and any orientation in space, and to get a measure of the variability in the simulations, the simulations can be repeated with multiple simulation networks, each with the same CBV but with a different distribution of the vessels in space. Other than the method used to calculate the transverse magnetization, these simulations are identical to MC simulations and can be used to calculate the signal from any distribution of perturbers, be they cylinders or spheres, for which there exist analytical expressions for the field inhomogeneities generated by them, or more arbitrary geometries, for which the field offsets can be calculated by Fourier-based forward field modelling [85-87].

Finally, while running the simulations in 3D presented a trade-off between the simulations' computational efficiency and their ability to generate variability in their results, Pannetier et al. [73] managed to satisfy both requirements by returning the simulations to 2D. They randomly distributed multiple cylinders, all perpendicular to the 2D plane, up to the desired CBV. Rather than average the simulations over a series of B_0 directions, they calculated the signal just once but where the field offsets surrounding the vessels were calculated from the weighted average of the field offsets generated at two orthogonal B_0 directions (one parallel and one perpendicular to the vessels). This was done to mimic the B_0 distribution of a 3D vessel network. By rerunning the

simulations using multiple spatial distributions of the vessels in 2D, they obtained the same sort of variability one might get in 3D.

3.2 Implementation

In this thesis, simulations were performed in both 2D and 3D, depending on the application: vessel networks were simulated in 2D and sphere networks were simulated in 3D. For simplicity, the theory of the deterministic diffusion method will be presented in 2D but, given that the convolution process is independent along each dimension, extension of the method to 3D is trivial. All simulations were run in MATLAB (MathWorks, Inc., Natick, MA) with some of the functions coded in C using the MEX library. Here, the general implementation of the simulations is described, and the details of the applications are described in the chapters that follow.

3.2.1 Defining the Perturbers

The simulations here were all run over areas or volumes with isotropic side length, W. The simulations were discretized onto a lattice with N elements per dimension, resulting in a spatial resolution $\Delta x = W/N$. In the case of the 2D vessel networks, the networks were defined in the following way:

1. Vessels were modelled as infinite cylinders perpendicular to the simulation plane.
2. The centre coordinate of each vessel was randomly selected from a continuous uniform distribution across the plane with each coordinate ranging from $-W/2$ to $+W/2$.
3. Vessel radii were either constant or randomly selected from a distribution of radii.

4. Vessels were added to the plane until the desired volume fraction, ζ, was reached.

This process results in a 2D matrix, **P**, describing the locations of the perturbers, such that $P_{kl} = 1$ when the (k,l)-th lattice element is occupied by a perturber and $P_{kl} = 0$ otherwise.

In addition to the perturber matrix, there is a corresponding field inhomogeneity matrix, $\mathbf{\Delta\omega}$, that describes the net field offset at each lattice element. Here, $\mathbf{\Delta\omega}$ was calculated as the superposition of the field offsets generated by each perturber. Analytical expressions for the field offsets generated by a single vessel or sphere are given in Eqs. (2.1) and (5.13), respectively. Rather than calculate the field inhomogeneities produced by the vessels as the average from two orthogonal B_0 directions, as in Pannetier et al. [73], we chose to assign each vessel its own randomly oriented B_0 direction. An example vessel network is shown in Figure 3.1. This method, originally proposed by Miller and Jezzard [88], is more likely to reproduce the distribution of field offsets in a 3D network as compared to the orthogonal averaging method. To sample from a uniform distribution of angles across the unit sphere, the B_0 azimuth, ϕ, was randomly selected from a uniform distribution ranging from 0 to 2π and the polar angle, θ, was assigned from a $\sin(\theta)/2$ distribution. This was implemented by setting $\theta = \cos^{-1}(2u\text{-}1)$, where u was randomly selected from the uniform distribution ranging from 0 to 1 [89].

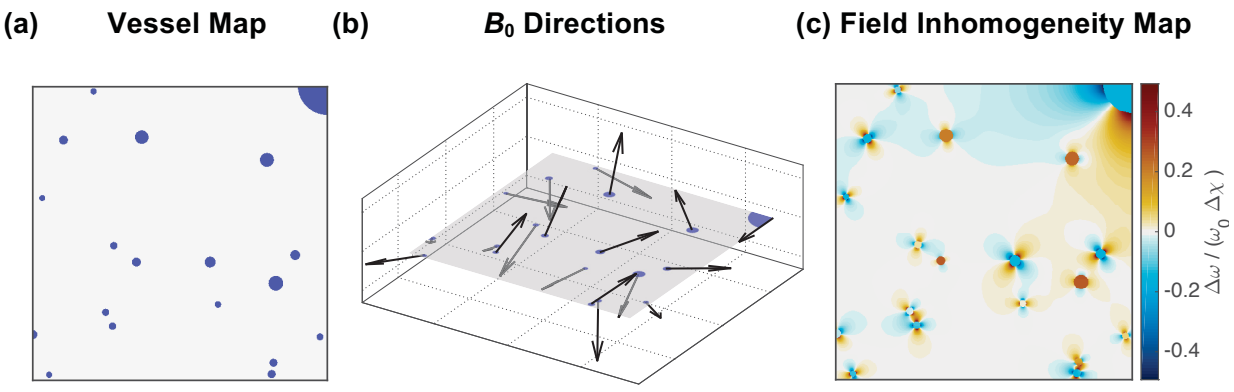

Figure 3.1: 2D vessel map and its field inhomogeneity map.

(a) Example 2D vessel map (i.e., the **P** matrix). The blue circles correspond to the vessel cross sections. The vessel radii are random. (b) The random B_0 directions assigned to each vessel. The directions are represented by the arrows and are overlaid on a semi-transparent version of the vessel map. (c) The field inhomogeneity map (i.e., the **Δω** matrix) generated by the vessels. All the vessels were assigned the same susceptibility offset, $\Delta\chi$, and the map was normalized by $\omega_0\Delta\chi$.

In the case of the 3D sphere distributions, spheres of equal radii were distributed throughout the simulation volume until the desired ζ was reached and **Δω** was computed from the superposition of the dipole fields generated by each sphere.

3.2.2 Tracking Transverse Magnetization

The calculation of the transverse magnetization across space was performed by simultaneously accounting for precession, transverse relaxation, and diffusion. As is common – although not necessary – with many MC or deterministic diffusion simulations of the BOLD effect, longitudinal relaxation and the effects of imaging gradients were ignored [10,17,52,54,70,90,91]. In both the 2D and 3D models, the complex magnetization, **M**, was calculated in discrete time steps, δt, and was operated on by a relaxation and precession matrix, **R**, and a diffusion kernel, **D**. The magnetization at the j-th time point was given by

$$\mathbf{M}_j = \begin{cases} \left(\mathbf{M}_{j-1} \cdot \mathbf{R}\right) * \mathbf{D} & \text{if } j > 0 \\ \mathbf{1} & \text{if } j = 0 \end{cases} \tag{3.1}$$

where · denotes element-wise multiplication and $*$ denotes convolution. Following an initial 90° excitation pulse, Eq. (3.1) implies that each element of the lattice had a uniform magnetization with an initial phase of 0 and a magnitude of 1.

The relaxation and precession matrix was given by

$$R_{kl} = \exp(-i\Delta\omega_{kl}\delta t) \cdot \begin{cases} \exp\left(\delta t / T_{2,ip}\right) & \text{if } P_{kl} = 1 \\ \exp\left(\delta t / T_{2,ep}\right) & \text{if } P_{kl} = 0 \end{cases}, \tag{3.2}$$

where $T_{2,ip}$ ($T_{2,ep}$) is the irreversible intra-perturber (extra-perturber) transverse relaxation time, e.g. in the case of a vessel network, $T_{2,ip}$ was the T_2 of blood and $T_{2,ep}$ was the T_2 of grey matter. In the cases where just the effects of susceptibility induced dephasing were considered, $T_{2,ip}$ and $T_{2,ep}$ were ignored.

Diffusion was modelled by an isotropic, Gaussian blurring of the magnetization along each dimension, independently. This was implemented by linear convolution (i.e., non-circular convolution) of the magnetization with the one-dimensional discrete diffusion kernel with a width parameter equal to the expected mean-square displacement of the spins, $\sigma^2 = 2D\delta t$, where D is the diffusion coefficient of water in the tissue of interest. The discrete diffusion kernel is the solution to the discrete-space, continuous-time diffusion equation [92]. The k-th element of the kernel was given by [92]

$$D_k = e^{-(\sigma/\Delta x)^2} I_{k-N_{hw}}((\sigma/\Delta x)^2), \tag{3.3}$$

where N_{hw} is the number of elements in the kernel half-width, such that the total number of elements in the kernel is $2N_{hw} + 1$, and $I_{k-N_{hw}}$ are the modified Bessel functions of the first kind

of integer order k-N_{hw}. The half-width of the kernel was a minimum of 6σ (rounded up to the nearest integer) and was extended, if necessary, until $1 - \sum D_k \leq 5\times10^{-8}$. This requirement assured that the kernel was approximately normalized and, therefore, that magnetization was conserved. As an example, in the simulations employed in Chapter 6, the same simulation networks were rescaled for vessel networks with radii ranging from 1–16 μm. For $D = 0.8$ μm^2/ms, $\delta t = 0.25$ ms, and a matrix size of 1020^2, the normalization error, $1 - \sum D_k$, across the full-width at 6σ was 8×10^{-9} for the 1-μm networks and 1.5×10^{-4} for the 16-μm networks. As a result, the kernel was extended from a half-width of 1 to 3 for the 16-μm networks, reducing the normalization error to 2×10^{-9}.

Refocusing pulses were modelled by taking the complex conjugate of the magnetization at each lattice element. Finally, the signal magnitude at the j-th time point was given by

$$S_j = \frac{1}{N'^2}\left|\sum_{k,l} M_{kl,j}\right|, \tag{3.4}$$

where N' was the number of elements summed along each dimension. N' is different from the total number of lattice elements along each dimension, N, and is explained below.

3.2.3 Lattice Resolution and Extent

In every application of the simulations, the required spatial resolution, Δx, and the spatial extent of the lattice, W, need to be considered. The required spatial resolution is generally constrained by sampling the field offsets generated by the smallest perturbers. Here, this was determined in advance of each study by simulating at a much higher spatial resolution than necessary and then finding a lower resolution where the root mean square error (RMSE) between the reference signal

and the test signals was still below any noticeable threshold. Generally, this RMSE threshold was $\sim 10^{-3}$, where the simulations were normalized to 1.

The spatial extent of the lattice should be large enough such that:

1. It contains enough perturbers for the simulations to converge relatively quickly.
2. Convolution edge effects do not contaminate the sampled lattice area.
3. Long-ranging field effects from the largest perturbers can be experienced by the spins.

The lattice must also be small enough to meet the specific memory constraints of the CPU being used for the simulations. The three conditions enumerated above help define three regions for running the simulations: the sampled lattice area, the unsampled lattice edge, and the padded edge.

As shown in Figure 3.2, the lattice occupies both the sampled lattice area and the unsampled lattice edge, and it has extent W and N elements per side. It is over the lattice (both sampled and unsampled regions) where the magnetization and diffusion are calculated using Eq. (3.1). The sampled lattice area is the region over which the magnetization is summed in Eq. (3.4) to calculate the net MR signal. It has extent W' and N' elements per side, with $W' \leq W$ and $N' \leq N$. The sampled lattice area is related to the convergence of the simulations by the law of strong numbers, which tells us that the simulations will converge on the true mean as the number of perturbers is increased and the variance of the sample mean will be proportional to 1/(# perturbers) [93]. From this, the variance on the simulation estimates can be reduced by increasing the number of perturbers in each simulation network and/or by increasing the number of networks (N_{net}) to run

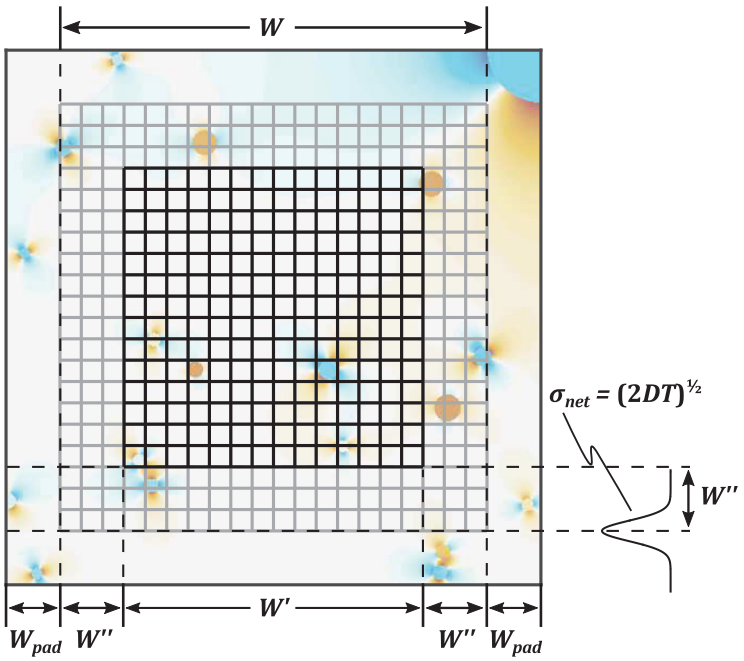

Figure 3.2: Layout of the simulation plane.

The entire simulation plane is enclosed in the solid black box, within it are: the sampled lattice area, designated by the black grid of width W'; the unsampled lattice area, designated by the grey grid with edge width W''; and the padded edge, designated by the external edge with no grid and of edge width W_{pad}. The total lattice width is $W = W' + 2W''$ and the total simulation plane width is $W + 2W_{pad}$. Shown on the right is the net diffusion kernel for a total simulation time T; its half-width is ~$6\sigma_{net}$ and W'' should be greater than or equal to it. The usefulness of the padded edge is exemplified by the large vessel in the top right corner of the simulation plane, whose field offsets extend a considerable distance from its centre and into the sampled lattice area. Note that the grid size in the figure is much coarser than generally used in the simulations and is only drawn this way for illustrative purposes.

the simulations over. If the number of perturbers is to be increased but the volume fraction kept constant, then W'' must be increased. This can be summarized by the relation

$$\sigma^2 \propto \frac{1}{\#\ perturbers} \propto (N_{net}\ \zeta\ W')^{-1}. \qquad (3.5)$$

As a result of using linear convolution to compute the diffusion process, elements near the edge of the lattice will be given by a weighted sum of elements inside the lattice and elements outside the lattice with no magnetization. The unsampled lattice edge accounts for these convolution edge effects where the diffusion kernel interacts with areas outside of the lattice, which have no magnetization, and therefore corrupt the "true" magnetization inside the lattice. The minimum required unsampled edge length, W', can be determined by considering the net kernel width, σ_{net}, at the end of the simulation time, T. We want the probability of magnetization at the very edge of the lattice to be able to diffuse into the sampled area to be approximately 0. Since we determined that a half-width of 6σ was sufficient to capture nearly all magnetization, W'' can be determined by

$$W'' \geq 6\sigma_{net} = 6\sqrt{2DT}. \tag{3.6}$$

An unfortunate consequence of having to predefine the unsampled edge width when creating the simulation networks is that, if one later wanted to simulate for a time > T, then the networks would need to be recreated with a larger W'. Fortunately, most BOLD imaging sequences do not consider the transverse magnetization much beyond ~100 ms, therefore, one can pick a conservative estimate for T such that the networks can be reused in most cases.

The final simulation region is the padded edge. It extends beyond the lattice by an amount W_{pad} and allows for perturbers to populate the region outside of the lattice, where the magnetization is not tracked. This is useful in cases where the field offsets generated by perturbers are experienced in the lattice but the range of spin diffusion in the simulation time is too short to require calculating the magnetization in this area since the likelihood of spins from the padded edge diffusing into the sampled area, and vice versa, is very low. The minimum width required for

this area can be determined by selecting a threshold for which the ΔB_0 from the strongest perturber should be sensed within the lattice. For example, if one chooses to sample down to some fraction, b, of the maximum ΔB_0 produced by a vessel of radius R, then making the combination of the unsampled edge length and the padded edge a minimum size of $b^{½}R$ would ensure this – since the field offsets generated by a vessel fall off with distance r as $(R/r)^2$.

As a final comment, the use of the unsampled edge and the padded edge can be removed by performing the convolutions with the diffusion kernel using circular convolution and by calculating the field offsets using Fourier-based forward field modelling, respectively [73,94,95]. Circular convolution has the effect that spins diffusing out of the simulation lattice will wrap around to the other side of it and, therefore, never experience regions of undefined magnetization or field inhomogeneity. This circular convolution can be calculated using the product of the Fourier transforms of **D** and **M**. Similarly, Fourier-based forward field modelling, when performed using circular convolution, will also result in long-ranging field offsets wrapping around the lattice to the opposite edge. Although we are unaware of any side-by-side comparison of the two different implementations, our own experience was that the required time to calculate the convolution in the Fourier domain was longer. This was because, when calculated in the Fourier domain, the diffusion kernel needed to be a complex matrix of the same size as the simulation matrix and the forward and inverse Fourier transforms of **M** had to be calculated prior to and after multiplication with the diffusion kernel, respectively. When calculated in the spatial domain, the diffusion kernel could be significantly smaller than the lattice size and it could operate along each dimension independently. As a result, the convolution calculation in the spatial domain required fewer mathematical operations and was faster. This was our primary reason for calculating the simulations in the spatial domain.

In Chapters 5 and 6, these methods are applied to spherical and cylindrical perturbers, modelling red blood cells and blood vessels, respectively.

Chapter 4

The Susceptibility of Blood During Hyperoxia

4.1 Preface

THE use of hyperoxia in BOLD studies has gained in popularity because of its ability to passively increase venous oxygenation and, therefore, increase the BOLD signal and provide physiologically relevant contrast [21]. Furthermore, due to the lack of significant perfusion changes arising from hyperoxia, it provides an attractive means of calibrating the BOLD signal without needing to use inherently low signal-to-noise ratio arterial spin labelling sequences to measure perfusion changes during the gas challenge.

In addition to oxygen's impact on the BOLD signal through its influence on T_2^*, it is known to directly reduce T_1 [96,97], making it possible to monitor changes in the partial pressure of

oxygen (pO_2) in tissues during hyperoxia [98-101]. This T_1 shortening is the result of oxygen being a paramagnetic molecule [102], just like deoxyhemoglobin. While the concentration of dissolved oxygen in blood is generally low enough to be ignored under normal physiological conditions [32,74], at elevated pO_2 levels, the susceptibility of arterial blood may become substantially more paramagnetic, resulting in a confounding contribution to the BOLD signal. This is, in fact, precisely what was recently predicted by Schwarzbauer and Deichmann [23] using a theoretical model for the susceptibility of blood with dissolved oxygen.

After evaluating the susceptibility calculations in [23], we determined that they were flawed in multiple ways, including overestimating the volume fraction occupied by dissolved oxygen and an inability to accommodate blood with non-standard hematocrit values. This chapter (based on [103]) presents a reformulation of the susceptibility of blood that accounts for these errors and that is validated through susceptibility measurements in oxygenated ex vivo bovine plasma and distilled water. This paper included two appendices that are included at the end of the chapter, for continuity.

The Effect of Dissolved Oxygen on the Susceptibility of Blood

Avery J.L. Berman[1,2], Yuhan Ma[1], Richard D. Hoge[3,4], G. Bruce Pike[2]

[1]McConnell Brain Imaging Centre, Montreal Neurological Institute, McGill University, Montreal, Canada

[2]Department of Radiology and Hotchkiss Brain Institute, University of Calgary, Calgary, Canada, T2N 4N1

[3]Institut de génie biomédical, Département de physiologie, Université de Montréal, Montréal, Canada

[4]Unité de neuroimagerie fonctionelle, Centre de recherche de l'institut de gériatrie de Montréal, Montreal, Canada

Magnetic Resonance in Medicine, 2016; 75(1): 363–71

4.2 Abstract

Purpose

It has been predicted that, during hyperoxia, excess O_2 dissolved in arterial blood will significantly alter the blood's magnetic susceptibility. This would confound the interpretation of the hyperoxia-induced blood oxygenation level-dependent (BOLD) signal as arising solely from changes in deoxyhemoglobin. This study, therefore, aimed to determine how dissolved O_2 affects the susceptibility of blood.

Theory and Methods

We present a comprehensive model for the effect of dissolved O_2 on the susceptibility of blood and compare it with another recently published model, referred to here as the ideal gas model (IGM). For validation, distilled water and samples of bovine plasma were oxygenated over a range of hyperoxic O_2 concentrations and their susceptibilities were determined using multi-echo gradient echo phase imaging.

Results

In distilled water and plasma, the measured changes in susceptibility were very linear, with identical slopes of 0.062 ppb/mm Hg of O_2. This change was dramatically less than previously predicted using the IGM and was close to that predicted by our model. The primary source of error in the IGM is the overestimation of the volume fraction occupied by dissolved O_2.

Conclusion

Under most physiological conditions, the susceptibility of dissolved O_2 can be disregarded in MRI studies employing hyperoxia.

Keywords

susceptibility; dissolved O2; blood BOLD; hyperoxia

4.3 Introduction

The magnetic susceptibility of materials and tissues is of fundamental importance in NMR and MRI: it relates the magnetization induced in matter to an applied external field, and differences in susceptibility across boundaries can produce non-local field offsets that alter the MR signal. The susceptibility of hemoglobin (Hb) is of particular significance since the molecule undergoes conformational changes and electronic rearrangement when binding O_2 that result in a conversion of Hb from being paramagnetic in the deoxygenated state to diamagnetic when oxygenated [50]. This property of Hb has been exploited in several MRI techniques, most notably blood oxygenation level-dependent (BOLD) functional MRI (fMRI) for the localization of changing neural activity [6-8] and susceptibility weighted imaging for the identification of veins [104]. These techniques are made possible by the fact that, under normal physiological conditions, Hb in veins and capillaries is partially saturated with O_2, making these vessels paramagnetic relative to the surrounding tissue, resulting in frequency offsets between the vessels and tissue and increased transverse decay [11]. On the other hand, Hb in arteries under normal physiological conditions is generally nearly fully oxygen saturated, imparting little susceptibility difference relative to the surrounding tissue and, therefore, negligible contributions to BOLD fMRI and susceptibility weighted imaging (neglecting inflow enhancement effects).

Some fMRI techniques now use hyperoxia as a means of altering the BOLD signal: under hyperoxia, the partial pressure of O_2 (pO_2) in blood is high enough such that nearly all arterial Hb is oxygenated and an excess of O_2 molecules are dissolved in arterial blood [32]. The excess O_2 in arterial blood that is not consumed by tissue metabolism ends up bound to Hb in veins, reducing the venous concentration of deoxy-Hb (dHb) and resulting in a subsequent increase in the BOLD

signal relative to normoxia (breathing of room air). By modulating the BOLD signal, hyperoxia has been used in calibrated BOLD [21,22] and has also been proposed as a method for measuring deoxygenated cerebral blood volume [105].

Being a paramagnetic molecule, O_2 can have significant effects on MR images; it creates large susceptibility differences between air cavities and tissue, and in turn, can lead to extensive areas of signal dropout in T_2^*-weighted images and geometric distortion in echo-planar imaging. It has also been shown to produce aberrant T_2^* fluctuations during hyperoxia in brain regions fairly distal to the airways [106] and in peripheral vascular reactivity BOLD studies employing air-pressurized cuffs, even in slices up to 15 cm away from the cuff [107]. Despite these effects of *gaseous* O_2, the susceptibility of *dissolved* O_2 in blood is commonly ignored during normoxia since the amount dissolved in plasma is normally very small and its contribution to the net susceptibility of blood is negligible compared to that of the other major constituents, specifically oxygenated and deoxygenated red blood cells (RBCs) and plasma [74,108,109].

Recently, Schwarzbauer and Deichmann (SD) extended the model of the susceptibility of blood to include dissolved O_2 [23]. SD theoretically predicted that when concentrations of dissolved O_2 in blood were sufficiently high, such as during hyperoxia, dissolved O_2 would significantly contribute to the susceptibility difference between arterial blood and the surrounding tissue. Using their extended model and simulations, they predicted that in going from normoxia to hyperoxia, MR signal changes from tissues populated by arteries could be substantial and even comparable to venous-driven BOLD contrast. Considering that BOLD studies are geared towards measuring changes in dHb and not dissolved O_2 directly, the implications of SD's findings for fMRI studies using hyperoxia, such as calibrated BOLD, are profound and have led us to re-examine the model of the susceptibility of dissolved O_2 proposed by SD.

In this article, we show that the model used by SD for incorporating the effect of dissolved O_2 into the susceptibility of blood was inaccurate, specifically, the volume fraction of dissolved O_2 was significantly overestimated. We present an alternative model that corrects for this overestimation and we have validated it by measuring the effect of increasing levels of dissolved O_2 on the susceptibility of distilled water and *ex vivo* bovine plasma.

4.4 Theory

Unless stated otherwise, all susceptibilities are volume susceptibilities in the International System of Units (SI); however, several original sources used cgs units and the susceptibility is often expressed as molar or mass susceptibility. Table 4.1 and Section 4.10 describe all of the susceptibility values used throughout this article, including their original sources and their conversion to volume susceptibility in SI units.

For a mixture of substances in solution, such as in blood, the net susceptibility of the solution, χ_{net}, is given by the weighted sum of the individual susceptibilities, χ_i,

$$\chi_{\text{net}} = \sum_i \alpha_i \chi_i, \tag{4.1}$$

where the weighting factors, α_i, are the volume fractions occupied by the substances in solution. Applying this to blood, χ_{blood} can be divided into contributions from RBCs and plasma [108],

$$\chi_{\text{blood}} = \text{Hct} \cdot \chi_{\text{RBC}} + (1 - \text{Hct}) \cdot \chi_{\text{plasma}}, \tag{4.2}$$

where Hct is the hematocrit, χ_{RBC} includes contributions from intracellular water, paramagnetic dHb, and diamagnetic oxy-Hb, and χ_{plasma} includes contributions from water and plasma proteins.

Table 4.1: Susceptibility values including their sources and their conversion to volume susceptibility in SI units.

Substance	Symbol	Source (ppm, cgs units)	Conversion factor	$\chi(22\,^{\circ}\mathrm{C})$ (ppm, SI units)	$\chi(37\,^{\circ}\mathrm{C})$ (ppm, SI units)
water	$\chi_{\mathrm{H_2O}}$	−12.96 $\mathrm{cm^3/mol}$ [102]	Eq. (4.10)	−9.022	−9.001
oxygen	$\chi_{\mathrm{O_2}}$	3415 $\mathrm{cm^3/mol}$ [102]	$\times 4\pi \cdot 293.15\ \mathrm{K} / (T + 273.15) / \bar{v}_{M,\mathrm{O_2:H_2O}}(T)$ [b]	1383	1342
hemoglobin (diamagnetic component)	χ_{diamHb} [a]	−0.587 $\mathrm{cm^3/g}$ [108]	$\times 4\pi \cdot 5.5\times10^{-6}$ $\mathrm{mol/cm^3} \cdot 64450$ g/mol [108]	−2.61	−2.61
plasma proteins	χ_{prot} [a]	−0.587 $\mathrm{cm^3/g}$ [108]	$\times 4\pi$ / 0.730 $\mathrm{cm^3/g}$ [110]	−10.1	−10.1
difference between deoxygenated and oxygenated RBC	$\Delta\chi_{\mathrm{do}}$	0.27 [108,111]	$\times 4\pi \cdot 310.15\ \mathrm{K} / (T + 273.15)$	3.57	3.39

SI, International System of Units.

All sources were in cgs units.

[a] Aside from H_2O, the molar susceptibilities of the diamagnetic molecules were assumed to be temperature-independent [109].

[b] $\bar{v}_{M,\mathrm{O_2:H_2O}}$ is the partial molar volume of O_2 dissolved in water (see Section 4.9 for more details).

To account for dissolved O_2, SD divided χ_{blood} into contributions from O_2, with a volume fraction α_{O_2}, and from RBCs and plasma, with a volume fraction $(1 - \alpha_{O_2})$. For the volume fraction of O_2, they used $\alpha_{O_2} = \varepsilon \cdot pO_2$, where ε is the Bunsen solubility coefficient of O_2 in blood, which was taken to be 3.1×10^{-5} mL O_2/mL blood/mm Hg [32]. Crucially, this quantity, $\varepsilon \cdot pO_2$, is the volume that O_2 in blood would occupy as an ideal gas at standard temperature and pressure (STP) per mL of blood, it is *not* the physical volume fraction occupied by O_2 in blood [112]. In fact, when O_2 dissolves in a liquid such as blood or water, the volume occupied by the O_2 in solution is orders of magnitude less than the volume occupied by the same number of moles in the gaseous state at STP. Additionally, in this model, the contribution of dissolved O_2 to χ_{blood} is only valid for an average Hb concentration (and therefore Hct) [112]; however, the amount of O_2 that can be dissolved in blood is proportional to the amount of blood water, which in turn is dictated by Hct since it displaces plasma – the largest source of blood water. Therefore, SD's formulation considerably overestimated α_{O_2} and did not account for the effect that Hct has on the amount of O_2 that can dissolve in blood. We refer to this model for the susceptibility of dissolved O_2 as the ideal gas model (IGM).

To account for the volume of dissolved O_2 and Hct, we consider the O_2 dissolved in each water compartment of blood – specifically, the water in plasma and the water in RBCs [33] – since quantities such as the partial molar volume of O_2 dissolved in water are well documented and enable direct calculation of the change of water volume as a function of pO_2. The details for calculating α_{O_2} and the relevant susceptibilities are given in Sections 4.9 and 4.10, respectively.

When the formulations for χ_{RBC} and χ_{plasma} from Spees et al. [108] are modified such that the susceptibilities of the contributing components are all expressed using volume susceptibilities and the contribution from dissolved O_2 to the water compartment is added, we get

$$\chi_{\mathrm{RBC}} = \alpha_{\mathrm{Hb}}\,\chi_{\mathrm{diamHb}} + (1-\alpha_{\mathrm{Hb}})\left((1-\alpha_{\mathrm{O_2}})\chi_{\mathrm{H_2O}} + \alpha_{\mathrm{O_2}}\cdot\chi_{\mathrm{O_2}}\right) + (1-\mathrm{SbO_2})\cdot\Delta\chi_{\mathrm{do}} \tag{4.3}$$

and

$$\chi_{\mathrm{plasma}} = \alpha_{\mathrm{prot}}\,\chi_{\mathrm{prot}} + \left(1-\alpha_{\mathrm{prot}}\right)\left((1-\alpha_{\mathrm{O_2}})\chi_{\mathrm{H_2O}} + \alpha_{\mathrm{O_2}}\cdot\chi_{\mathrm{O_2}}\right). \tag{4.4}$$

In Eq. (4.3), α_{Hb} is the intracellular volume fraction of Hb and is equal to 0.266 [108], χ_{diamHb} represents the diamagnetic contribution to the susceptibility from each Hb molecule regardless of oxygenation state, $\Delta\chi_{\mathrm{do}}$ represents the susceptibility difference between fully oxygenated and fully deoxygenated RBCs (ignoring dissolved O_2), and SbO_2 is the fractional O_2 saturation of Hb. In Eq. (4.4), χ_{prot} is the susceptibility of plasma proteins and α_{prot}, the volume fraction of plasma proteins, is given by the product $w_{\mathrm{prot}}\,\rho_{\mathrm{plasma}}\,\bar{v}_{\mathrm{prot}} = 0.052$, where $w_{\mathrm{prot}} = 0.07$ is the assumed mass fraction of proteins in plasma [108], $\rho_{\mathrm{plasma}} = 1.026$ g/cm^3 [110], and $\bar{v}_{\mathrm{prot}} = 0.730$ cm^3/g is the partial specific volume of plasma proteins [110].

4.5 Methods

Susceptibility measurements were made in oxygenated samples of distilled water as well as *ex vivo* bovine plasma in a large water phantom for imaging. Details of the methods are given below.

4.5.1 Sample Preparation

Distilled water was used for the experiments in water and *ex vivo* bovine plasma (GeneTex, Inc., Irvine, CA) was used for the plasma experiments. The plasma composition was 8 g/dL of protein, a molality of 174.5 mmol/kg, <2 mg/dL of Hb, and 8 g/L of tri-sodium citrate (Na-citrate) anticoagulant. All measurements were conducted at room temperature.

For each water and plasma measurement, a 50-mL centrifuge tube was filled three quarters full with the liquid and sealed with a rubber septum and self-adhesive film. O_2 was bubbled through the liquid at a low flow rate (< 5 L/min) for 0 – 10 minutes using a catheter connected to a medical O_2 supply.

After bubbling, the sample was gently agitated to ensure uniform oxygenation. The oxygenated liquid was transferred via syringe to a 120-mm long, 15-mL polypropylene centrifuge tube with a 17-mm outer diameter that was also sealed with a rubber septum and self-adhesive film. Another needle was inserted in the tube such that as much air as possible could be expelled prior to imaging it.

Immediately after the transfer, the sample was imaged while the pO_2 of the remaining liquid in the large centrifuge tube was measured. pO_2 measurements were made with an Orion Star A323 dissolved O_2 meter connected to a photo-luminescence pO_2 probe (Thermo Fisher Scientific Inc., Waltham, MA).

4.5.2 MR Susceptometry

To measure the susceptibility of the samples, we used the relation between the susceptibility difference inside and outside the tube, $\Delta\chi = \chi_{\text{in}} - \chi_{\text{out}}$, to the Larmor frequency shift inside the tube, Δf_0, by approximating the tube as an infinite cylinder [52]:

$$\Delta f_0 = \frac{1}{6}\Delta\chi f_0(3\cos^2\theta - 1), \tag{4.5}$$

where f_0 is the centre frequency and θ is the angle the tube makes with the external field, $\mathbf{B_0}$. For small θ, the field offset outside of the tube is negligible.

Based on our theory, the expected difference in susceptibility between plasma at a pO_2 of 110 mm Hg (at normoxia) and at 550 mm Hg (upper range of hyperoxia challenges) is approximately 24 ppb. Using Eq. (4.5) with the tube aligned parallel to $\mathbf{B_0}$, this change in susceptibility would result in a frequency shift of only 1 Hz at 3 T, therefore the imaging protocol was designed to be sensitive to frequency shifts with a precision < 0.1 Hz.

To measure the frequency shifts across the phantom, we used multi-echo gradient recalled echo (GRE) imaging and used the linear relation between phase and frequency over time:

$$\phi(x, y, t) = 2\pi\Delta f_0(x, y) \cdot t + \phi_0(x, y), \tag{4.6}$$

where $\phi(x, y, t)$ is the phase at time t at the voxel with coordinates (x, y) and ϕ_0 is the phase offset immediately after excitation at that voxel.

4.5.3 MRI Data Acquisition

All imaging was on a 3-T Siemens TIM Trio system (Siemens, Erlangen, Germany) using the vendor-supplied 32-channel receive-only head coil. The prepared sample was placed along the axis of a plastic 4-L cylindrical phantom filled with distilled water as a reference medium while two poly(methyl methacrylate) (PMMA) inserts held the tube in place by its ends. The phantom was positioned in the head coil with the tube aligned parallel to the $\mathbf{B_0}$ field. A single slice, 2D multi-echo GRE sequence with monopolar readout was used for imaging. A 5-mm axial slice centred on the mid-point of the tube was acquired on a 256×256 matrix over a 200×200 mm^2 field of view. Imaging parameters were: 16 echoes, first echo time (TE) of 3.0 ms, 3.75-ms echo spacing, 500 Hz/pixel readout bandwidth, and a 90-ms repetition time (TR). The total acquisition time was 23 s. Prior to running the sequence, Siemens advanced shimming was performed on the slice.

For the plasma samples only, forcing all of the air bubbles out of the tubes was sometimes not possible; in this case, the phantom was tilted upwards slightly in order to shift the bubbles away from the imaging slice. For all plasma samples, therefore, an additional low-resolution 2D multi-slice GRE scan was acquired such that the tube angle could be measured on the magnitude images. This scan used the same imaging parameters as the single slice acquisition above except it used twenty 5-mm slices with a 1-mm slice gap, a 128×128 matrix, a single readout with TE = 20 ms, and a 500 ms TR.

4.5.4 Image Processing

All image processing was performed in MATLAB (The MathWorks Inc., Natick, MA). To accurately generate phase images for each echo, we reconstructed individual channel images using the multi-channel recombination method introduced by Robinson et al. [113]. We adapted their implementation to our data by using all 16 echoes at the full spatial resolution of the acquisition. The offset-corrected images were bound between $\pm\pi$ and were saved for processing in the main pipeline. Magnitude images were output from the scanner, using sum of squares reconstruction.

To calculate $\Delta\chi$ from the magnitude and offset-corrected phase images, the following steps were performed: temporal phase unwrapping, field map estimation, background field removal, and susceptibility calculation. These steps are summarized in Figure 4.1. First, the phase images were temporally unwrapped such that the phase values were no longer bound between $\pm\pi$. For the n-th echo, this was done by adding the phase of the product of the n-th complex image and the complex conjugate of the (n–1)-th complex image to the phase of the previously unwrapped image. The phase of the first echo was left unmodified.

After phase unwrapping, a field map, Δf_{meas}, was estimated by linearly fitting the phase over time on a voxel-wise basis using weighted least-squares. The squared magnitude image values were used as the fit weights [114]. The frequencies were given by the linear coefficients of the fits and maps of their estimated uncertainties, $\sigma_{\Delta f}$, were also produced.

To correct for macroscopic field inhomogeneities, Δf_{inhom}, a retrospective background field estimation method was used [115]. In the original method, a second-order 2D polynomial was fit to the field map across the entire phantom using weighted least-squares and subtracted from Δf_{meas} to produce a corrected map, Δf_{corr}. Prior to fitting, regions of interest (ROIs) covering the

tubes and the voxels whose values in the magnitude image were below a certain threshold were masked out such that the fit would not be influenced by the offset of interest in the tube and by unreliable frequency measurements, respectively.

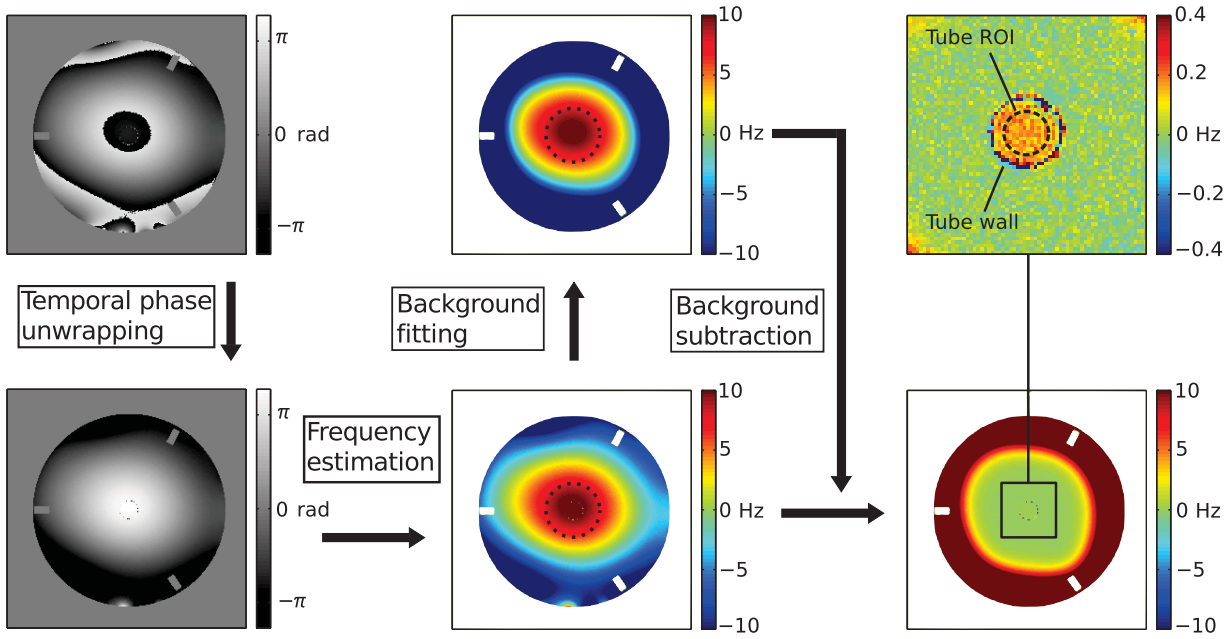

Figure 4.1: Schematic overview of the field mapping pipeline.

The pipeline converts the raw phase images to background-corrected frequency maps. The dotted black circle on the frequency maps in the centre column represents the boundary of the inclusion ROI within which the background field mapping was performed. The top right is a zoom-in of the background-corrected field map with the windowing adjusted to highlight the frequency difference inside and outside the tube. The dashed black circle within the zoom-in represents the boundary of the ROI in the tube over which the frequency values were averaged for determining $\Delta\chi$ with Eq. (4.5).

In our study, we found that fitting Δf_{inhom} across the entire phantom with a 2$^{\text{nd}}$-order 2D polynomial did not satisfactorily remove the inhomogeneity in the region of the tube since large frequency fluctuations near the phantom wall tended to skew the fit. Therefore, we tested higher-

order fits and restricted the fit to a 55-mm diameter inclusion ROI that was just over three-times the diameter of the tube (as shown in the centre column of Figure 4.1). A 6th-order 2D polynomial gave Δf_{corr} closest to 0, the lowest variance, and the highest adjusted coefficient of determination (R^2) of the fits when the phantom and the tube were both filled with distilled water and when no tube was present at all. To exclude voxels with low signal from the fit, a threshold corresponding to the maximum signal from any voxels with partial voluming with the tube wall was used. The weighting values for each voxel in the fit were given by $1/\left(\sigma_{\Delta f} + \lambda\right)^2$, where $\lambda = 1.6\times10^{-2}$ Hz prevented division by zero.

For each sample, Δf_{corr} at the centre of the tube was averaged over a 12-voxel diameter ROI, giving $\overline{\Delta f}_{\text{corr}}$ (ROI represented by the dashed black circle in the top-right field map in Figure 4.1). For the plasma samples, the tilt angle, θ, of the tube was measured by selecting three points along the axis of the tube on the low-resolution multi-slice image and then calculating the angle between the line of best fit through the points and $\mathbf{B_0}$. Finally, $\Delta\chi$ was calculated from Eq. (4.5) using $\Delta f = \overline{\Delta f}_{\text{corr}}$, the measured value of θ for plasma or $\theta = 0$ for water, and f_0 from the scanner (stored in the image headers). The uncertainty on $\Delta\chi$, $\sigma_{\Delta\chi}$, was estimated using standard error propagation methods with $\sigma_{\overline{\Delta f}_{\text{corr}}}$ equal to the standard deviation of Δf_{corr} in the tube ROI and $\sigma_\theta = 0.5°$ for all samples, including water.

We tested the validity of the background field removal and susceptibility calculation by performing Fourier-based forward field modelling on a digital representation of our phantom [85-87] using realistic susceptibility values for all the materials [116]. After fitting the generated background field to a 6th-order polynomial and subtracting this fit, the relationship between the remaining field shift inside the tube and the susceptibility difference between the liquid inside the

tube and outside the tube agreed with the infinite cylinder model to within 0.1% when the tube angle relative to $\mathbf{B_0}$ was varied from 0 to 5°. This was in agreement with other studies examining the range of validity of the infinite cylinder model [117,118].

4.5.5 Analysis

The measured values of $\Delta\chi$ in water and plasma were compared with the theory presented above using the pO_2 and temperature measurements from the oxygenated samples to calculate χ inside the tube, χ_{in}, and from the distilled water in the phantom to calculate χ in the surrounding water, χ_{out}. Equation (4.4) for χ_{plasma} was used for the calculations of both χ_{in} and χ_{out}: for the bovine plasma, α_{prot} was given by the product [protein] $\cdot\, \bar{v}_{\text{prot}} = 0.08$ g protein/cm^3 plasma $\times$ 0.730 cm^3 plasma/g protein = 0.058 and for water, α_{prot} was set to 0. For each set of measurements, the line of best fit for $\Delta\chi$ vs. pO_2 was found using a general least-squares approach that incorporated the uncertainty in both the pO_2 and $\Delta\chi$ measurements [119]. Differences between the measured and theoretically predicted slopes of $\Delta\chi/pO_2$ were tested for statistical significance using a two-tailed t-test. Additionally, the measured slopes in all three solutions were themselves compared for statistical differences using an analysis of covariance (ANCOVA) test.

Since the original model for χ_{blood} [108] did not use anti-coagulant nor did it account for the susceptibilities of electrolytes, an offset between the measured susceptibility in plasma and the theoretical predictions from Eq. (4.4) was present. To account for this offset, we incorporated electrolytes and Na-citrate into our calculations by assuming that they also dissolve in the water compartment of Eq. (4.4).

To account for Na-citrate, we measured its susceptibility in water using our technique described above by dissolving 8 g/L of it in distilled water (the same concentration as the bovine plasma). We also repeated our measurements of the effect of dissolved O_2 on the susceptibility of the Na-citrate solution by oxygenating the solution over a range of pO_2 values.

For the electrolytes, we assumed that Na^+ and Cl^- were the sole electrolytes contributing to the susceptibility since they constitute the majority of the electrolyte concentration in plasma [120]. Given a total molality of 174.5 mmol/kg in the plasma samples, we varied the molality of NaCl from 0 – 175 mmol/kg and determined which value resulted in the susceptibility offset that matched the measurements.

Finally, since the solubility coefficient of blood, ε, that the IGM used was measured for whole blood with normal Hb concentrations [112], it was not possible to compare it directly to our measurements in water and plasma. Since ε was based on the volume that all the moles of O_2 dissolved in blood would occupy as an ideal gas at STP, as a means of comparing this theory to our measurements, we first calculated the mole fraction and volume fraction in water/plasma using our theory, then converted these using the ideal gas law to the volume fraction that O_2 would occupy if the same number of moles were in the gaseous state:

$$\alpha_{\mathrm{O_2,\,IGM}} = \frac{\alpha_{\mathrm{O_2}}}{\bar{v}_{M,\mathrm{O_2{:}H_2O}}} \cdot \frac{R \cdot T_{\mathrm{stp}}}{\mathrm{P_{stp}}}, \tag{4.7}$$

where R = 82.06 (cm^3 atm)/(mol K) is the ideal gas constant, T_{stp} = 273.15 K, $\mathrm{P_{stp}}$ = 1 atm, and $\bar{v}_{M,\mathrm{O_2{:}H_2O}}$ is the partial molar volume of O_2 dissolved in water. For this comparison, we calculated $\chi_{\mathrm{O_2}}$ in the same manner as SD [23], described in Section 4.10.

4.6 Results

Oxygenating and scanning the samples was conducted at room temperature. The average temperature of the solutions was (22 ± 1) °C for distilled water, (23 ± 1) °C for distilled water with 8 g/L of dissolved Na-citrate, and (21.92 ± 0.08) °C for plasma. The reason for the variation in temperature ranges was that the distilled water experiments were performed on multiple days whereas the plasma samples were performed over several hours. The pO_2 and temperature of the water in the phantom was measured multiple times throughout the experiment and the average values were (151 ± 3) mm Hg and (21.1 ± 0.2) °C, respectively.

Using the multi-slice scans of the plasma samples, the average tilt angle of the tubes was (1.4 ± 0.8)° with a maximum angle of 2.7° with respect to $\mathbf{B_0}$.

An example of the field mapping and background field removal for a scan of an oxygenated water sample is shown in Figure 4.1. In the inclusion ROI used for fitting the background field, the typical estimated uncertainty on the frequencies was approximately (0.040 ± 0.008) Hz with a maximum uncertainty of 0.1 Hz and inside the tube was (0.036 ± 0.007) Hz with a maximum uncertainty of 0.05 Hz. This technique was therefore capable of measuring frequency offsets with our specified precision $\lesssim$ 0.1 Hz in our ROI.

Plots of $\Delta\chi$ vs. pO_2 for all three solutions are shown in Figure 4.2. Figure 4.2 also shows our model's predictions and the IGM's predictions for $\Delta\chi$ using the average temperature of each solution and the surrounding water in the phantom in the calculations of both. Note that in this figure the $\Delta\chi$ offsets for the theoretical predictions have been adjusted such that the lines intersect

with the lines of best fit at normoxia in order best visualize the differences in $\Delta\chi/pO_2$ slopes. We have labeled our theory with our initials "BMHP".

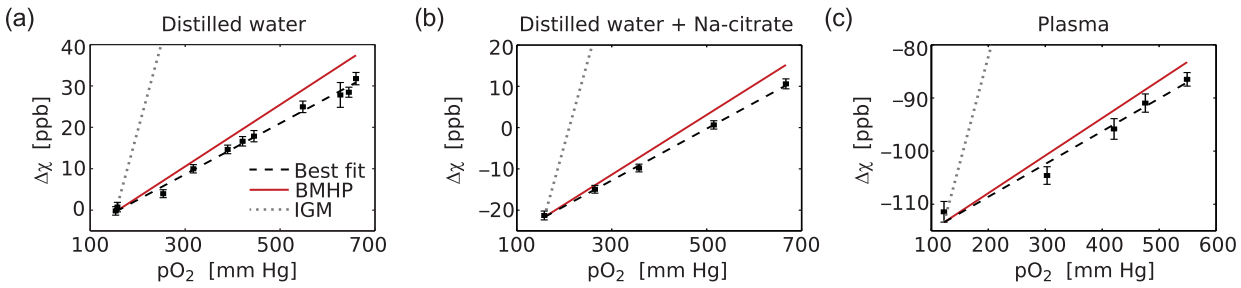

Figure 4.2: Measured susceptibilities with dissolved oxygen

Measured susceptibility differences (squares plus error bars) between oxygenated water (a), water + Na-citrate (b), and bovine plasma (c) and the surrounding water in the phantom. In each plot, the dashed black line is the line of best fit for the measurements, the solid red line is the predicted susceptibility difference using our theory (BMHP), and the solid grey line is the predicted susceptibility difference using the ideal gas model (IGM) employed by Schwarzbauer and Deichmann [23]. To better compare the effect of dissolved O_2, the vertical offsets of the theoretical predictions have been adjusted in the plots such that the lines intersect with the lines of best fit at normoxia. For clarity, the graphs' limits are constrained to the range of measured $\Delta\chi$ rather than the full range predicted by the IGM.

The regression coefficients for the measured data are shown in, Table 4.2 as well as the coefficients from our theory and the IGM. The far right column gives the coefficient of determination (R^2) for the lines of best fit; from these results and qualitatively from the plots in Figure 4.2, $\Delta\chi$'s dependence on pO_2 is obviously very linear for all three solutions.

From the $\Delta\chi$ measurements of distilled water with dissolved Na-citrate, we found the susceptibility of dissolved Na-citrate to be $\chi_{\text{Na-cit}} = (-12.1 \pm 0.2)$ ppm. For plasma, we used this value and tested the effect that dissolved Na-citrate and dissolved Na-citrate + NaCl had on the

slope and offset of our theory. We found that the added solutes had no measurable effect on the slope but large effects on the offset. When both solutes were included in the model, 125 mmol NaCl/kg plasma was the molality that produced the offset that best matched the measurements. This value is within an acceptable range, given a molality of 174.5 mmol/kg [120].

The most salient result was the discrepancy between the measured and modelled slopes of $\Delta\chi/pO_2$. We found that the IGM overestimated the slope by over 500%, whereas our theory produced a much more accurate prediction of the slope but still overestimated it by 14% – 21%.

Table 4.2: Susceptibility of dissolved oxygen fit results.

The coefficients of the linear fits of the measured and theoretical changes in $\Delta\chi$ vs. pO2 using our theory and the ideal gas model (IGM). Fits are of the form $\Delta\chi = m_{\Delta\chi} \cdot pO_2 + \Delta\chi_0$.

Solution	$m_{\Delta\chi}$ (ppb/mm Hg)	$m_{\Delta\chi}$ % difference	t-test (P)	$\Delta\chi_0$ (ppb)	$\Delta\chi_0$ % difference	R^2
water						
Measured	0.062 ± 0.002			–9.8 ± 0.8		0.993
BMHP	0.075	21	2×10^{-4}	–11	12	
IGM	0.42	580	3×10^{-17}	–65	560	
water + Na-citrate						
Measured	0.063 ± 0.003			–32 ± 1		0.998
BMHP + 8 g/L Na-citrate	0.072	14	0.06	–32	0	
IGM	0.41	550	2×10^{-6}	–62	94	
plasma						
Measured	0.062 ± 0.005			–121 ± 2		0.973
BMHP	0.071	15	0.09	–74.4	–39	
BMHP + 8 g/L Na-citrate	0.071	15	0.10	–95.4	–21	
BMHP + 8 g/L Na-citrate + 125 mmol/kg NaCl	0.071	15	0.10	–122	0.8	
IGM	0.40	550	7×10^{-6}	–129	7	

IGM, ideal gas model

[a]BMHP theory by Berman, Ma, Hoge, and Pike.

As demonstrated by the *P*-values in Table 4.2, the differences between the measured and our modelled slopes were statistically significant in water ($P = 2\times10^{-4}$) but not significant in water + Na-citrate nor in plasma ($P = 0.06$ and 0.10, respectively). At a pO_2 of 550 mm Hg in plasma, these errors in the slopes translated into errors in the susceptibility of 145 ppb using the IGM and 4.5 ppb using our theory. When we compared the three measured $\Delta\chi/pO_2$ slopes from water, water + Na-citrate, and plasma using an ANCOVA test, there was no significant difference between the three of them ($P = 0.8$).

Finally, the high degree of linearity between $\Delta\chi$ and pO_2 would suggest that the detailed model presented here could be further simplified. This is because the volume fraction of O_2, α_{O_2}, is extremely linear as a function of pO_2, so we can express it as $\alpha_{O_2} = \varepsilon' \cdot pO_2$, similar in form to the original IGM but with an empirically estimated constant of proportionality (ε'). Linearly fitting Eq. (4.8) vs. pO_2, we get $\varepsilon' = 5.42\times10^{-8}$ mL O_2/mL H_2O/mm Hg at 22 °C and 4.24×10^{-8} mL O_2/mL H_2O/mm Hg at 37 °C. Based on the measured slopes of $\Delta\chi/pO_2$, the corresponding values of χ_{O_2} to use would be (1140 ± 60) ppm at 22 °C and (1090 ± 50) ppm at 37 °C using Curie's law.

4.7 Discussion

Here we have introduced a new model for the susceptibility of blood that incorporates dissolved O_2 in the water compartments of blood and we have measured the change in susceptibility of plasma as a function of increasing pO_2. Previous studies have already evaluated the change in χ_{blood} for whole blood with pO_2 ranging from 0 up to ~120 mm Hg [108,111]; the work presented here complements these studies by considering the change in χ_{blood} over the hyperoxia range 120

mm Hg < pO_2 < 600 mm Hg. Plasma, rather than whole blood, was used here in order to disentangle dissolved O_2-induced susceptibility changes from Hb-induced susceptibility changes.

We found that the IGM for the susceptibility of dissolved O_2 dramatically overestimated the change in susceptibility in all three of the solutions we studied. This was due to the overestimation of the volume fraction of dissolved O_2, as described in the Theory section and Sections 4.9 and 4.10. Our model was in much better agreement with the measurements although it did slightly, but statistically significantly, overestimate the slope of $\Delta\chi/pO_2$ for water. We speculate that two separate factors may be contributing to the slightly decreased slope. The first is that, while Curie's law is sufficient for modelling the change in susceptibility for most paramagnetic molecules of interest in MRI, diamagnetic contributions to the susceptibility of O_2 from pairwise intermolecular interactions are greater with increasing molar density [121]. Our estimate of χ_{O_2} may not have fully accounted for the diamagnetic contribution since O_2 dissolved in liquid is actually at a much higher density than as a gas and our reference value for χ_{O_2} was measured with O_2 in its gaseous state at 1 atm [102].

In addition to intermolecular interactions having a potential impact on the diamagnetic contribution to χ_{O_2}, there is evidence for O_2–H_2O interactions that may affect the paramagnetism of χ_{O_2}. Dissolved O_2 has been found to add another ultraviolet absorption band to the spectra of organic solvents, including water [122]. It is believed that this is caused by a charge transfer effect in which O_2 behaves as an electron acceptor and the solvent molecules as electron donors. Given that O_2's paramagnetic behaviour is the result of it having two unpaired electrons, it is plausible that this charge transfer could fractionally reduce the effective number of unpaired electrons and, therefore, reduce the magnetic moment and paramagnetism of dissolved O_2. It is not clear how

much each of the above two mechanisms contribute to the observed minor discrepancy between theory and experiment and it is beyond the scope of this study.

If we briefly re-examine how increased dissolved O_2 in arterial blood may affect T_2^*-weighted imaging, it is best to put it in perspective with the changes occurring in venous blood. If a subject has average resting physiological conditions with arterial pO_2 = 110 mm Hg, Hct = 0.4, and O_2 extraction fraction = 0.35, then the venous SbO_2 will be 0.65. If arterial pO_2 increases to 550 mm Hg under hyperoxia and changes in O_2 metabolism and blood flow are considered negligible, then the venous SbO_2 will increase to 0.74 [32]. Using our model for χ_{blood} at 37 °C with χ_{O_2} = 1090 ppm, as measured, the expected change in the susceptibility of arteries would be –5.3 ppb*, whereas the change in veins would be –127 ppb. The change is more than 20 times larger in venous blood than in arterial blood, meaning that any possible signal change that may arise from $\Delta\chi$ in arteries would be dwarfed by the change resulting from veins. For comparison, the IGM predicted a change of +125 ppb in arteries. A scenario where arterial susceptibility changes may actually contribute more noticeably would be in the event of scanning extremely anemic patients during hyperoxia. Performing the analysis above but with Hct = 0.2, $\Delta\chi$ for arteries is +7.1 ppb and for veins is –98 ppb. In this case, caution may be required when interpreting BOLD signal changes from hyperoxia; however, for most physiological conditions, hyperoxia-driven T_2^* contrast will be dominated by dHb in veins and capillaries.

* Arteries show a negative change in susceptibility because at 110 mm Hg, SbO_2 is approximately 98% and at 550 mm Hg, it increases to essentially 100%. Therefore, the change in susceptibility from the 2% dHb converting to oxy-Hb outweighs the positive change in susceptibility from the added dissolved O_2.

4.8 Conclusion

We have presented a model for the susceptibility of blood that incorporates dissolved O_2 and we have experimentally validated the theory over a wide range of pO_2 values in distilled water and in plasma. We found that the change in susceptibility was marginally less than predicted and we have characterized the observed solubility of dissolved O_2 in water and its susceptibility such that they can easily be incorporated into future modelling. Most importantly, in contrast to previous predictions that overestimated the volume fraction of dissolved O_2 [23], our results indicate that the effect of dissolved O_2 on the susceptibility of blood is negligible, even at the highest levels of hyperoxia. This work shows that, except in some extreme physiological circumstances, the susceptibility of dissolved O_2 can generally be ignored in MRI studies employing hyperoxia.

4.9 Calculating the Volume Fraction of O_2 in Water

Here we describe how we calculate the volume fraction of dissolved O_2 in water, α_{O_2}, for a given pO_2. α_{O_2} can be given by the product of the mole fraction of O_2 dissolved in water, $\bar{n}_{O_2}$, and the partial molar volume of O_2 dissolved in water, $\bar{v}_{M,O_2:H_2O}$, all divided by the total molar volume of the O_2-water solution:

$$\alpha_{O_2} = \frac{\bar{n}_{O_2} \cdot \bar{v}_{M,O_2:H_2O}}{\bar{n}_{O_2} \cdot \bar{v}_{M,O_2:H_2O} + \left(1 - \bar{n}_{O_2}\right) v_{M,H_2O}}. \tag{4.8}$$

For the range of pO_2 encountered under normoxia and hyperoxia, the dissolved O_2-water solution is very dilute, therefore, the molar volume of H_2O (v_{M,H_2O}) is used in place of the partial

molar volume. $\bar{n}_{O_2}$ is obtained by Henry's law using an empirical formula for the reference $\bar{n}_{O_2}$ at atmospheric pressure [123]:

$$\bar{n}_{O_2}(\mathrm{pO_2}, T) = \exp\left(A + \frac{B}{(T + 273.15)} + C \ln\left((T + 273.15) \cdot 100\ \mathrm{K^{-1}}\right)\right) \cdot \frac{\mathrm{pO_2}}{760\ \mathrm{mm\ Hg}}, \tag{4.9}$$

with A = –66.7354, B = 8747.55 K, C = 24.4526, and T is the temperature in degrees Celsius. $\bar{v}_{M,O_2:H_2O}$ can be obtained empirically by the formula $\bar{v}_{M,O_2:H_2O}(T) = (31.7 - 0.04\ ^\circ\mathrm{C^{-1}} \cdot T)\ \mathrm{cm^3/mol}$ [124]. Over the range of pO_2 explored in this study, the ratio of $\varepsilon \cdot pO_2/\alpha_{O_2}$ at 37 °C remains relatively constant at 731. For example, when pO_2 = 500 mm Hg and T = 37 °C, Eq. (4.8) gives a volume fraction for dissolved O_2 of 2.12×10^{-5}, whereas in the IGM, $\varepsilon \cdot 500$ mm Hg = 1.55×10^{-2}.

To test the agreement of these calculations with the established solubility coefficient of O_2 in blood at STP, when α_{O_2} for a given pO_2 is converted back to the *gaseous* volume of O_2 relative to *water* volume using Eq. (4.7) and then converted to the gaseous volume of O_2 relative to *blood* volume using Eq. (5) from [112], we end up with a Bunsen solubility coefficient of O_2 in blood equal to 3.13×10^{-5} mL O_2/mL blood/mm Hg. This is in perfect agreement with the original value given in [32,112].

4.10 Details of Susceptibility Calculations

Here we layout in detail how the susceptibilities of several of the constituents of blood and our experimental samples were calculated.

As shown in Table 4.1, the molar susceptibility of O_2 is governed by Curie's law and is therefore inversely proportional to temperature. We converted to volume susceptibility by dividing the molar susceptibility by the partial molar volume of O_2, whereas in the IGM, the molar susceptibility was divided by the molar volume of gaseous O_2 at 1 atm and 37 °C. The result is that χ_{O_2} is actually significantly larger in our model and the product $\alpha_{O_2}\chi_{O_2}$ works out to be roughly the same for our two models. However, since α_{O_2} in the IGM is overestimated, the factor $(1-\alpha_{O_2})$ significantly reduced the contribution of the remaining constituents of χ_{blood}.

For the susceptibility of water, it has been shown that there exists a slight temperature dependence, such that χ_{H_2O} is given by [125]

$$\chi_{H_2O}(T) = \frac{4\pi(-12.96\times10^{-6}\ \text{cm}^3/\text{mol})}{v_{M,H_2O}(T)} \times(1 + D\cdot(T-20) + E\cdot(T-20)^2), \tag{4.10}$$

where D = 1.38810×10^{-4} °C^{-1}, E = –1.2685×10^{-7} °C^{-2}, and 4π (–12.96×10^{-6}) cm^3/mol is the molar susceptibility of H_2O at 20 °C [102]. Spees et al. [108] did not account for this temperature dependence, therefore, our values for χ_{H_2O} differ slightly.

In order to measure Na-citrate's susceptibility in distilled water and to incorporate this into the susceptibility of the plasma samples, the mole and volume fractions of Na-citrate in the samples were calculated using a molecular mass of 294.10 g/mol and a partial molar volume of 69.32 cm^3/mol [126]. Similarly, for NaCl we used a partial molar volume of 16.3 cm^3/mol at 22 °C [127] to help convert the molality to a volume fraction and to convert from molar susceptibility to get a volume susceptibility of –23.2 ppm [102].

Chapter 5

Transverse Signal Evolution in Blood

5.1 Preface

HAVING determined the *microscopic* contributions of oxygen to the susceptibility of blood, the next aim was to analytically describe the signal evolution from blood due to molecular diffusion through the *mesoscopic* field inhomogeneities produced by partially deoxygenated red blood cells in plasma. Given the success of the weak field approximation of Jensen and Chandra for fitting T_2 relaxometry data from blood [76,78,80,81] and its algebraic simplicity, it was used in this study to derive a closed-form solution of signal evolution under any arbitrary train of 180° refocusing pulses (including a single spin echo or free induction decay).

The derived closed-form solution was validated using simulations of the transverse magnetization from distributions of spheres, as described in Chapter 3. Although spheres have been used as a simple geometric approximation of red blood cells [10,70], the motivation for their use here was that they have an exact analytical solution for the parameters of the weak field

approximation, making it possible to predict the simulated time courses *a priori* with the closed-form solution. One set of analyses was intentionally kept general because the theory of the weak field approximation has been used to model signal relaxation from tissues other than blood, such as brain and liver iron [76,128]. It is finally shown how the analytical parameters that were derived for the weak field approximation break down at high volume fractions when spheres cannot overlap, as may be the case for a typical hematocrit of blood. However, it was possible to empirically derive these parameters and recover the agreement for volume fractions up to ≈ 40%. This last finding holds promise for employing the weak field approximation to describe signal from systems of perturbers with more complex geometries and spatial distributions, such as more realistic red blood cell shapes or iron depositions in brain tissue or liver, where analytical expressions for the weak field parameters may not be readily determined. This chapter is based on a manuscript prepared for *Journal of Magnetic Resonance*.

Transverse signal decay under the weak field approximation: theory and validation for spherical perturbers

Avery J.L. Berman[1,2] and G. Bruce Pike[1,2,3]

[1]Department of Biomedical Engineering, McGill University, Montreal, Canada

[2]Hotchkiss Brain Institute, University of Calgary, Calgary, Alberta, Canada

[3]Departments of Radiology and Clinical Neurosciences, University of Calgary, Calgary, Alberta, Canada

Prepared for Journal of Magnetic Resonance

5.2 Abstract

Purpose

To derive a general expression for the transverse signal time course in a system of magnetic perturbers in the motional narrowing regime. This was examined with a focus on modelling intravascular signal decay.

Theory and Methods

A closed-form solution (CFS) for transverse signal decay under any train of refocusing pulses was derived using the weak field approximation. The CFS was validated via simulations of spins diffusing in the presence of spherical perturbers with a range of sizes, magnetic susceptibilities, and distributions.

Results

The CFS was valid in the motional narrowing regime and partially into the intermediate dephasing regime. When compared to a well-known expression for the transverse decay rate, fits to the CFS were in excellent agreement for multi-echo spin echo sequences but diverged for free induction decay. The CFS accurately predicted the signal decay at high volume fractions of non-overlapping spheres – like the hematocrit of blood – when the volume fraction and the characteristic perturber length were appropriately scaled.

Conclusion

Transverse signal decay in the motional narrowing regime can be accurately described analytically. This theory has applications in areas such as quantitative tissue iron imaging, relaxometry of blood, and contrast agent imaging.

Keywords

transverse relaxation; CPMG; magnetic inhomogeneities; blood; diffusion

5.3 Introduction

Understanding the detailed nature of transverse signal decay in the presence of magnetic perturbations plays an important role in many fields of MRI: from deriving baseline physiological parameters related to the blood oxygenation level-dependent (BOLD) signal [5] to quantifying structural properties of bone [129]. In the presence of magnetic perturbers, it is well known that the observed T_2 or T_2^* relaxation times depend on several factors, such as the perturbation magnitude (i.e., field strength and magnetic susceptibility offset between the perturbers and the surrounding medium), the interplay between molecular diffusion and the spatial scale of the perturbers, and the refocusing rate in a multi-echo spin echo sequence [60,130]. Depending on the combination of these parameters, the system is said to be in one of three dephasing regimes: static dephasing, motional narrowing, or an intermediate dephasing regime, with each regime displaying unique signal characteristics.

For RBCs in blood, the shape and size of the cells and the diffusion coefficient of blood water have relatively low variability, such that the system exists in the motional narrowing regime. In the motional narrowing regime, the characteristic time for a water molecule to diffuse the length of a perturber is much less than the time for a spin at the surface of a perturber to dephase [131]. Using an algebraic approximation for the temporal correlation function, Jensen and Chandra [76] derived an expression for how the transverse signal decay rate would change (ΔR_2) in a random distribution of perturbers as a function of the refocusing interval in a Carr-Purcell-Meiboom-Gill (CPMG) acquisition. This model is referred to as the weak field approximation (WFA). Following an alternative approach known as the Gaussian phase approximation, Sukstanskii and Yablonskiy

[131] derived a closed-form solution for how the transverse signal would evolve during free induction decay (FID) and as a function of spin echo (SE) time in a single SE type measurement. This derivation resulted in the same ΔR_2 as in the FID limit for spheres from the weak field approximation. The WFA has successfully been applied to model relaxometry results from ex vivo blood samples [76,78,80,81] and in vivo tissue non-heme iron depositions, also known as magnetic field correlation imaging [76,128].

Many of the theories describing relaxation in the different dephasing regimes [5,76,131], including the WFA, assume that the positions of the perturbers are uncorrelated. This leads to the unrealistic scenario where perturbers can physically overlap. At low perturber volume fraction, the amount of overlap is negligible, however, at higher volume fractions (e.g. ~40–45% hematocrit in blood), this is not the case. In exchange theory [75] and in more recent diffusion models of relaxation [74,79], this has been overcome by scaling the volume fraction of the perturbers, ζ, with the volume fraction of the surrounding medium, $1 - \zeta$. While this scaling is particularly important for accurately describing relaxation from blood, where ζ is on the order of 40%, the experimental evidence to support this scaling factor is limited and difficult to tease apart from other contributions to relaxation such as the intrinsic relaxation rates of the perturbers and medium [78,82,132].

The WFA has typically been used to compare its predictions of ΔR_2 with in vivo experiments or simulations to make inferences on the underlying physiology. With the increasing use of SE-based pulse sequences that sample away from the spin echo itself, such as asymmetric spin echo [133], gradient echo sampling of the spin echo [134], and gradient echo sampling of FID and echo [69], it is important to be able to compare the measurements with the entire predicted time course, rather than solely the signal observed at the spin echoes. Here we present a closed-form solution describing the complete transverse signal time course for an arbitrary number of

refocusing pulses using the weak field approximation. We compare the solution to the asymptotic solution for ΔR_2 and to simulations from networks of spheres over a range of conditions, including when the spheres overlap or not.

5.4 Theory

Following the derivation of the WFA from Jensen and Chandra [76], for a system of hydrogen nuclei subjected to a spatially varying magnetic field, the total field along the longitudinal direction at a point $\boldsymbol{r}$ is given by the sum of the main magnetic field, B_0, and an inhomogeneous component, $\Delta B(\boldsymbol{r})$. The spatial variation of this field can be described by an average over the inhomogeneous component for all pairs of points, $\boldsymbol{r}$ and $\boldsymbol{r'}$, referred to as the spatial correlation function:

$$C(\boldsymbol{r} - \boldsymbol{r}') = \langle \Delta B(\boldsymbol{r}) \Delta B(\boldsymbol{r}') \rangle_{\text{fld}}, \tag{5.1}$$

where $\langle \cdots \rangle_{\text{fld}}$ denotes the average over the field inhomogeneities in space. Due to molecular diffusion through the field over time, C will effectively vary over a time interval Δt and is described by the temporal correlation function, $K(\Delta t)$:

$$K(|\Delta t|) = \langle \Delta B[\boldsymbol{r}(t)]\, \Delta B[\boldsymbol{r}(t + \Delta t)] \rangle_{\text{fld+diff}} = \langle C[\boldsymbol{r}(t)] - C[\boldsymbol{r}(t + \Delta t)] \rangle_{\text{diff}}, \tag{5.2}$$

where the average is over space and all possible diffusion trajectories.

For a system of spins in the motional narrowing regime, diffusion across the field inhomogeneities reduces the transverse signal magnitude, $S'(t)$, at time t during a CPMG experiment [76,131]:

$$S'(t) = \exp\left\{-\frac{\gamma^2}{2}\int_0^t d\tau \int_0^t d\tau' \sigma(\tau)\sigma(\tau')K(|\tau - \tau'|)\right\}, \tag{5.3}$$

where $\sigma(t)$ is a spin flip function of magnitude 1 and which changes sign upon application of any 180° refocusing pulses.

Although analytic expressions for $K(t)$ for systems of spheres and infinite cylinders exist [76,131], deriving an exact expression for $K(t)$ is, generally, only tractable for simple geometries. A relatively simple form can be derived by considering the angular average of $C(\boldsymbol{r})$ and assuming it decays monotonically towards 0 as $r \to \infty$. By assuming that this radial correlation function, $G(r)$, decays as a quadratic exponential, i.e.,

$$G(r) = \frac{1}{4\pi}\int_0^{\pi} d\theta \int_0^{2\pi} d\phi \sin\theta\, C(r,\theta,\phi) = G_0 e^{-(r/r_c)^2}, \tag{5.4}$$

where $G_0 = C(0)$ is the mean square field inhomogeneity and r_c is a characteristic length that depends on the exact description of the perturbers, then, for unrestricted and isotropic diffusion in three-dimensions, $K(t)$ will take the algebraic form [76]

$$K(t) = G_0\left(1 + \frac{4Dt}{r_c^2}\right)^{-\frac{3}{2}}, \tag{5.5}$$

where D is the diffusion coefficient of water. This derivation assumes that the object is finite in three-dimensions, or more practically, that the field changes quickly relative to diffusion along any direction. Therefore, it cannot describe the correlation function for long cylinders, which are frequently used to model blood vessels, or broad disks. Using (5.5) and assuming that $S'(t)$ decays monoexponentially as $t \to \infty$, an asymptotic solution for ΔR_2 is [76]

$$\Delta R_2 = G_0 \frac{\gamma^2 r_c^2}{2D} F\left(\frac{2D\tau_{180}}{r_c^2}\right), \tag{5.6}$$

where τ_{180} is the CPMG refocusing interval and F is [76]:

$$F(x) = \frac{1}{\sqrt{\pi}} \int_0^\infty dy \frac{e^{-y}}{\sqrt{y}} \left[1 - \frac{1}{xy} \tanh(xy)\right]. \tag{5.7}$$

Using the correlation function in Eq. (5.5), it is also possible to explicitly solve the integral in Eq. (5.3) to produce a closed-form solution (CFS) for the signal magnitude at any time, t. If no refocusing pulses are applied, then the solution of this integral gives the FID signal:

$$S'(t) = \exp\left\{-\frac{\gamma^2}{2} G_0 \tau_D^2 \times \left[\frac{t}{\tau_D} - \left(\frac{1}{4} + \frac{t}{\tau_D}\right)^{\frac{1}{2}} + \frac{1}{2}\right]\right\}, \tag{5.8}$$

where $\tau_D \equiv r_c^2/D$ is the characteristic time for water molecules to diffuse over twice the characteristic length scale. In the case of a SE or CPMG sequence, this equation holds for $t < {}^1/_2\ \tau_{180}$. This and the following expression were recently independently derived [135]. After one refocusing pulse, we get

$$\begin{aligned} S'(t) = \exp\Bigg\{ & -\frac{\gamma^2}{2} G_0 \tau_D^2 \\ & \times \left[\frac{t}{\tau_D} + \left(\frac{1}{4} + \frac{t}{\tau_D}\right)^{\frac{1}{2}} + \frac{3}{2} - 2\left(\frac{1}{4} + \frac{t - \tau_{180}/2}{\tau_D}\right)^{\frac{1}{2}}\right. \\ & \left. - 2\left(\frac{1}{4} + \frac{\tau_{180}/2}{\tau_D}\right)^{\frac{1}{2}}\right]\Bigg\}, \end{aligned} \tag{5.9}$$

where $t > {}^1/_2\ \tau_{180}$ if only one refocusing pulse is applied or ½ $\tau_{180} < t < {}^3/_2\ \tau_{180}$ if another pulse is applied at $t = {}^3/_2\ \tau_{180}$. Continuing in this manner, the CFS after N refocusing pulses can be deduced [136]:

$$
\begin{aligned}
S'(t) = \exp\Bigg\{ & -\frac{\gamma^2}{2} G_0 \tau_D^2 \\
& \times \Bigg[\frac{t}{\tau_D} + (-1)^{N+1} \left(\frac{1}{4} + \frac{t}{\tau_D} \right)^{\frac{1}{2}} + \frac{1}{2} + N \\
& + \sum_{n=1}^{N} 2(-1)^{N-n+1} \left(\frac{1}{4} + \frac{t - (2n-1)\tau_{180}/2}{\tau_D} \right)^{\frac{1}{2}} \\
& + 2(-1)^n \left(\frac{1}{4} + \frac{(2n-1)\tau_{180}/2}{\tau_D} \right)^{\frac{1}{2}} \\
& + 4(-1)^n (N-n) \left(\frac{1}{4} + \frac{n\tau_{180}}{\tau_D} \right)^{\frac{1}{2}} \Bigg] \Bigg\}.
\end{aligned}
\tag{5.10}
$$

This expression holds even if no more pulses are applied after the N-th refocusing pulse and the system proceeds to evolve freely as an FID.

5.5 Methods

The evaluation of Eq. (5.10) was implemented in MATLAB R2015a (MathWorks, Natick, MA) using a function handle that was updated at each refocusing pulse and that iteratively added the terms in the summation to itself up to the N-th pulse. As written, Eq. (5.10) represents a general solution for transverse signal decay that could apply to a variety of systems given appropriate values for r_c and G_0 and that the conditions of the WFA are satisfied. To assess the validity of the CFS with concrete values, we considered spherical perturbers, for which r_c and G_0 are known. Also, given our aim of using the CFS to describe intravascular signal decay, where RBCs are the

principal magnetic perturbers, modelling the perturbers as spheres is a common first approximation. For spheres of radius R and with a susceptibility offset ($\Delta\chi$) relative to the external medium, r_c and G_0 are [76]

$$r_c = \left(\frac{4}{\pi\sqrt{3}}\right)^{\frac{1}{3}} R, \tag{5.11}$$

and

$$G_0 = \frac{4}{5}\zeta B_{eq}^2, \tag{5.12}$$

where ζ is the volume fraction occupied by the spheres and B_{eq} is the maximum field offset at the equator of a sphere and perpendicular to B_0, given by $B_{eq} = B_0\Delta\chi / 3$ (using SI units for $\Delta\chi$). Note that the WFA assumes that the positions of the spheres are uncorrelated, which allows for the possibility of overlapping spheres.

5.5.1 Simulations

To assess the accuracy of the CFS, we compared it to simulations of the transverse MR signal from networks of randomly positioned spheres using MATLAB. The simulations were performed using the deterministic diffusion method in three-dimensions [71], described in detail in Chapter 3. This is a computationally efficient simulation technique and it inherently models the perturber boundaries as freely permeable, as required by the WFA.

The field offsets generated by each sphere were given by

$$\Delta B(r) = \begin{cases} B_{eq}\left(\frac{R}{r}\right)^3 (3\cos^2\theta - 1) & r > R \\ 0 & r \leq R \end{cases}, \tag{5.13}$$

where θ is the angle between $\boldsymbol{B_0}$ and the line joining the centre of a sphere and a point a distance r from the sphere centre. The field offsets for each sphere were independently calculated and summed across the lattice.

Using this simulation framework, the accuracy of the CFS was examined across the dephasing regimes and then more specifically in the context of modelling intravascular signal. Unless stated otherwise, common simulation settings for both cases included B_0 = 3 T, time step δt = 0.25 ms, total simulation time = 80 ms, D = 2.7 μm^2/ms to approximate free water diffusion in plasma at 37 °C [137], and intrinsic T_2 relaxation was ignored.

5.5.2 General Validation of the Closed-Form Solution

To evaluate the general validity of the CFS across dephasing regimes, the simulations were run on networks where the sphere radii were increased from 1.5 μm up to 40 μm with ζ held constant at 3%. Δχ of the spheres was set to 1.2 ppm, which is equivalent to the susceptibility offset between 60% oxygenated RBCs and plasma (see Eq. (5.14) below). Under these settings, the parameter typically employed to classify the dephasing regime, $\alpha = \tau_D \delta\omega = r_c^2/D\,\gamma B_{eq}$, varies from 0.22–160, where $\alpha \ll 1$ defines the motional narrowing regime, $\alpha \gg 1$ defines the static dephasing regime, and $\alpha \sim 1$ represents the intermediate regime. Simulated pulse sequences included FID, spin echo (echo time = 80 ms), and CPMG using τ_{180} = 40 or 10 ms, resulting in 2 or 8 echoes, respectively. For networks where the sphere radius was less than 3 μm, the time step needed to be decreased to 0.05 ms to properly sample the diffusion effects in the field offsets around the perturbers; for larger

radii, time steps less than 0.25 ms negligibly affected the simulations. These simulations were performed on 10 randomly seeded networks of 1.5-μm radius spheres on a 600^3 lattice with a side length of 154 μm isotropic. These networks were reused for the larger radii by assigning them an effective lattice size of 154 μm × R/1.5 μm.

5.5.3 Validation of the Closed-Form Solution to Model Intravascular Signal

To evaluate the specific ability of the CFS to model decay as the volume fraction increased to levels comparable to the hematocrit of blood, the sphere radius was fixed at 3 μm and a range of volume fractions were tested to better reflect realistic blood hematocrit values. Simulations were only run using a τ_{180} of 40 ms since this adequately allowed for both FID and spin echo characteristics to be observed. Multiple field offsets were considered by using blood oxygen saturations (SO_2) of 0.6, 0.7, 0.8, and 0.9 and calculating $\Delta\chi$ using

$$\Delta\chi = \Delta\chi_{do}(\mathrm{SO}_{2,\mathrm{ref}} - \mathrm{SO}_2), \tag{5.14}$$

where $\Delta\chi_{do}$ = 4π·0.27 ppm is the susceptibility difference between fully deoxygenated and fully oxygenated RBCs, and $SO_{2,ref}$ = 0.95 is the oxygen saturation at which the susceptibility of RBCs and plasma are matched [103,138]. These SO_2's resulted in $\Delta\chi$ from 1.2 ppm down to 0.17 ppm.

Three sets of random perturber distributions were considered: one set where spheres could overlap and two sets where overlap was not allowed. The first non-overlapping distribution, referred to here as "random non-overlapping", was generated by randomly placing the spheres without overlap, until the desired ζ was reached. This method of distributing the spheres could generally only reach a volume fraction of ~40% before there were no more spaces available to place new spheres without overlap. The second distribution of non-overlapping spheres was

generated by randomly placing the spheres on a hexagonal close packed (HCP) lattice until the desired ζ was reached. With the HCP arrangement, the maximum possible packing was $\zeta \approx 74\%$. Examples of the three distributions at $\zeta = 40\%$ are given in Figure 5.1. These simulations were carried out with ζ between 3% and 60% (where possible) on 8 different networks per ζ-value on a 200^3 lattice with a side length of 150 μm isotropic.

5.5.4 Analysis

Prior to comparing the simulations with the CFS in Eq. (5.10), the simulations were averaged across all random networks for each set of run parameters (e.g. ζ, τ_{180}, $\Delta\chi$). Each set of signals was compared by examining the root mean square error (RMSE) between the time series as well as ΔR_2. ΔR_2 was calculated at the final time point, echo time (TE) = 80 ms, using $\Delta R_2 = -\ln(S)/TE$.

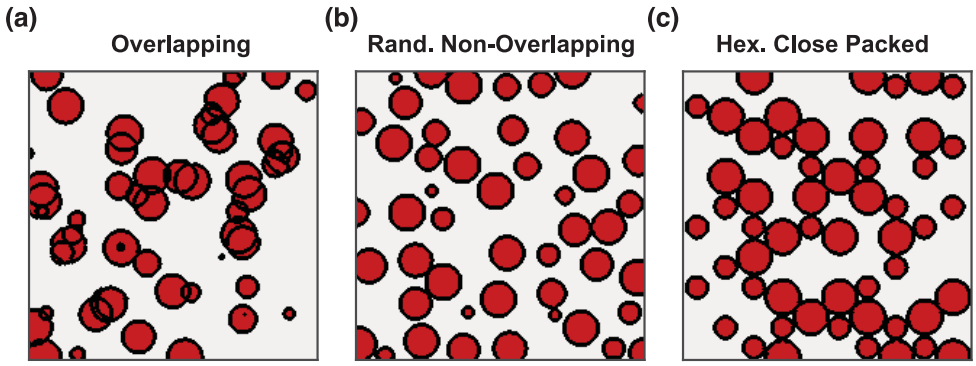

Figure 5.1: Example cross-sections through the sphere distributions.

The three three-dimensional distributions were all popoulated to 40%. (a) The overlapping distribution where the sphere positions were uncorrelated and hence allowed to overlap. (b) The random non-overlapping distribution where sphere positions were randomly assigned without overlap until the desired volume fraction was reached. (c) The hexagonal close packed distribution where the spheres were randomly assigned to the lattice elements of a hexagonal close packed distribution until reaching the desired volume fraction. The sphere boundaries are emphasized in black to highlight the differences between the distributions.

For the specific case examining non-overlapping perturbers, the simulations diverged from the CFS as ζ was increased. This behaviour has been described previously and it has been suggested that the volume fraction, ζ, be replaced by an apparent volume fraction $\zeta' = \zeta(1 - \zeta)$ to account for this [75,79]. If correct, then the parameter G_0, which represents the mean square field inhomogeneity, should exhibit a quadratic dependence on ζ, rather than the linear one in Eq. (5.12). In addition to G_0, the characteristic perturber length, r_c, was also introduced in Eq. (5.4) in the context of the radial correlation function, $G(r)$, and it is, in theory, only dependent on the perturber radius, although it is speculated to have some ζ-dependence [139]. To verify these hypotheses, $G(r)$ was computed for all the simulation networks using the discretized ΔB_{klm} and then fit to Eq. (5.4), from which G_0 and r_c were determined. These fitted G_0 and r_c values were then substituted into the CFS to compare its agreement with the simulations.

5.6 Results

5.6.1 Closed-Form Solution Vs. Monoexponential Decay

Examples of the CFS for multiple refocusing intervals are shown in Figure 5.2 and are plotted along with the monoexponential decay described by Eq. (5.6). These curves were generated as described in the Methods section where the spheres approximated RBCs with $\zeta = 40\%$, radius = 3 μm, and $SO_2 = 60\%$. Figure 5.2 shows an enlargement of the CFS and the monoexponential curve for the case $\tau_{180} = 10$ ms; the points of maximal refocusing are shifted significantly earlier in time than the spin echo times and the monoexponential curve does not pass through them. Despite this offset, when at least three spin echoes from the CFS were fit to a monoexponential decay, the fitted ΔR_2 values were within 2% of those predicted by Eq. (5.6) for the ranges $\tau_{180} = 1$–75 ms and $D = 0.5$–4 $\mu m^2/ms$, as shown in Figure 5.2c. For the FID, it is evident from Figure 5.2a that the CFS initially diverges from monoexponential decay and gradually reaches it. Thus, values of ΔR_2^* from the monoexponential expression significantly overestimate the ΔR_2^* estimated using up to ten echoes from the CFS, particularly at short echo spacings (Figure 5.2d).

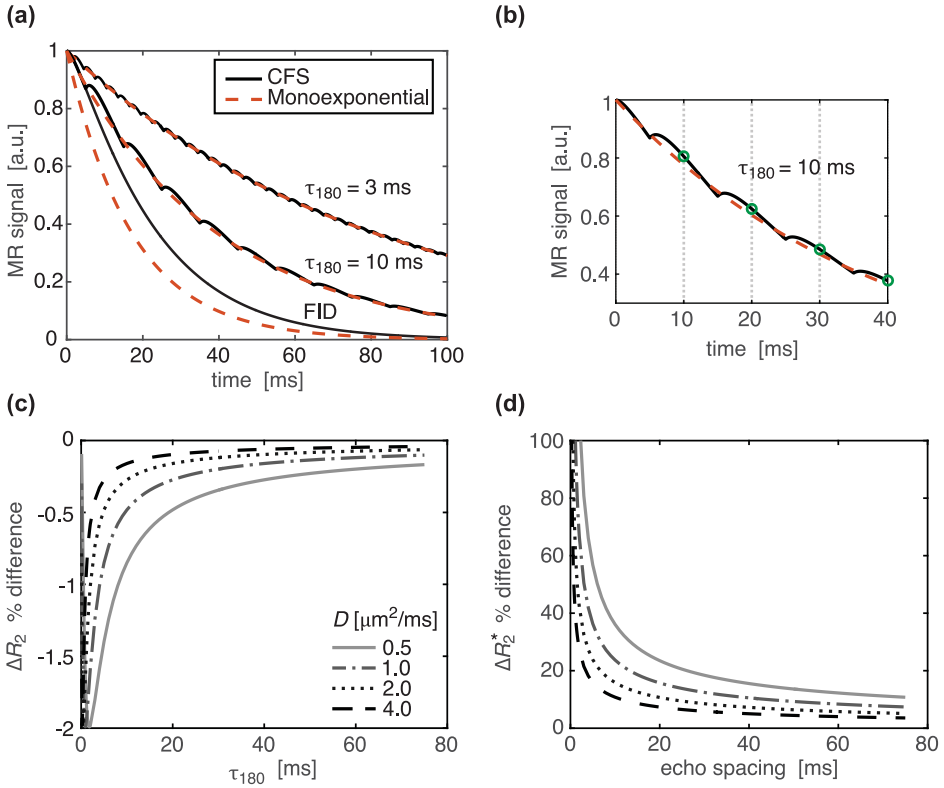

Figure 5.2: Comparions of the closed-form solution vs. the monoexponential approximation.

The CFS in Eq. (5.10) and the monoexponential approximation in Eq. (5.6) from Jensen and Chandra [76] were calculated for spheres in blood using $\zeta = 40\%$, $R = 3$ μm, $D = 2.7$ μm^2/ms, and $SO_2 = 60\%$, unless specified otherwise. (a) Example time series for two τ_{180} values and for an FID. (b) The $\tau_{180} = 10$ ms time series is expanded to highlight some of the characteristics of the CFS, such as the shift in the maximal refocusing points and the differences between it and the monoexponential approximation. (b) shares the same legend as (a), and the green markers represent the CFS signal at the spin echo times. (c) and (d) The percent differences between $\Delta R_2^{(*)}$ estimated from the monoexponential curve and the CFS shown for several diffusion coefficient values and as a function of echo spacing. (c) Comparison of the CPMG signals where ΔR_2 from the CFS was estimated using three echoes. (d) Comparison of the FID signals, where ΔR_2^* from the CFS was estimated using ten echoes. (c) and (d) share the same legend. CFS = closed-form solution, ζ = volume fraction, R = radius, D = diffusion coefficient, SO_2 = oxygen saturation.

5.6.2 General Validation of the Closed-Form Solution

Figure 5.3 compares the simulated FID and τ_{180} = 40 ms time series against the closed-form solution for several radii. The agreement between simulation and CFS is close for the 1.5-µm radius but for the 40-µm radius, the CFS significantly overestimates the decay. At the 5.2-µm radius, the agreement is also close but the decay is slightly overestimated by the CFS. These three radii demonstrate the transition from the motional narrowing regime to the static dephasing regime and Figure 5.4, which compares ΔR_2 and the RMSE between the simulations and the CFS, shows this transition in its near entirety.

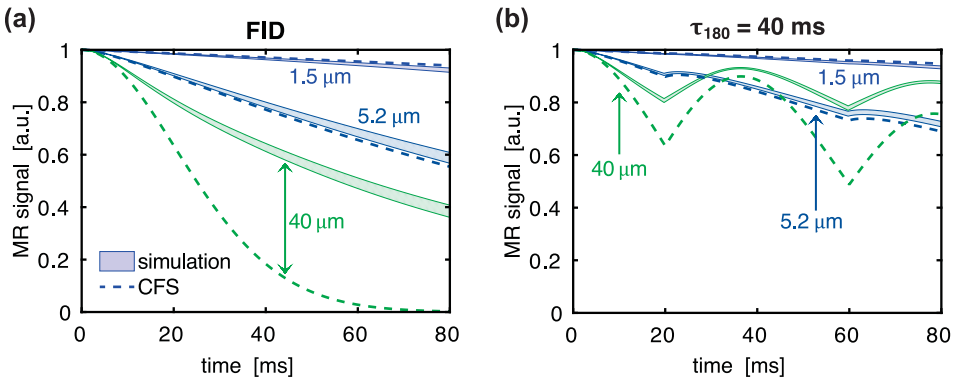

Figure 5.3: Comparison of the mean simulated signals vs. the CFS for select sphere radii.
Simulated FID (a) and CPMG (b) sequences shown. The shaded bands represent the mean ± standard deviation of the simulated signals and the dashed lines represent the CFS for each radius.

5.6.3 Modelling Intravascular Signal

To consider the CFS's ability to model intravascular signal, it was compared against simulations where the sphere radius was set to 3 µm. Above, the CFS was found to be in good agreement when

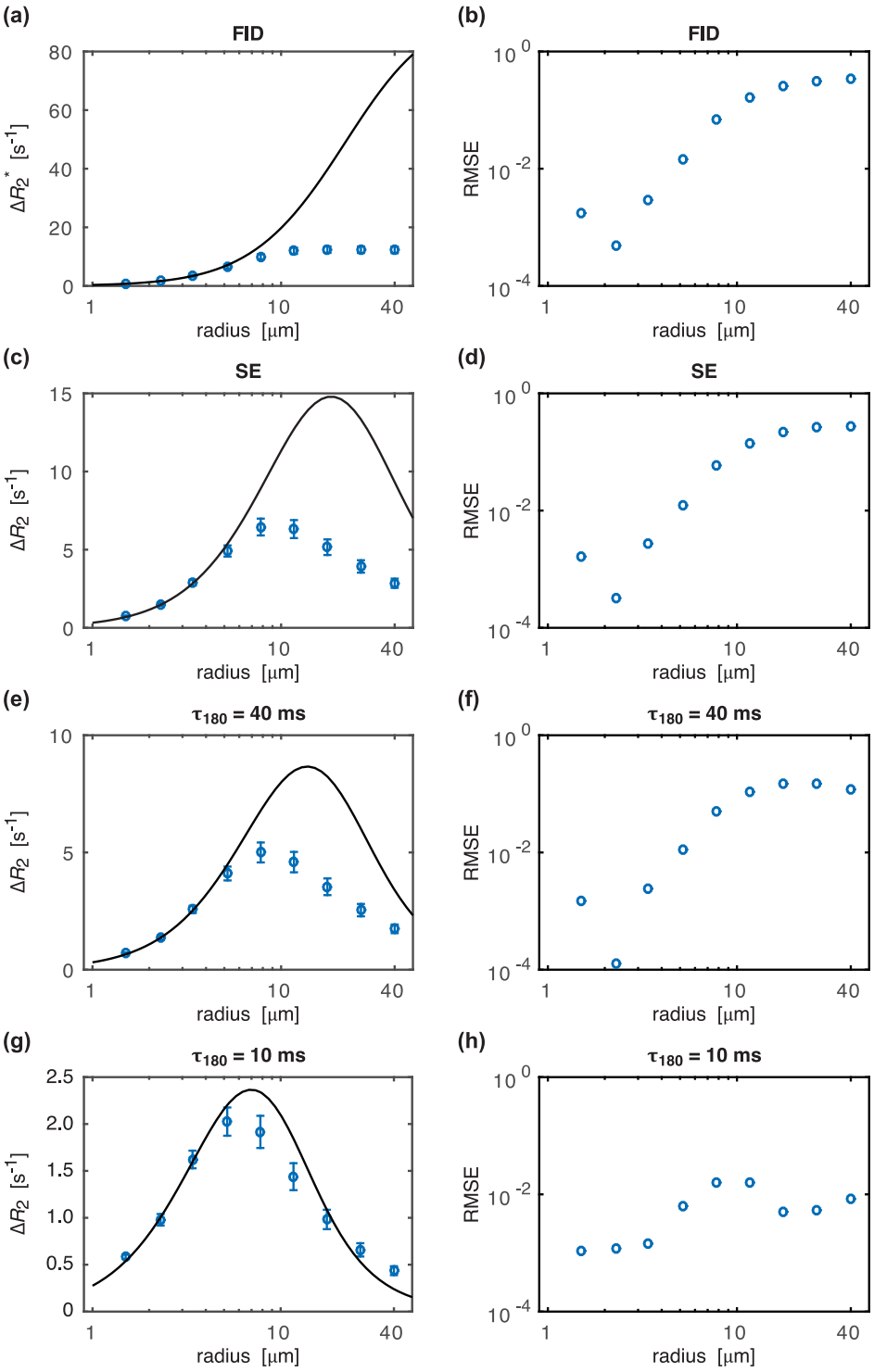
(a)
FID
ΔR2* [s-1]
radius [μm]
(b)
FID
RMSE
radius [μm]
(c)
SE
ΔR2 [s-1]
radius [μm]
(d)
SE
RMSE
radius [μm]
(e)
τ180 = 40 ms
ΔR2 [s-1]
radius [μm]
(f)
τ180 = 40 ms
RMSE
radius [μm]
(g)
τ180 = 10 ms
ΔR2 [s-1]
radius [μm]
(h)
τ180 = 10 ms
RMSE
radius [μm]

Figure 5.4: Accuracy of the CFS vs. simulations across a range of radii and pulse sequences.

Page 83: (Left) Comparison of $\Delta R_2^{(*)}$ from the simulations (circle markers) with the predicted values from the CFS (black line). The error bars represent the standard deviation of the mean simulated values. (Right) The RMSE across time between the mean simulations and the CFS. Note that the ΔR_2 scales change between the pulse sequences' figures, whereas they are constant for the RMSEs. Each row is from a different pulse sequence. RMSE = root mean square error.

the volume fraction was set to 3% and $\Delta\chi$ corresponded to an SO_2 of 60%. Here, those simulations were repeated with ζ up to 60%, encompassing typical hematocrits, and SO_2 up to 90%.

Figure 5.5a–c show the average radial correlation functions for the simulated three sphere distributions at $\zeta = 40\%$ along with the fits to Eq. (5.4). None of the distributions exactly show the Gaussian decay described by Eq. (5.4), including the overlapping distribution. However, as shown in Figure 5.5d, the $G(r = 0)$ values (i.e., the mean square field offsets, G_0) increase linearly with volume fraction for the overlapping networks according to Eq. (5.12) and they vary quadratically according to $\zeta(1 - \zeta)$ for both non-overlapping distributions, in agreement with earlier predictions [75,79]. From the fits of Eq. (5.4) to $G(r)$, the fitted r_c are in excellent agreement with Eq. (5.11) and are independent of volume fraction for overlapping spheres (Figure 5.5e). For the non-overlapping networks, however, the fitted r_c decreases with increasing volume fraction by an amount that depends on the exact distribution of the spheres. Since $G(r)$ was not exactly Gaussian and since the G_0 values were in such good agreement with theory, all fits to $G(r)$ were constrained to pass through G_0 at $r = 0$.

Example simulated and predicted time series using the CFS are given in Figure 5.6a–c, the effective ΔR_2 for all ζ are given in Figure 5.7a–c, and the RMSE between the simulations and CFS are given in Figure 5.7d–f. In the overlapping networks, the maximum RMSE is 0.016 for all ζ

and SO_2. Given that the signals range from 1 (at t = 0) to 0, those magnitudes of RMSE are negligibly small. In the random non-overlapping distribution, the largest RMSE is 0.024 and it occurs at ζ = 30%, as shown in Figure 5.6e, where one could argue that that degree of error is still relatively negligible. In the HCP distribution, the RMSE steadily increases for ζ > 20% up to 0.06 at ζ = 60%, where it appears more substantial (Figure 5.7e).

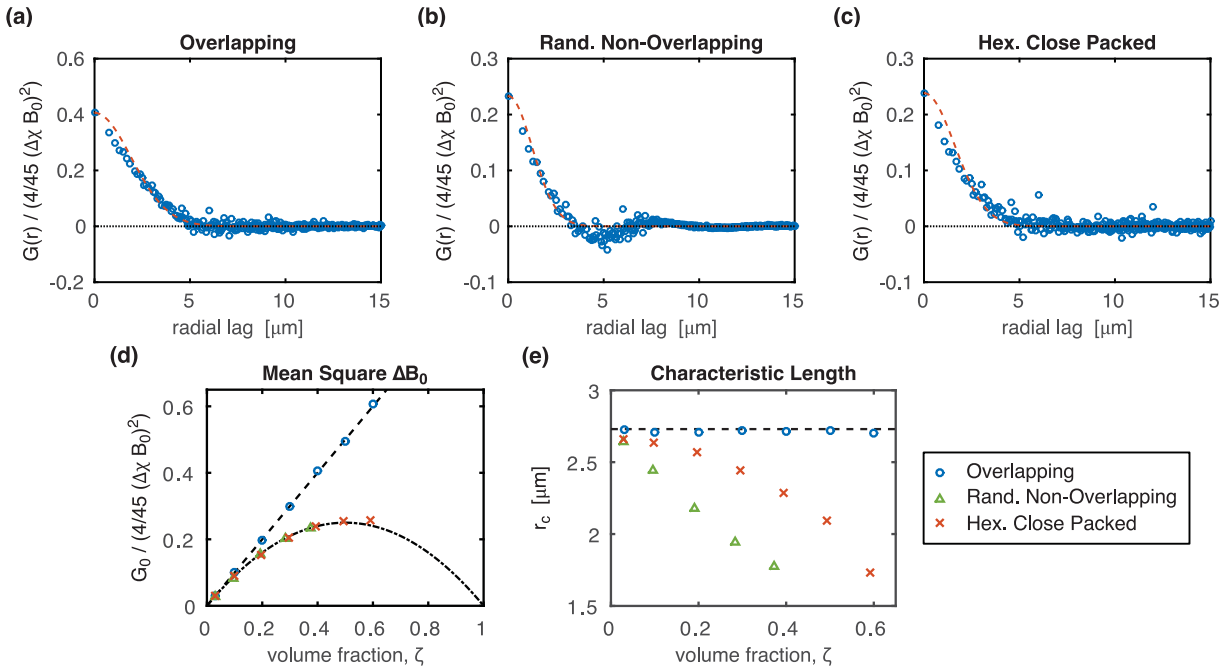

Figure 5.5: Radial correlation functions, G_0, and r_c.

(a–c) Mean radial correlation functions from the three sphere distributions at a volume fraction of 40% (circle markers) along with their fits to the Gaussian decay in Eq. (5.4) (dashed line). These have been normalized such that their values at r = 0 are proportional to ζ or $\zeta(1 - \zeta)$ for the non-overlapping networks. (d) The mean square field inhomogeneity values, G_0, from the three different sphere distributions as a function of volume fraction. These have also been normalized. The dashed line and the dash-dotted line show the cases where G_0 is proportional ζ or $\zeta(1 - \zeta)$, respectively. (e) The characteristic length parameter, r_c, obtained from the fits to the simulation networks' radial correlation functions as a function of volume fraction. These r_c values are compared to the value predicted from Eq. (5.11), which for a radius of 3 μm gives r_c = 2.73 μm (dashed black line). (d) and (e) share the legend on the bottom right. Note that the random non-overlapping networks could generally only be populated up to a volume fraction of ~40%.

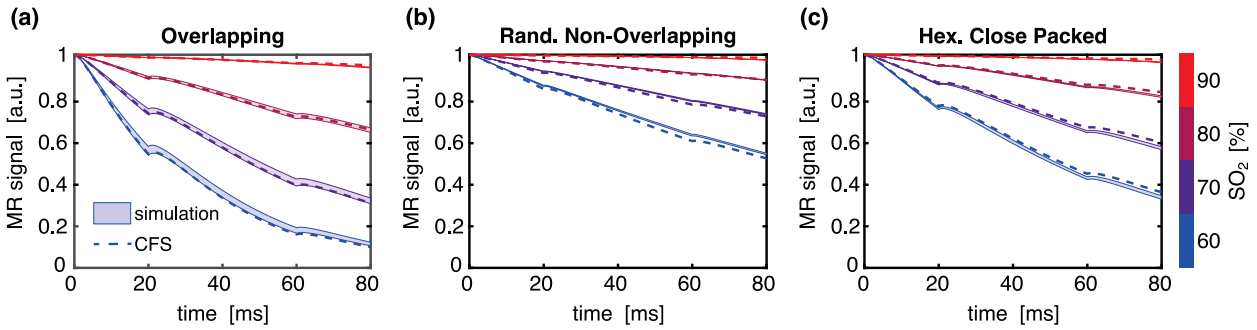

Figure 5.6: Simulated signals vs. the CFS for three sphere distributions.

In all three simulations, $\zeta = 40\%$, $\tau_{180} = 40$ ms, and the distributions are: (a) overlapping, (b) random non-overlapping, and (c) hexagonal close packed. The shaded bands represent the mean ± standard deviation of the simulated signals and the dashed lines represent the CFS for each SO_2 as predicted using the fitted G_0 and r_c values from the networks' radial correlation functions. The plotted colours correspond to the SO_2 values in the colour bar on the right.

Independent of the exact agreement between the CFS and simulations, it is apparent from Figure 5.6 and Figure 5.7 that the amount of decay is significantly reduced in the non-overlapping networks. This is expected given that G_0 for both was decreased by a factor $(1 - \zeta)$ relative to the overlapping distribution. However, between the two non-overlapping distributions, the decay in the random non-overlapping distribution is significantly reduced relative to the HCP distribution. Additionally, the degree of refocusing in the random non-overlapping distribution is decreased and the time to maximum refocusing is shifted earlier in time. Both observations are explained by the decreased r_c. The impact of the decreasing r_c can also be seen in Figure 5.7b–c, where the non-monotonic changes in ΔR_2 cannot be explained by a quadratic dependence on ζ alone. If that were the case, ΔR_2 should peak at $\zeta = 50\%$, whereas in the random non-overlapping distribution it peaks at $\zeta \approx 30\%$ and in the HCP distribution it peaks at $\zeta \approx 40\%$.

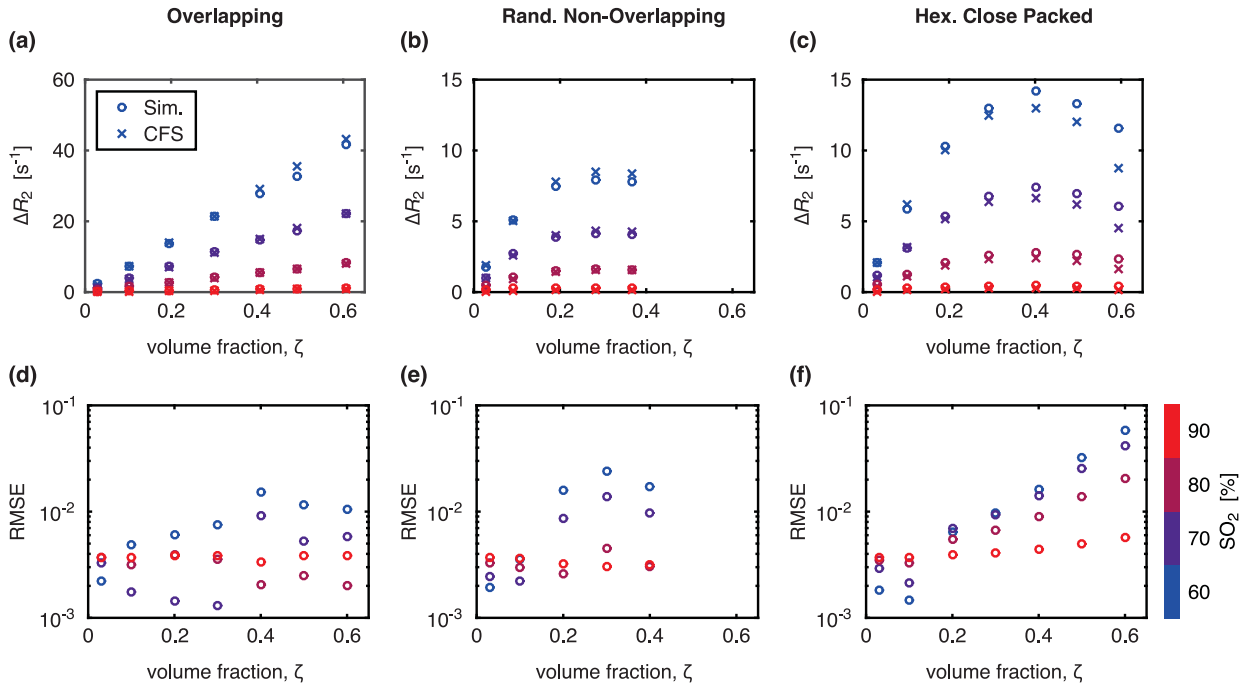

Figure 5.7: Accuracy of the CFS across all volume fractions.

Accuracy of the CFS for the three different sphere distributions as assessed using ΔR_2 (a–c) and the RMSE (d–f). Mean simulated ΔR_2 are represented by the circle symbols and the CFS-predicted ΔR_2 are represented by the x's. The sphere distributions are overlapping (a and d), random non-overlapping (b and e), and hexagonal close packed (c and f). The symbol colours correspond to the SO_2 values in the colour bar on the bottom right. Note that the ΔR_2 scale in (a) is four times those of (b) and (c).

5.7 Discussion

In this study, we have used the weak field approximation model to describe the entire transverse signal time course. We found that the closed-form solution and the original WFA expression for monoexponential decay provide very similar estimates for ΔR_2 in CPMG sequences; however, the discrepancy for the measured FID decay can be significant (up to as much as 100% error in the estimates of ΔR_2^*). In light of the agreement between the simulations and the CFS in the motional narrowing regime, as detailed in Figure 5.4, we would attribute this discrepancy to the ΔR_2^* model

not accurately accounting for the amount of time required for the FID to approach monoexponential decay. Considering that most multi-echo gradient echo sequences use echo spacings less than 20 ms, the discrepancy could be substantial if one were to use measured ΔR_2^* values to obtain quantitative estimates of the underlying tissue properties.

To determine the dephasing regime in which the CFS was valid, we compared it with simulations in which the sphere radii were increased from 1.5 μm up to 40 μm (Figure 5.3). These simulations used a low volume fraction of 3% such that the issue of perturber overlap would be negligible. In most of the pulse sequences, the CFS started to significantly overestimate the decay for $R > 5.2$ μm but was accurate for smaller radii. The motional narrowing regime is most commonly classified using the dimensionless inequality $\alpha = \tau_D \delta\omega \ll 1$ [60]. With our simulation parameters, a radius of 5.2 μm results in $\alpha = 2.7$, meaning that the WFA is valid in the motional narrowing regime, as expected, and it can be applied across the motional narrowing-intermediate dephasing regime boundary but not well beyond it. The simulations in this study used a diffusion coefficient of 2.7 $\mu m^2/ms$, corresponding to that of free water in plasma [137]. This should be an accurate representation of the diffusion coefficient at low perturber concentrations, however, as the perturber concentration increases, the apparent diffusion coefficient will decrease as the diffusion will be hindered by the finite permeability of the perturbers. For blood, the apparent diffusion coefficient may be in the range of 1.5–2.1 $\mu m^2/ms$ [137,140]. With RBCs modelled as 3.0-μm spheres, this would result in a maximum α of 1.6, meaning that the WFA can still accurately describe the relaxation from RBCs when using a decreased diffusion coefficient.

When we performed simulations that more closely resembled RBCs using a range of SO_2 values and increased volume fractions, the CFS was in excellent agreement with the WFA. This was in spite of the fact that the radial correlation functions of the simulation networks did not

always show the Gaussian decay proposed by Jensen and Chandra [76] (Figure 5.5). The overall shape of $G(r)$ was similar for the overlapping and the HCP distributions and tended to be monotonically decreasing. $G(r)$ for the random non-overlapping distribution, however, was non-monotonic and it displayed oscillations about $G(r) = 0$. Whatever discrepancies that do exist between the simulated signals and the CFS could perhaps be reduced by modifying the expression for $G(r)$ to better reflect the empirical values depending on the exact perturber distribution. Novikov and Kiselev [141] have considered this where they derived a sinc-based radial correlation function and found reasonable agreement with simulations in the motional narrowing regime. Judging from Figure 5.5, a sinc-based radial correlation function may better describe $G(r)$ for the randomly non-overlapping distribution but likely not for the HCP distribution, therefore the modification will still need to be perturber distribution-dependent.

This study also provides further validation that the true volume fraction, ζ, must be replaced with a scaled version, $\zeta' = \zeta(1 - \zeta)$, when considering systems with relatively high volume fractions [79]. Kiselev and Novikov [79] have justified this scaling both formally as the second order density correction from the virial expansion as well as qualitatively, where the roles of "perturber" and "external medium" become reversed as ζ increases. This scaling applies to the mean square field inhomogeneity, G_0, and is extremely important given that the effective decay rates are generally considered to be linearly proportional to G_0, as in Eq. (5.6). In addition to this, we have shown that the decay rates are further reduced by changes in the characteristic length, r_c, as ζ increases. By ignoring terms lower than 1^{st}-order in t in Eq. (5.10), it can be shown that the asymptotic dependence of the relaxation rate on r_c is quadratic. Therefore, the signal relaxation becomes quite sensitive to any changes in r_c. This is apparent in the large difference in the relaxation rates between the two non-overlapping distributions, which is nearly a factor of two at $\zeta = 40\%$.

To the best of our knowledge, this relationship between r_c and the volume fraction has only been briefly discussed in the literature but it has not been thoroughly investigated [139]. To make predictions of the transverse signal with the CFS for the non-overlapping distributions, we were required to fit Eq. (5.4) to the empirically determined radial correlation functions from the simulation networks themselves. It would be convenient if the simulation networks did not need to be created at all. An improved understanding of the statistical properties of the perturber distributions, in a manner similar to what has been done with time-dependent diffusion studies [142] may enable this.

One limitation of this study is that the validation of the CFS was only performed using spherical perturbers. This was done since there exist analytical solutions for G_0 and r_c that allowed for the simulations to be predicted *a priori*. However, by increasing the volume fraction without overlap, the field distributions became less like those from spheres with uncorrelated positions. In this case, the CFS was still able to accurately capture the signal evolution. For other geometries, the parameters G_0 and r_c would take on other values but they would scale with volume fraction and field offset strength similarly. Using the Gaussian phase approximation in the long-time limit (which shows the same long-time behaviour as the WFA), Sukstanskii and Yablonskiy [131] calculated ΔR_2 for randomly oriented ellipsoids of revolution. Even for the case of an oblate spheroid where one radius is twice the length of the other – a geometry that has previously been used to represent RBCs [140] – ΔR_2 would still be within 4% of that of spheres (when the sphere and ellipsoid volumes and volume fractions are matched). This reflects how the field inhomogeneities can be approximated as those from a sphere in the long-time limit [143]. In the short-time limit, both FID and SE relaxation depend on the ratio of the surface area to the volume [131]. This ratio for an oblate spheroid is approximately 2/3 of a sphere's, so a sphere does not

reliably reproduce the initial time course. Therefore, particularly in the long-time limit, fits to the CFS for spheroids might still be cautiously interpreted as if they were spheres.

Another limitation of both the theory and the simulations includes the assumption that the water diffusion inside, outside, and across the perturbers is equal. For very small perturbers or for small volume fractions, such as iron depositions, this is likely not significant. For RBCs, the cellular permeability to water is finite and the lifetime between exchanges of a water molecule across the cell is approximately 10 ms [45,132,144]. Water is, therefore, quickly exchanging across the RBC boundary, and, as discussed above, this may be suitably modelled with a single diffusion coefficient that is the weighted sum of the intra- and extra-cellular diffusion coefficients [74]. The WFA has successfully been applied to relaxometry data from a range of tissues in vivo, such as blood samples [76,78,80-82] and tissue iron [76], where the parameters G_0 and r_c have different interpretations but are still related to the mean square field inhomogeneity and perturber size. This too is evidence that these limitations have only a minimal effect on the WFA's ability to characterize relaxation from tissues in the motional narrowing regime and to provide fitted parameters of physiological interest.

We envision the CFS could be used to simplify the simulation of transverse signal decay from systems in the motional narrowing regime, such as blood, where the sheer number of perturbers makes simulation a computational burden. This could be achieved by directly substituting the simulation time course with the CFS analytical time course, provided appropriate values for G_0 and r_c. As shown with the spheres at high volume fractions, when analytical solutions for G_0 and r_c are not apparent, these parameters could be empirically determined by fitting the radial correlation function. Another application of the CFS could be to decrease the total scan time required for fitting transverse signal decay to the WFA by substituting the large number of

refocusing rates used during a CPMG experiment with fewer refocusing rates and sampling the signal at time points away from the spin echo times. The non-SE samples would provide additional information, related to the characteristic perturber size, that could then be fit using the CFS. It may even be feasible to reduce the number of acquisitions to one with many GE readouts.

5.8 Conclusion

We have derived and validated a closed-form solution for transverse signal decay under an arbitrary number of refocusing pulses using the weak field approximation. When using the signal at the spin echoes from the CFS to fit for ΔR_2, it was in excellent agreement with a well-known expression for asymptotic ΔR_2 derived in the original WFA study [76], showing self-consistency of the CFS within the WFA. This comparison also showed that the time for an FID to approach monoexponential decay can be substantial and, thus, caution should be taken if applying the asymptotic model of ΔR_2^* decay to gradient echo data.

When compared against simulations from spherical perturbers, the CFS was found to be very accurate in the motional narrowing regime – as expected – and partially into the intermediate dephasing regime. This was the case when the volume fraction varied from 3%–60% and the perturbers could overlap. When the perturbers could not overlap, the relaxation rates of the simulations were significantly reduced relative to the overlapping case. In the context of the weak field approximation, these reductions in ΔR_2 could be explained by reductions in the mean square field inhomogeneity, G_0, which was proportional to $\zeta(1 - \zeta)$ and independent of the perturber distribution as well as reductions of the characteristic length, r_c, which were dependent on both ζ and the perturber distribution. These changes in G_0 and r_c could both be empirically determined

by fitting the radial correlation functions of the simulation networks, resulting in excellent agreement between the CFS and simulations up to $\zeta \approx 40\%$.

This study has advanced biophysical signal modelling from tissues where the perturber volume fraction is substantial. This could help simplify simulations from tissues such as blood or reduce the amount of time required for quantitative *in vivo* or *ex vivo* MR acquisitions from systems in the motional narrowing regime.

5.9 Acknowledgements

The authors would like to recognize financial support from the Canadian Institutes of Health Research (FDN 143290) and the Campus Alberta Innovates Program. The simulations in this study were enabled in part by support provided by WestGrid (www.westgrid.ca) and Compute Canada Calcul Canada (www.computecanada.ca).

Chapter 6

Gas-Free Calibrated fMRI

6.1 Preface

As discussed in Section 2.2.3, the first gas-free fMRI calibration experiments employed multi-echo gradient echo and spin echo sequences and combined the data to quantify R_2' [24,25]. However, these multi-echo estimates of R_2' are known to be highly sequence-dependent [145], as they will be impacted by multi-exponential decay [25,146], spin echo refocusing rate [75,147], and, similarly, diffusion-induced loss of phase history for single echo spin echo sequences [27]. Blockley et al. [27] proposed a gas-free calibration technique based on the ratio of spin echo and asymmetric spin echo images that overcomes multi-exponential decay issues yet is still affected by the diffusion-induced spin echo attenuation.

This chapter presents a study whose aim was to develop an asymmetric spin echo-based calibration method that would be accurate, insensitive to multi-exponential decay, and could correct for diffusion-induced spin echo attenuation. Ideally, this could have been guided by

analytical signal modelling, however, most signal models can only accurately predict signal from vessel networks over a limited domain of vessel sizes [148]. As signal decay is known to span all three dephasing regimes (motional narrowing, intermediate, and static dephasing) due to the range of vessel sizes present in the brain, this study was instead guided by signal simulations from blood vessel networks, as described in Chapter 3, using a blood susceptibility calculation, as described in Chapter 4. Based off the simulation results, a correction scheme for the spin echo attenuation was proposed and validated using additional simulations and in vivo experiments in healthy subjects. The principal advance of the proposed correction scheme is that, with the acquisition of at least one more pair of spin echo and asymmetric echo images, the correction can be derived from the data itself, rather than applying an assumed scaling factor as previously suggested [27]. This chapter is based on a manuscript submitted to *NeuroImage*. Supplementary results pertaining to the measurement of signal dephasing from macroscopic field inhomogeneities are provided in Appendix A. Ethics approval of this study is provided in Appendix B.

Gas-Free Calibrated fMRI: Correcting for Diffusion

Avery J.L. Berman[1,2], Erin L. Mazerolle[2,3], M. Ethan MacDonald[2,3], Nicholas P. Blockley[4], Wen-Ming Luh[5], G. Bruce Pike[1,2,3,6]

[1]Department of Biomedical Engineering, McGill University, Montreal, Canada

[2]Hotchkiss Brain Institute, University of Calgary, Calgary, Alberta, Canada

[3]Department of Radiology, University of Calgary, Calgary, Alberta, Canada

[4]FMRIB Centre, Nuffield Department of Clinical Neurosciences, University of Oxford, Oxford, United Kingdom

[5]Cornell MRI Facility, Cornell University, Ithaca, NY, USA

[6]Department of Clinical Neuroscience, University of Calgary, Calgary, AB, Canada

Submitted to NeuroImage

6.2 Abstract

Calibrated functional magnetic resonance imaging (fMRI) is a method to measure the metabolic and hemodynamic contributions to the blood oxygenation level dependent (BOLD) signal. This technique typically requires the use of a respiratory challenge, such as hypercapnia or hyperoxia, to estimate the calibration constant, *M*. There has been a recent push to eliminate the gas challenge from the calibration procedure using asymmetric spin echo (ASE) based techniques. This study uses simulations to better understand spin echo (SE) and ASE signals, analytical modelling to characterize the signal evolution, and in vivo imaging to validate the modelling. Using simulations, it is shown how ASE imaging generally underestimates *M* and how this depends on several parameters of the acquisition, including echo time and ASE offset, as well as the vessel size. This underestimation is the result of imperfect SE refocusing due to diffusion of water through the extravascular environment surrounding the microvasculature. By empirically characterizing this SE attenuation as an exponential decay that increases with echo time, we have proposed a quadratic ASE biophysical signal model. This model allows for the characterization and compensation of the SE attenuation if SE and ASE signals are acquired at multiple echo times. This was tested in healthy subjects and was found to significantly increase the estimates of *M* across grey matter. These findings show promise for improved gas-free calibration and can be extended to other relaxation-based imaging studies of brain physiology.

Keywords

calibrated fMRI; BOLD; asymmetric spin echo; relaxometry; diffusion; cerebral metabolic rate of oxygen

6.3 Introduction

Calibrated functional magnetic resonance imaging (fMRI) was developed to disentangle the hemodynamic and metabolic contributions to the blood oxygenation level dependent (BOLD) signal using simultaneous measurements of the gradient echo BOLD signal and cerebral blood flow (CBF) [14,15]. A calibration experiment is run to estimate the calibration constant, M, and is most commonly performed using a respiratory challenge where subjects inhale a gas mixture with additional carbon dioxide and/or oxygen to elicit changes in the BOLD signal and CBF or arterial oxygen tension [15,21,36,68]. The use of hypercapnia, the state of elevated CO_2 in blood, suffers from multiple limitations: it may violate the assumption of iso-metabolism on which standard calibration models depend [149-152], and it typically measures perfusion changes using time-resolved arterial spin labelling (ASL), an imaging technique with a low signal-to-noise ratio. Similarly, the use of hyperoxia, the state of elevated O_2 in blood, requires either the additional measurement of the oxygen extraction fraction and the concentration of hemoglobin in blood or the assumption of those two parameters [21,22] that can lead to bias [26]. Hyperoxia may also produce concomitant decreases in CBF if blood CO_2 is not controlled [153,154]. In general, gas challenges require additional apparatus and increased subject tolerance and preparation, thus, a gas-free alternative would greatly improve the appeal of calibrated fMRI.

To date, a limited number of studies have examined gas-free calibration of the BOLD signal by substituting the gas challenge with a measurement of R_2' at rest, the reversible component of the transverse relaxation rate [24,25,27,28]. Under the assumption that the primary difference between the apparent and the irreversible relaxation rates (R_2^* and R_2, respectively) in a voxel is from the field inhomogeneities generated by deoxyhemoglobin (deoxyHb) [25,26], R_2' is the

favoured candidate for gas-free calibration due to its intimate relationship with baseline blood oxygen saturation and the deoxygenated cerebral blood volume (CBV) [5]. However, as in most areas of MR relaxometry, the apparent values of R_2' are highly dependent on the measurement technique and may produce different values due to multi-exponential decay, imperfect spin echo refocusing, and other acquisition related factors [145]. Blockley et al. [27] recently proposed a calibration technique that is insensitive to multi-exponential decay based on using spin echo (SE) and asymmetric spin echo (ASE) imaging. When compared against traditional hypercapnic calibration, their ASE calibration underestimated M across grey matter (GM) and the visual cortex, on average. This underestimation was postulated to arise from incomplete spin echo refocusing of spins diffusing in the extravascular space. This effect is the same source of contrast in SE BOLD imaging, and is known to be vessel-size and field strength dependent [17].

In addition to imperfect SE refocusing, several other sources may confound the observed R_2' values. Macroscopic field inhomogeneities, which are prominent around air-tissue interfaces, lead to dramatic geometric distortions and signal intensity distortions in echo planar imaging (EPI). The intensity distortions tend to increase R_2' and these effects can be mitigated by a range of acquisition-related methods [155]. Cerebrospinal fluid (CSF) has recently been shown to significantly increase measured R_2' in grey matter [156,157]. This is postulated to arise from a chemical shift between CSF and parenchyma, resulting in enhanced signal dephasing in tissue voxels with partial voluming with CSF [158]. By adding a fluid attenuated inversion recovery (FLAIR) preparation to the imaging sequence, the CSF signal can be eliminated and the R_2' of neighbouring parenchymal voxels tends to decrease. Unlike field inhomogeneities and CSF, which can be prospectively and retrospectively managed, additional non-deoxyHb sources of tissue magnetic susceptibility, such as iron depositions and myelin, will alter R_2' in a less predictable

manner (they can increase or decrease R_2', depending on their susceptibility and relative concentration). Kida et al. [24] found that these other sources of susceptibility have negligible contributions to the observed R_2 and R_2^* (and hence R_2') at 7 T in rats. In this study, which was performed at a field strength of 3 T, we do not consider these other sources, consistent with earlier work [27,146].

The purpose of this study was to determine how incomplete refocusing of SE and ASE signals affects the estimation of R_2' and how it can be accounted for to obtain a more accurate estimate of M. Simulations were used to determine the vessel-size dependence of the R_2' underestimation and to develop a strategy to retrospectively correct for it. This strategy was tested in vivo, taking precautions to avoid confounds from macroscopic field inhomogeneities and CSF partial volume. These ASE-based M calculations were compared against hypercapnic calibration in the same subjects.

6.4 Theory

6.4.1 Calibrated fMRI with Asymmetric Spin Echo Imaging

The standard calibrated fMRI model that relates changes in $CMRO_2$ and CBF to changes in the gradient echo (GE) BOLD signal is [15]

$$\frac{\Delta \mathrm{BOLD}}{\mathrm{BOLD}_0} = M\left(1 - \left(\frac{\mathrm{CBF}}{\mathrm{CBF}_0}\right)^{\alpha-\beta}\left(\frac{\mathrm{CMRO}_2}{\mathrm{CMRO}_{2|0}}\right)^{\beta}\right), \qquad (6.1)$$

where the subscript '0' refers to a value at baseline and $\Delta\text{BOLD} = \text{BOLD} - \text{BOLD}_0$. α is the Grubb constant and accounts for coupling between CBV and CBF arising from an empirical power law relation between the two [66]. β describes the non-linear dependence of the change in R_2^* on the susceptibility offset of blood relative to tissue [17,64]. M is proportional to the resting concentration of deoxyHb in blood and it can be considered the maximum fractional increase in the GE BOLD signal, which would theoretically occur upon removal of all deoxyHb in blood (i.e., venous oxygen saturation $\rightarrow$ 100%) [14,159,160]. Under the assumption of iso-metabolism, M is estimated with hypercapnia (M_{HC}) by measuring changes in CBF and the BOLD signal using

$$M_{\text{HC}} = \frac{\frac{\Delta\text{BOLD}}{\text{BOLD}_0}}{1 - \left(\frac{\text{CBF}}{\text{CBF}_0}\right)^{\alpha-\beta}}. \tag{6.2}$$

Rather than perturb the oxygen saturation (SO_2) like a gas-based calibration would, a spin echo image perturbs the spins of the system such that, *in the absence of diffusion*, the SE will refocus all the spin dephasing induced by deoxyHb present in blood vessels and will, therefore, be equal to the maximum possible GE BOLD signal. To then estimate R_2', one can acquire another image with R_2^*-weighting, since $R_2^* = R_2 + R_2'$. Acquiring an ASE image is appropriate for this because it will have the same slice profile as the SE image. Example SE and ASE sequences and their transverse signal decays are displayed in Figure 6.1. If the spin echo in the ASE image is shifted earlier by a time τ, the signal can be described by

$$S_{\text{ASE}}(\text{TE}, \tau) = S_0 \text{e}^{-R_2 \cdot \text{TE}} \text{e}^{-R_2' \tau}, \tag{6.3}$$

where TE is the echo time, τ is the ASE offset, and S_0 is the signal at TE = 0. In the convention used here, τ > 0 corresponds to TE occurring a time τ *after* the SE occurs. Eq. (6.3) assumes τ > 0 but in the case of τ < 0, τ should to be replaced by |τ|. The SE signal, S_{SE}, is also described by Eq. (6.3) but with τ = 0. If τ is chosen to be the same as the echo time used for functional imaging, then M from ASE imaging (M_{ASE}) can be estimated from the ratio of an SE and ASE image, both acquired at time TE [27]:

$$\begin{aligned} M_{ASE} &= \ln(S_{SE}/S_{ASE}) \\ &= R_2'\tau. \end{aligned} \tag{6.4}$$

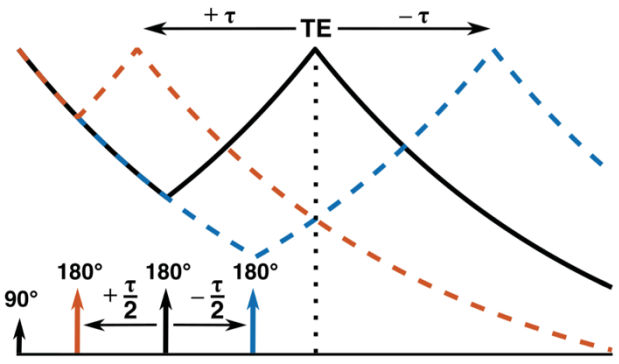

Figure 6.1: Example asymmetric spin echo sequences and transverse decay.

The SE and ASE pulse sequences share the same 90° excitation pulse and sample the signal at the same echo time (TE, dotted vertical line). The black curve represents the pure SE sequence signal decay. The dashed orange curve represents the ASE sequence signal decay when the ASE offset is +τ. The dashed blue curve represents the ASE sequence signal decay when the ASE offset is –τ. The three signals have no T_2 decay, no diffusion effects, and only show R_2'-related decay and refocusing. The two ASE signals are equal at TE.

6.4.2 Quadratic Spin Echo Attenuation

The model of gas-free calibration described above by Eq. (6.4) applies in the absence of diffusion, where the 180° pulse will perfectly refocus the dephasing surrounding blood vessels. To determine how SE attenuation from diffusion depends on TE and τ, simulations of the SE and ASE signals were run from vessel networks as a function of vessel radius. These considered the decay resulting from field inhomogeneities only and ignored intrinsic T_2 decay (details provided in the Methods section below). Figure 6.2 shows examples of the simulations for three different vessel radii as a function of TE. The grey curves show the entire simulated time series, like the simulated signals in Figure 6.1, however, diffusion is incorporated and there are more spin echo times displayed. The impact of diffusion on the individual simulated time series is that the amount of SE attenuation increases with increasing TE and the time at which maximum refocusing occurs shifts earlier in time than the nominal SE time. Also, the amount of decay and refocusing both increase with increasing vessel size. The coloured envelopes represent the signals at the echo times, i.e., when the decays are actually sampled, be it the SE or ASE signals. The signal envelopes for all radii and for more values of τ are shown in Figure 6.3. The key qualitative observations are:

1. With respect to TE, the envelopes are all well described by a quadratic-exponential decay early on and by linear-exponential decay later, with the time to transition being proportional to vessel radius.
2. With respect to τ, the envelope for a given radius is approximately a shifted copy of that radius' envelope from τ = 0. The shift is by an amount τ in time and an amount $R_2'\tau$ along the ordinate. R_2' is smallest for small vessels [17], hence the shift is smaller for them and greater for large vessels.

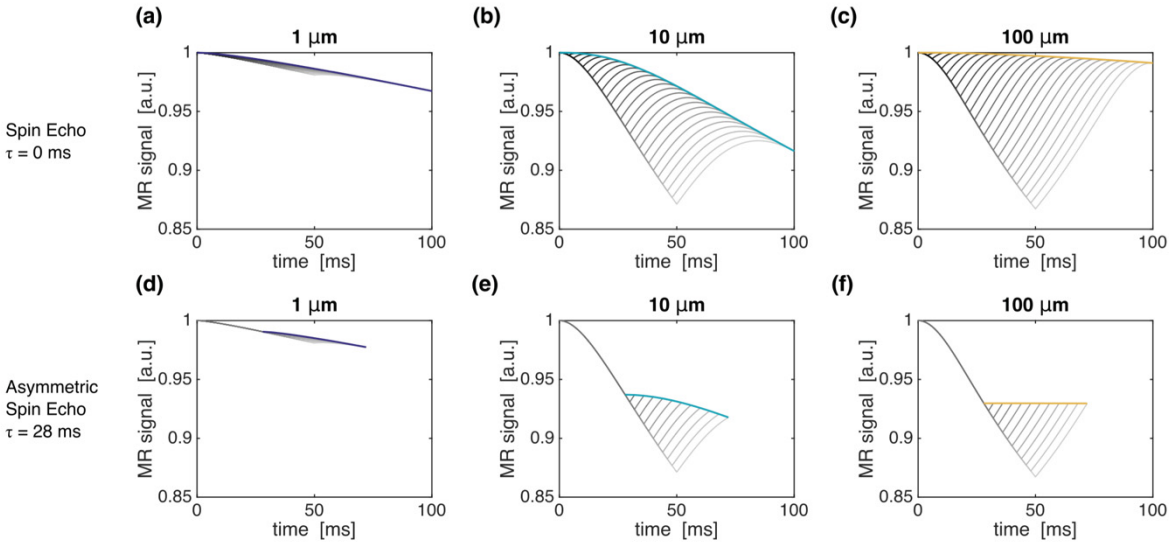

Figure 6.2: Example simulated time series from SE and ASE sequences.

The individual time series for each TE are shown by the greyscale curves, with black to grey representing earlier to later TEs and TE incrementing by 4 ms. The coloured signal envelopes represent the signals at the echo times. In the case of the SE simulations (top row), each envelope shows only the signal at the SE times (t_{SE}). In the case of the ASE simulations (bottom row), each envelope shows only the signals at the times TE = t_{SE} + τ. The maximum t_{SE} simulated was 100 ms, therefore, TE ranges from 28 ms to 72 ms for the ASE envelope. Each column depicts the simulations from a network containing a different vessel radius (1 μm, 10 μm, or 100 μm). The plotted greyscale ASE signals are for a negative ASE offset but the resulting differences between their signal envelopes and the signal envelopes from the positive offsets were negligible.

The simulations above were repeated on networks populated by two different distributions of vessel radii, referred to here as the Lauwers [46] and Frechet distributions [49], and shown in Figure 6.4. The Lauwers distribution had very few radii > 10 μm, whereas the Frechet distribution peaked near 10 μm and had a long tail out to 60 μm. Similar signal behaviour can be seen in the simulations from the Lauwers and Frechet vessel-size distributions, shown in Figure 6.5. In this case, the Lauwers distribution, which is primarily microvascular, appears to transition from quadratic- to linear-exponential decay earlier than the Frechet distribution and its vertical shift is smaller,

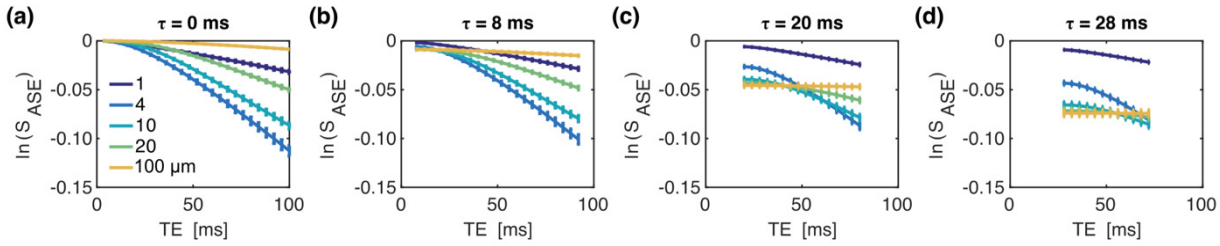

Figure 6.3: Logarithm of the ASE signal envelopes as a function of TE and vessel radius.

Each sub-figure shows the envelope for different ASE offsets, τ, where $\tau = 0$ corresponds to the pure spin echo signal. Within each sub-figure, each curve represents the mean signal from a different vessel radius, and they all share the legend in (a). The ranges of TE for each sub-figure are $\tau \leq TE \leq 100\ ms - \tau$. Error bars represent the mean ± standard deviation (SD) of the simulations across networks.

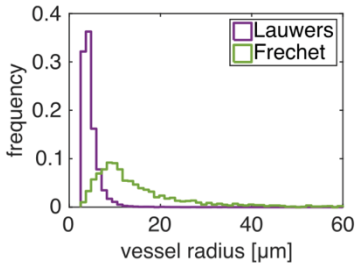

Figure 6.4: Histograms of the Lauwers and Frechet vessel-size distributions.

The values represent the frequency with which the given ranges of radii occur across all vessel networks of a given distribution.

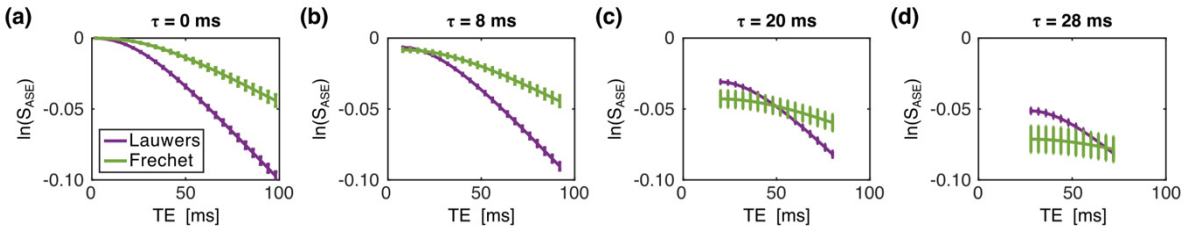

Figure 6.5: Logarithm of the ASE signal envelopes as a function of TE for the Lauwers and Frechet vessel-size distributions.

Each sub-figure shows the envelope for different ASE offsets, τ, where τ = 0 corresponds to the pure spin echo signal. All sub-figures share the legend in (a). Error bars represent the mean ± SD of the simulations across networks.

consistent with the results in Figure 6.3.

We propose that the diffusion-induced SE attenuation can be characterized by ignoring the transition to linear-exponential decay and considering the attenuation as an additional quadratic-exponential decay term with rate constant $(R_{2,diff})^2$. This decay would commence at TE = τ and the ASE signal in Eq. (6.3) would be modified as

$$S_{\mathrm{ASE}}(\mathrm{TE},\tau) = S_0 e^{-R_2\cdot \mathrm{TE}} e^{-R_2'\cdot\tau} e^{-\left(R_{2,diff}\right)^2(\mathrm{TE}-\tau)^2}. \tag{6.5}$$

We refer to this model of the ASE signal as the *quadratic ASE (q-ASE) model*. The $(R_{2,diff})^2$ term can be visualized by plotting the expression

$$\begin{aligned}\Delta R_2(\mathrm{TE}) &= -\frac{\ln S_{\mathrm{SE}}}{\mathrm{TE}} = -\frac{\ln\left(S_{ASE}(\tau=0)\right)}{\mathrm{TE}} \\ &= -\ln S_0\,/\mathrm{TE} + R_2 + \left(R_{2,diff}\right)^2\mathrm{TE} \\ &= \left(R_{2,diff}\right)^2\mathrm{TE}.\end{aligned} \tag{6.6}$$

The final equality is a simplification for the simulations only because S_0 is normalized to 1 and the intrinsic R_2 is set to 0. This indicates that $(R_{2,diff})^2$ can be estimated from the initial slope of ΔR_2 vs. TE.

Taking the ratio $\ln(S_{SE}/S_{ASE})$ using Eq. (6.5) gives

$$\ln\left(\frac{S_{SE}}{S_{ASE}}\right) = \ln\left(\frac{S_{ASE}(\tau = 0)}{S_{ASE}(\tau)}\right) = R_2'\tau + \left(R_{2,diff}\right)^2\tau^2 - 2\left(R_{2,diff}\right)^2\tau\mathrm{TE}. \quad (6.7)$$

Since $\tau \leq \mathrm{TE}$, the ratio will always be less than $R_2'\tau$ and is consistent with M being underestimated from $\ln(S_{SE}/S_{ASE})$ alone, as in Eq. (6.4). From the linear TE-dependence, it should be possible to estimate $(R_{2,diff})^2$ and R_2' if this ratio is measured at two or more echo times. M can then be estimated using

$$M = e^{R_2'\cdot \mathrm{TE}_{func}} - 1 \simeq R_2'\mathrm{TE}_{func}, \quad (6.8)$$

where TE_{func} is now the BOLD echo time of the functional experiment that the calibration is to be applied to.

Alternatively, one could use a fixed TE and fit the quadratic dependence of Eq. (6.7) using several values of τ. However, more data would be required to fit the quadratic relationship and other experiments and theories of SE decay have shown that this ratio can become quadratic around the SE as a function of TE or τ in the absence of diffusion [1,5,161]. Therefore, these two distinct quadratic behaviours could confound the estimate of $(R_{2,diff})^2$.

6.5 Methods

6.5.1 Simulations

The simulations in this study used the deterministic diffusion method [83]. This consisted of populating a two-dimensional (2D) plane with vessels to the desired CBV, where blood vessels were modelled as cylinders perpendicular to the plane. To model the random orientation of the vessels, the direction of the main B_0 field was randomized for each vessel [88]. This vessel-wise randomization of the B_0 direction was used rather than physically reorienting the vessels relative to the plane because it resulted in a more easily controlled CBV and still generated the desired distribution of field offsets since the field offsets along a direction parallel to a cylinder are invariant. An example vessel distribution and the resulting field offsets are shown in Figure 6.6.

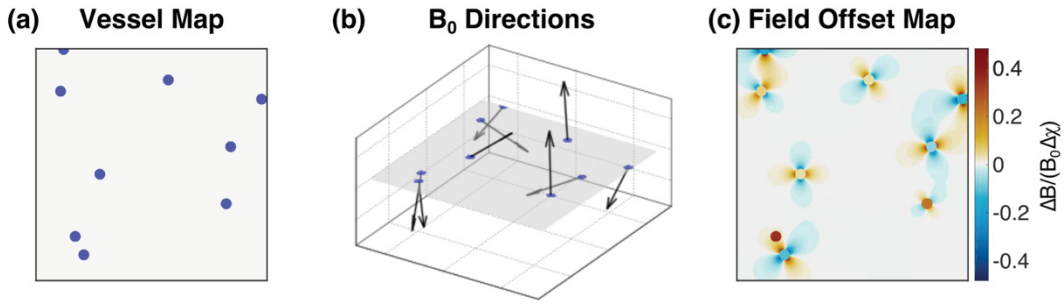

Figure 6.6: 2D vessel map and its field inhomogeneity map (single radius)

(a) Example 2D vessel map. The blue circles correspond to the vessel cross sections. (b) The random B_0 directions assigned to each vessel. The directions are represented by the arrows and are overlaid on a semi-transparent version of the vessel map. (c) The field offset map generated by the vessels. All the vessels were assigned the same susceptibility offset, $\Delta\chi$, and the map was normalized by $B_0\Delta\chi$.

The deterministic diffusion simulation method spatially discretizes the area over which the simulation is run onto a lattice and, for a given distribution of vessels, calculates the field offsets generated by them over this lattice [73,83]. Following an initial 90° excitation pulse, each element of the lattice has a uniform magnetization with an initial phase of 0 and magnitude of 1. In time steps, δt, the magnetization at the (k,l)-th lattice element, M_{kl}, precesses by an angle $\Delta\phi_{kl} = \gamma\, \Delta B_{kl}\, \delta t$, where ΔB_{kl} is the field offset at that lattice element. Diffusion is modelled by an isotropic, Gaussian blurring of the magnetization along each dimension independently. This was implemented by linear convolution of the magnetization with the 1D discrete diffusion kernel with a width parameter equal to the expected mean-square displacement of the spins, $\sigma^2 = 2D\delta t$, where D is the diffusion coefficient of water in tissue [95]. The k-th element of the kernel is given by

$$D_k = e^{-(\sigma/\Delta x)^2} I_k((\sigma/\Delta x)^2), \tag{6.9}$$

where Δx is the physical spacing between lattice elements and I_k is the modified Bessel function of the first kind of order k. The half-width of the kernel was a minimum of 6σ and was extended, if necessary, until $1 - \Sigma D_k \leq$ 5e-8. This requirement ensures that the kernel is normalized and it was empirically tested for accuracy with preliminary simulation tests. 180° refocusing pulses were modelled by taking the complex conjugate of the magnetization at each lattice element. Finally, the signal magnitude at the n-th time point is given by

$$S_n = \frac{1}{N^2}\left|\sum_{k,l} M_{kl,n}\right|, \tag{6.10}$$

where N is the number of lattice elements summed along each dimension and the sum was only performed over the central 1/3 of the lattice width along each dimension to avoid convolution edge effects.

The field offsets generated by each vessel were given by modelling them as infinite cylinders perpendicular to the simulation plane with [52]:

$$\Delta B_0 = \begin{cases} \frac{1}{2}\Delta\chi B_0 \left(\frac{R}{r}\right)^2 \sin^2(\theta)\cos(2\phi) & r \geq R \\ \frac{1}{6}\Delta\chi B_0 (3\cos^2(\theta) - 1) & r < R \end{cases}, \quad (6.11)$$

where R is the vessel radius, r is the distance from the point of interest to the centre of the vessel, θ is the angle between B_0 and the centre line of the vessel, ϕ is the angle between the vector defined by r and the component of B_0 in the plane, and $\Delta\chi$ is the susceptibility difference between the blood within the vessel and the surrounding tissue. The field offsets from each vessel were independently calculated and summed across the lattice to give ΔB_{kl}.

To determine the echo time dependence of the SE attenuation, simulations were run from time 0 (i.e., immediately after excitation) up to the spin echo time (t_{SE}), with t_{SE} incremented in 4-ms steps from 4 to 100 ms. Since the simulations only ran up to t_{SE}, the ASE signals were determined using negative ASE offsets (i.e., $\tau < 0$) and testing showed that the signal difference for positive vs. negative τ was negligible (results not shown). Simulations were performed using B_0 = 3 T, CBV = 2% (representing venous CBV), $\Delta\chi = 4\pi \cdot 0.04$ ppm, diffusion coefficient D = 0.8 μm^2/ms, and time step δt = 0.25 ms. This $\Delta\chi$ approximately corresponds to vessels with an SO_2 of 60% and hematocrit of 40% and where tissue has the same susceptibility as fully oxygenated blood [103,138]. Ten networks were randomly seeded with 1.0-μm vessels on a 1020^2 lattice with a side length of 255 μm isotropic. At this resolution, each vessel could be sampled up to eight times across its diameter, and using higher resolutions had a negligible impact on the results. These networks were reused to perform the simulations for radii up to 20 μm by assigning them an effective lattice size of 255 μm × R/1.0 μm. For $R \geq 20$ μm, the same scaling was employed,

however, the lattice was resampled to a 6375^2 grid to ensure the diffusion kernel and field offset map were sampled at a high enough spatial resolution. All simulations were run using MATLAB R2015a (MathWorks, Natick, MA).

For the vessel-size distributions, the Lauwers distribution was obtained using the parameters for the complete vessel network in [46] with the radii ranging from 3.0–40 μm. The Frechet distribution was implemented in MATLAB using the *gevrnd* function with the input parameters $\mu = 10.1$ μm, $\sigma = 5.8$, and $k = 0.41$ taken from [49] and with the radii ranging from 2.5–60 μm.

To evaluate the hypothesis that $\ln(S_{SE}/S_{ASE})$ may have a linear dependence on TE, the ratio was calculated from the previous simulations as a function of TE and τ. The calibration constant, M, was then calculated from simulations with a finer division of radii from 1–100 μm and the Lauwers and Frechet radii distributions using two TEs to fit for R_2' and $(R_{2,diff})^2$ with Eq. (6.7). We tested this with $\tau = +30$ ms and TEs of 40 ms and 50 ms. The fitted R_2' values from the two different τ values were substituted into Eq. (6.8) to calculate M using $TE_{func} = 30$ ms. For comparison, M was also calculated at a single TE of 40 ms with $\tau = +30$ ms using Eq. (6.4), as in Blockley et al. [27]. These ASE-based M calculations were compared against the "ideal" M given by the maximum possible gradient echo percent signal change at TE = 30 ms. Since these simulations ignored T_2 relaxation, the maximum signal was taken to be 1.

6.5.2 In Vivo Study

MR Imaging

We evaluated the quadratic ASE model on nine healthy participants (4 female, 5 male; 19–39 years of age; mean age = 28 ± 7 years) using a 3 T scanner (Discovery 750, GE Healthcare, Waukesha, WI). The study was approved by our institutional review board and all participants gave informed written consent. Subjects were scanned with a 2D ASE EPI sequence with FLAIR preparation. Imaging parameters included: field of view = 224×224 mm^2; 96×96 matrix; bandwidth = 250 kHz; slice thickness = 2.0 mm + 1.0-mm gap; 34 slices (interleaved); flip angle = 90°; ASSET factor = 2; four TEs of 42, 50, 60, and 70 ms; τ = 0 and 30 ms; inversion time (TI)/repetition time (TR) = 2.0/8.0 s. This combination of TI/TR was determined to null the signal from CSF in preliminary testing on two additional subjects. Slices were angled parallel to the anterior commissure-posterior commissure line and aligned to the top of the brain. This typically resulted in whole-cerebrum coverage and partial cerebellum coverage. For each TE-τ image, 15 complex volumes were acquired with two additional dummy volumes.

During the hypercapnic calibration, participants were imaged with a dual-echo pseudo-continuous arterial spin labelling (ASL) sequence with a 2D EPI readout and the following imaging parameters: field of view = 224×224 mm^2; 64×64 matrix; bandwidth = 250 kHz; slice thickness = 5.0 mm + 1.0-mm gap; 18 axial slices acquired in a top-down order; flip angle = 90°; ASSET factor = 1.5; TE_1/TE_2 = 9.5/30 ms; TR = 3.6 s; ASL label duration = 1600 ms; post-label delay = 900 ms. Slices were aligned to the top of the brain and the labelling plane was located 20 mm inferior of the most inferior slice. 100 volumes were acquired with four additional dummy volumes.

A separate B_0 field map was acquired using a 2D, fast spoiled gradient recalled echo, three-echo sequence with a monopolar readout, a field of view matched to the ASE images, 256×256 matrix, TE_1 = 4.45 ms, echo spacing = 2.1 ms, TR = 500 ms, and flip angle = 30°. High resolution structural images were acquired using a 3D MP-RAGE acquisition [162] with a 1-mm isotropic resolution, 192×256×256 matrix, TR/TI/TE = 6.66/650/2.93 ms, and 10° flip angle.

Hypercapnia Gas Challenge

All subjects underwent a hypercapnic gas challenge in the MR scanner consisting of breathing medical air for 2 min, 5% CO_2 in medical air for 2 min, then medical air for 2 min. Participants were delivered the gases with an automated flow controller (FloBox 954, Sierra Instruments, Inc., L Monterey, CA) connected to a non-rebreathing circuit with an extended expired gas reservoir that was open to the room at its end [163]. Gases were delivered at a constant flow rate of 20 l/min, and partial pressures of oxygen and carbon dioxide in the breathing mask were monitored with BIOPAC $O_2$100C and $CO_2$100C modules connected to a BIOPAC MP150 acquisition unit (BIOPAC Systems, Inc., Goleta, CA). The mean end-tidal partial pressures of CO_2 ($P_{ET}CO_2$) and O_2 ($P_{ET}O_2$) at rest were determined from the 60 s of end-tidal measurements prior to the hypercapnia challenge, and the mean changes in the end-tidal values were determined from the final 60 s of the hypercapnia challenge.

Image Processing

All image analysis was ultimately performed in the individual subjects' ASL image space, however, image preprocessing was generally performed in each image's native space. A combination of tools from Statistical Parametric Mapping (SPM) 8 (Wellcome Trust Centre for

Neuroimaging, London, UK), FMRIB Software Library (FSL) v5.0.7 [164], and MATLAB were used for image analysis.

For each TE-τ ASE combination, the image volumes were motion corrected using SPM *realign*, complex-averaged across time, then converted to magnitude images. The mean magnitude images were coregistered to the mean TE/τ = 42/0 ms image using SPM *coreg* and then brain extracted using FSL *BET* [165]. The TE/τ = 42/0 ms brain extracted, distortion corrected image is referred to as the ASE reference image. Geometric distortion correction of the images was performed using the B_0 field map with FSL *FUGUE* [166]. The field map was fit by nonlinear estimation in the complex domain [167] and smoothed by fitting it to a 3D smoothing spline in MATLAB. Voxels in the ASE images where the estimated distortion was greater than 1 voxel were excluded from later analyses.

The ASL images were motion corrected using the SPM ASL toolbox [168]. Simultaneous geometric distortion correction and registration of the mean echo 1 image to the structural image was performed using boundary-based registration with FSL's *epi_reg* utility (white matter (WM) segmentation described below) [169,170]. The distortion correction was then applied to all echo 1 and echo 2 images.

Calculation of the *M* values was performed on anatomically defined grey matter regions of interest (ROIs). Segmentation of the structural image was performed using SPM8 *new segment* [171], giving tissue probability maps and the nonlinear deformation into MNI space. The inverse deformation fields were used to transform four atlas-based ROIs corresponding to the frontal, occipital, parietal, and temporal lobes from MNI space to subject space [172]. These ROIs were then multiplied with the GM tissue probability maps, transformed to ASL-space, and thresholded

at 0.75 to produce binary masks. A fifth ROI consisting of all GM thresholded at 0.75 was also used. The transformation matrices to the structural image for the ASE reference image were estimated using *epi_reg*: given the lack of GM-WM contrast and the pronounced CSF-parenchyma contrast in the FLAIR-ASE images, the CSF segmentation was used for the contrast boundary.

Macroscopic field inhomogeneities unequally affect the ASE and SE signal intensities and, hence, the apparent R_2'; therefore, several efforts were made to exclude regions of excess signal intensity distortions arising from field inhomogeneities and to compensate for moderate signal dropout. The field gradients across the slice, frequency, and phase encode directions were calculated numerically by central differences on the smoothed field map. The $\tau = 30$ ms ASE image intensities were corrected for gradients across the slice, G_s, by dividing them on a voxel-wise basis by the factor $sinc(\gamma G_s \tau \Delta z/2\pi)$ [1], where $\gamma = 2.675\times10^8$ rad/s/T is the gyromagnetic ratio of ^{1}H, and Δz is the slice thickness. The sinc correction method relies on an ideal square slice profile; this assumption was tested using Bloch simulations of the pulse sequence and by measurement of the slice profile in a phantom and it was found to be in close agreement up to the first zero of the sinc function. Voxels where the sinc term was less than 0.5 were excluded from the ROIs for analysis. In-plane field gradients can lead to gradual dephasing and, for gradients above a critical threshold, can push the gradient echoes in the EPI readout trajectory out of the *k*-space acquisition window, resulting in abrupt signal loss [173,174]. Therefore, only voxels where the in-plane gradient magnitude was less than 50% of the critical gradient magnitude were included for analysis. This corresponded to including voxels where the gradient magnitude was less than 84 μT m^{-1} along the readout direction and less than 56 μT m^{-1} along the phase encode direction. Despite these precautions, the estimated R_2' values in the temporal lobe were still artefactually elevated; therefore, only slices superior to the cerebellum were included in the ROIs for analysis.

Data Analysis

After transformation of all ASE images into each subject's own ASL space, their intensities were averaged across the five ROIs and the ratio of the mean SE over the mean ASE signal was calculated at each echo time. Non-linear fitting of this ratio vs. TE to the q-ASE model in Eq. (6.7) was performed in MATLAB using *lsqcurvefit* with the trust-region-reflective algorithm. This resulted in fits for R_2' and $(R_{2,diff})^2$ from which M was then determined using the non-linearized version of Eq. (6.8). Whether the q-ASE model statistically significantly increased the M values relative to those determined using only the TE = 42 ms data was assessed using a single-sided Wilcoxon signed rank test for each ROI, with $P < 0.05$ deemed significant.

For comparison, M was calculated across the ROIs from the dual-echo ASL images during the hypercapnia challenge. To calculate CBF-weighted changes, tag-control subtraction of the first echo images was performed using sinc interpolation. The second echo images were used as BOLD-weighted images. The percent signal changes of the BOLD and CBF signals were determined from their modelled responses using a general linear model analysis on the averaged signals across the ROIs [36]. Both the averaged BOLD and CBF signal time courses were modelled by convolving the hypercapnia stimulus paradigm with a gamma-variate function with a mean lag of 30 s and a standard deviation of 15 s [175]. The temporal derivative was included as an additional regressor to account for temporal delays in the responses. In the BOLD images only, linear drift and tag-control nuisance regressors were included. M values for each ROI were then calculated using Eq. (6.2) with $\alpha = 0.2$ [67] and $\beta = 1.3$ [151,176]. Whether the hypercapnic M values differed significantly from the ASE and q-ASE M values was determined using a two-sided Wilcoxon signed rank test for each ROI, with $P < 0.05$ deemed significant.

6.6 Results

6.6.1 Simulations

The quadratic decay term, $(R_{2,diff})^2$, is visualized in Figure 6.7 by plotting the initial slope of ΔR_2 vs. TE for the SE signals. The fitted slopes, which give $(R_{2,diff})^2$ by Eq. (6.6), appear to follow a sigmoidal relationship that is monotonically decreasing with vessel radius, as shown in Figure 6.7b. The $(R_{2,diff})^2$ values for the Lauwers and Frechet vessel radius distributions are (14.1 ± 0.5) s^{-2} and (5.3 ± 0.6) s^{-2}, respectively. From Figure 6.7a and c, if $(R_{2,diff})^2$ was estimated by fitting the tangent at later times, there would be an underestimation that would be worse for the smaller radii.

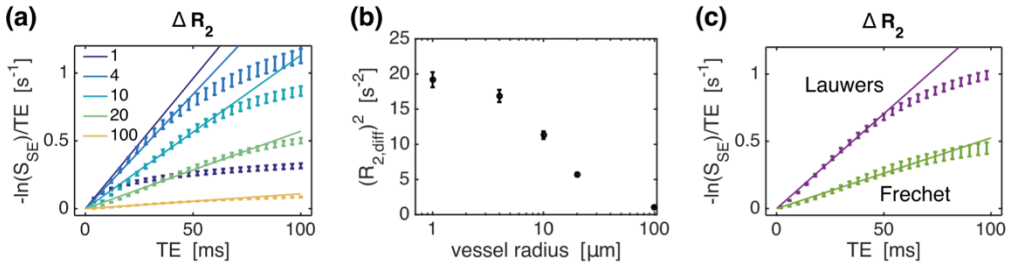

Figure 6.7: The TE-dependence of ΔR_2.

The dependence is given for individual radii (in μm) (a) and for the two distributions of radii (c). Error bars in (a) and (c) show the mean ± SD of the simulated ΔR_2 values. The initial relationships of ΔR_2 vs. TE are plotted with the straight lines. The slopes of the lines reflect the $(R_{2,diff})^2$ term and those values from (a) are plotted as a function of vessel radius in (b). The slopes in (c) for the Lauwers and Frechet distributions are (14.1 ± 0.5) s^{-2} and (5.3 ± 0.6) s^{-2}, respectively.

The log-ratio, $\ln(S_{SE}/S_{ASE})$, as a function of TE is shown in Figure 6.8 for a subset of τ offsets. For a given TE and given τ, the curves for each radius are vertically offset from each other and they increase monotonically with vessel size. This reflects the true difference in R_2' for the different vessel sizes that is widely known for GE BOLD [17]. At the vessel-size extremes of 1 μm and 100 μm, both ratios are relatively flat as a function of TE. These arise from two different mechanisms, however. The ratio is flat for the 1-μm simulations because the signal rapidly transitioned from quadratic to linear decay, as observed in Figure 6.3. Conversely, the ratio is relatively flat for the 100-μm simulations because the diffusion-induced SE attenuation is small since the scale of diffusion is much less than that of the field offsets surrounding the vessels. In between these radii, it can be seen how the curves transition. For the shortest τ offset, the slopes monotonically decrease with increasing radius (ignoring the 1 μm simulations). At the later τ offsets, the slopes no longer decrease monotonically with increasing radius but rather they peak around 10 μm. This change in behaviour with increasing τ is the result of the early quadratic decay being missed in the SE signals for the smaller vessel sizes as TE is increased, as predicted above by Figure 6.7.

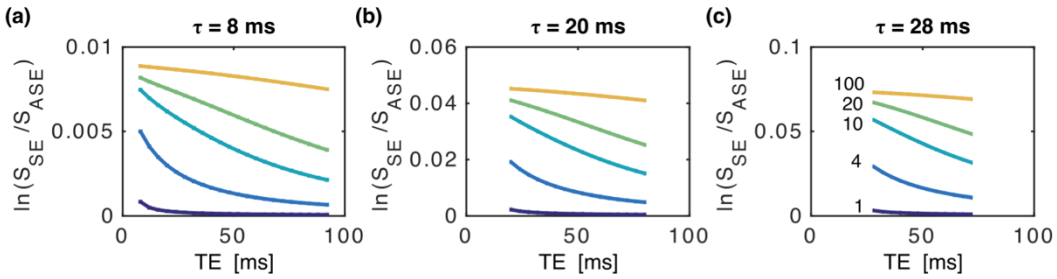

Figure 6.8: The SE/ASE log-ratio for individual radii.

The radii, in μm, are labelled in (c). Error bars represent the mean ± SD of the log-ratio across all simulated networks although they are mostly obscured by the connecting lines.

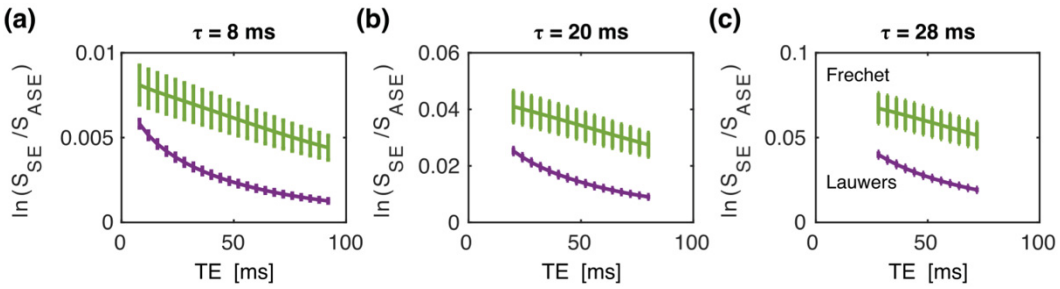

Figure 6.9: The SE/ASE log-ratio for the Lauwers and Frechet vessel-size distributions. The distributions are labelled in (c). Error bars represent the mean ± SD of the log-ratio across all simulated networks.

These same ratios are shown for the Lauwers and Frechet vessel-size distributions in Figure 6.9. These results are consistent with those of the individual radii above. The error bar sizes vary between the two distributions because there were far more vessels per network in the Lauwers simulations than the Frechet simulations. The vertical offset between the two curves reflects the intrinsic differences in R_2' between the two vessel-size distributions; the Frechet distribution has larger ratios because its vessel sizes are larger overall. The slope of the Lauwers curve at the smallest τ is initially steeper than that of the Frechet curve but it plateaus at the later echo times. The slope of the Frechet curve is relatively unchanged from τ-to-τ.

Figure 6.10 shows the results of calculating M using the ratio $\ln(S_{SE}/S_{ASE})$ at a TE of 40 ms with τ = 30 ms (denoted M_{ASE}). When the ratio from TE = 50 ms was incorporated to calculate R_2' and $(R_{2,diff})^2$ using the q-ASE model, almost all radii's M values were substantially increased (denoted $M_{q\text{-}ASE}$). These ASE-based M values were compared against the "ideal" M value (M_{ideal}), calculated as the maximum possible GE BOLD percent signal change at TE = 30 ms. M_{ASE} only agreed to within 5% of M_{ideal} for radii > 40 μm, whereas for $M_{q\text{-}ASE}$, this level of agreement was

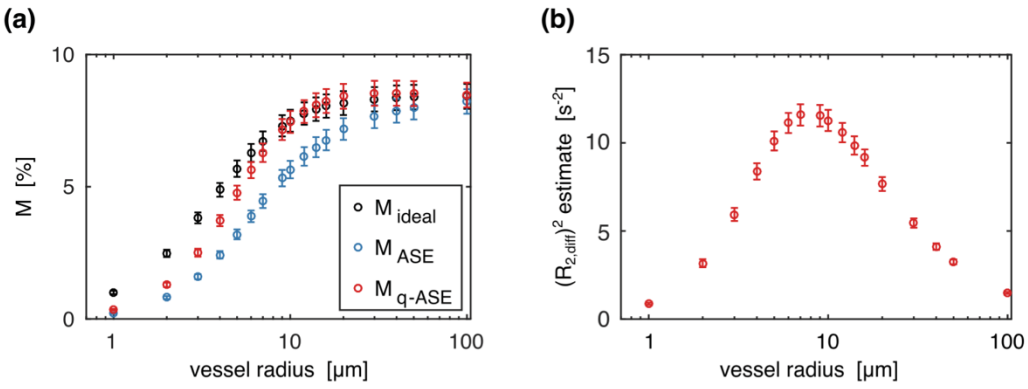

Figure 6.10: Simulated *M* values across radii.

(a) Radius-wise comparison of the ideal *M*-values (M_{ideal}) calculated from the maximum GE BOLD signal at TE = 30 ms vs. *M* when calculated using $\ln(S_{SE}/S_{ASE})$ at a TE of 40 ms with τ = 30 ms (M_{ASE}) and *M* when calculated using the quadratic ASE signal model ($M_{q\text{-}ASE}$) to fit for R_2' and $(R_{2,diff})^2$ with SE and ASE signals at TE = 40 and 50 ms. (b) The estimated $(R_{2,diff})^2$ values from the q-ASE model for each vessel radius. Error bars represent the mean ± SD across all simulated networks.

attained for radii > 7 μm. The corresponding estimated $(R_{2,diff})^2$ values are shown in Figure 6.10b. Similar results are observed in the Lauwers and Frechet radius distributions in Table 6.1.

6.6.2 In Vivo Imaging

The ratios of the SE and ASE signals, $\ln(S_{SE}/S_{ASE})$, were calculated for all subjects from the image intensities averaged across the GM ROIs. In one of the subjects, these ratios displayed substantially more variability than in the other subjects resulting in this subject being excluded from any analyses. The ratios from the remaining subjects are shown in Figure 6.11 along with their model fits to Eq. (6.7). Included in Figure 6.11 are the average model fits derived from the mean of all subjects' fitted R_2' and $(R_{2,diff})^2$. Those fits are tabulated in Table 6.2.

Table 6.1: Mean simulated *M* values from the vessel-size distributions.

M_{ideal} is the maximum percent GE BOLD signal at TE = 30 ms; M_{ASE} is the estimated M value from $\ln(S_{SE}/S_{ASE})$ with τ = 30 ms at either TE = 40 or 50 ms; $M_{q\text{-}ASE}$ is the estimated M value using the ASE and SE signals from both TEs and fitting for $(R_{2,diff})^2$ and R_2' prior to calculating M. The corresponding estimated $(R_{2,diff})^2$ values from the q-ASE fitting are also given. Values are displayed as mean ± SD.

M calculation	Lauwers			Frechet		
	M [%]	M/M_{ideal}	$(R_{2,diff})^2$ [s^{-2}]	M [%]	M/M_{ideal}	$(R_{2,diff})^2$ [s^{-2}]
M_{ideal} (TE = 30 ms)	5.8 ± 0.2			8.2 ± 1.1		
M_{ASE} (TE = 40 ms)	3.6 ± 0.2	0.62 ± 0.01		7.0 ± 1.0	0.86 ± 0.01	
M_{ASE} (TE = 50 ms)	3.1 ± 0.2	0.53 ± 0.02		6.6 ± 0.9	0.81 ± 0.02	
$M_{q\text{-}ASE}$	5.2 ± 0.3	0.88 ± 0.01	9.3 ± 0.4	8.3 ± 1.1	1.02 ± 0.02	6.5 ± 0.8

The ASL data from another subject were excluded due to improper labelling plane positioning. The remaining 7 subjects' mean changes in $P_{ET}CO_2$ and $P_{ET}O_2$ during the hypercapnia challenge were 9 ± 2 mm Hg and 15 ± 5 mm Hg, respectively. The gas delivery was not iso-oxic although this would only give an average change in arterial SO_2 from approximately 97% at rest to 98% during hypercapnia [32], resulting in a negligible contribution to the BOLD signal.

The mean calibration constants in the GM ROIs as determined from hypercapnia (M_{HC}), ASE at TE = 42 ms (M_{ASE}), q-ASE fit with the first three TEs ($M_{q\text{-}ASE}$ (3 TEs)), and q-ASE fit with all four TEs ($M_{q\text{-}ASE}$ (4 TEs)) are displayed in the bar plot in Figure 6.12.

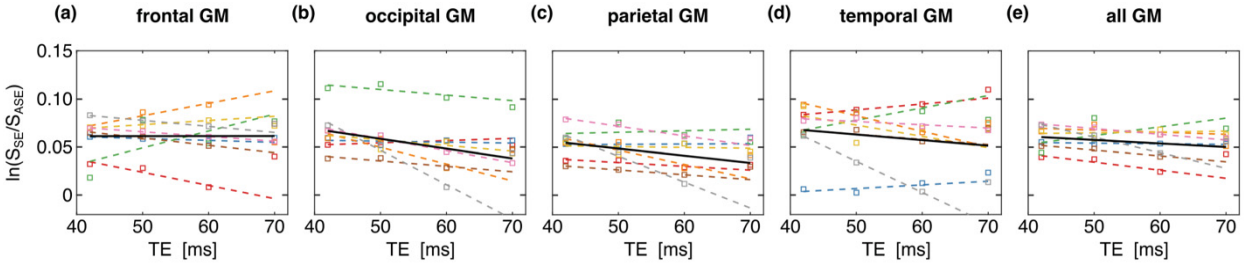

Figure 6.11: The SE/ASE log-ratio in vivo as a function of TE for the grey matter ROIs.

Individual subjects' values are plotted with the coloured markers and their resulting fits to Eq. (6.7) with the first three TEs are plotted with the coloured dashed lines. The mean fits are represented by the solid black lines. All axes share the same set of axis labels as (a). GM: grey matter.

Table 6.2: In vivo $(R_{2,diff})^2$ values across grey matter.

The mean ± SD in vivo $(R_{2,diff})^2$ values across the grey matter (GM) ROIs of 8 subjects. The fits for $(R_{2,diff})^2$ were performed using either the first three echoes or all four echoes.

# of Echoes in q-ASE Fit	Mean $(R_{2,diff})^2$ [s^{-2}]				
	Frontal GM	Occipital GM	Parietal GM	Temporal GM	All Grey Matter
3	-0.1 ± 18	17 ± 20	12 ± 16	10 ± 24	6 ± 12
4	-1 ± 11	9 ± 10	6 ± 7	3 ± 15	2 ± 7

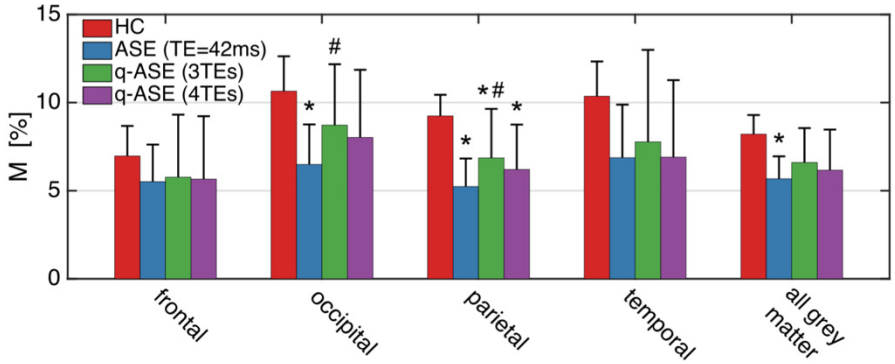

Figure 6.12: Comparison of *M* in the grey matter ROIs averaged across 7 subjects.

M was measured using hypercapnia (HC), from the first ASE echo time (ASE (TE=42 ms)), with the q-ASE model fit to the first three TEs (q-ASE (3TEs)), or all four TEs (q-ASE (4TEs)). * denotes the ASE or q-ASE *M* values were significantly different from the HC values ($P < 0.05$). # denotes the q-ASE *M* values were significantly greater than the ASE (TE=42ms) *M* values ($P < 0.05$).

6.7 Discussion

Gas-free fMRI calibration holds great appeal for improving access to calibrated fMRI methods; however, technical challenges still impede its adoption. In this study, we have examined SE attenuation resulting from diffusion through the microvasculature with the principal aim of being able to compensate for this attenuation in calibration. Despite SE attenuation being a well-known phenomenon, it has generally been disregarded in earlier studies using gas-free calibration [24,25,28] or acknowledged as a limitation of current implementations [27]. Here, we have shown that the attenuation substantially reduces the calibration constant when estimated with ASE imaging, in line with previous analytical simulations and in vivo measurements [27], but that the underestimation can be compensated by acquiring additional ASE images.

6.7.1 Microvascular Simulations

Using simulations from networks of vessels with identical radii and from two different distributions of radii, the general nature of the SE attenuation became much more apparent. By empirically describing the attenuation by a quadratic-exponential decay early on and a linear-exponential decay later, it was possible to identify several features of it: i) the overall magnitude of the attenuation is largest for intermediate vessel sizes; ii) the time to transition from quadratic to linear decay is proportional to vessel size; and iii) the attenuation at later ASE offsets ($\tau \neq 0$) can approximately be described by the SE ($\tau = 0$) attenuation but translated in time by τ and with an additional offset given by the intrinsic R_2' weighting. The first feature is already well known from SE BOLD vessel-size sensitivity studies [17,61,62]. The second and third features are novel findings of this study and led us to propose the quadratic ASE (q-ASE) biophysical signal model, described by Eqs. (6.5)–(6.7), with the addition of the diffusion-induced attenuation constant, $(R_{2,diff})^2$. This model correctly predicts that $\ln(S_{SE}/S_{ASE})$ underestimates M, and, crucially, it allows for the underestimation to be quantified by measuring the SE and ASE signals at two or more TEs. A model where the decay exponent was not exactly 2 but was empirically determined was considered; however, it was decided to keep the exponent at 2 based on the simplicity with which it allows the fitting of $\ln(S_{SE}/S_{ASE})$ vs. TE and based on the success with which it corrected the M values in simulations. In contrast to the simulations here, previous analytical calculations using a detailed BOLD signal model accounted for SE attenuation by modelling it as a linear exponential decay [26,27]. Those calculations also predicted an underestimation of M, however, as shown above, the linear decay does not provide a means by which it can be easily corrected.

A consequence of the transition from quadratic to linear decay is that the window of time to characterize the SE attenuation is limited: once the signal transitions to linear-exponential decay,

the attenuation becomes indistinguishable from intrinsic R_2 and gives a decreased apparent R_2' (and, therefore, decreased M). This is evident when comparing the estimated $(R_{2,diff})^2$ values from the simulations in Figure 6.10b and Table 6.1 with the true $(R_{2,diff})^2$ values in Figure 6.7. The true $(R_{2,diff})^2$ values are largest for the smaller radii and decrease monotonically with increasing radius, however, the estimated $(R_{2,diff})^2$ values peak for the intermediate vessel sizes. Because of this, the q-ASE model is still unable to effectively compensate for the underestimation in M for the smallest vessel sizes, whereas it performs remarkably well for intermediate to large radii. Physiologically, this would correspond to the correction working for most post-capillary vessels if one takes the upper cut-off radius for capillaries to be ~4–5 μm [19,40,46-48]. Note that, referring to a "true" $(R_{2,diff})^2$ value is also not entirely accurate since the estimation of it was still dependent on the limits over which it was fit .

6.7.2 In Vivo Imaging

Encouraged by the simulation results, we sought to determine the feasibility of measuring $(R_{2,diff})^2$ in vivo and to compensate for the SE attenuation during calibration. We measured SE and ASE images (τ = 30 ms) at TEs of 42, 50, 60, and 70 ms with the CSF signal nulled to avoid its contamination of R_2'. Anticipating that the ratio of the SE over the ASE signal could plateau at later echo times, we fit for $(R_{2,diff})^2$ and R_2' using either the first three TEs or all four. Independent of the number of TEs, there was considerable variability in the fits across subjects that resulted in positive and negative values for $(R_{2,diff})^2$; however, for all but the frontal GM ROI, the mean fits resulted in positive $(R_{2,diff})^2$ (Table 6.2), and the values were in line with those predicted by the simulations. The mean $(R_{2,diff})^2$ values were larger for the three-TE fits vs. the four-TE fits, perhaps implying that $\ln(S_{SE}/S_{ASE})$ does plateau beyond TE = 60 ms. The resulting increases in M were

significant in the occipital and parietal ROIs for the three-TE fit but not the four-TE fit, further suggesting that the data at the later echoes should not be used (Figure 6.12). Relative to hypercapnia, the ASE-based M estimates all underestimated M_{HC}, although the underestimation was not statistically significant for all comparisons.

Note that although M_{HC} was used for comparison, this does not imply that it is the standard for calibration. As discussed in the Introduction, hypercapnic calibration suffers from its own setbacks and technical challenges, including what exact values to use for α and β [18,20]. This means that the true magnitude of the underestimation of M in the ASE methods could be less (or more) than implied by the comparison against M_{HC}. Furthermore, if $CMRO_2$ were to decrease during the hypercapnic challenge, then the true M_{HC} would be less than the estimated value and could account for a significant fraction of the discrepancy [149,177]. An alternative measurement of R_2' may be a more appropriate comparison. This could consist of separate multi-echo GE and SE acquisitions, using a relatively short SE spacing to reduce the impact of diffusion-induced attenuation. In this case, multi-exponential decay would complicate the comparison but a correction could be incorporated [25].

When compared against the study by Blockley et al. [27], the measured M_{ASE} values relative to M_{HC} values are consistent. In that study, SE and ASE images were acquired at a single TE of 40 ms with a spiral readout with a marginally higher in-plane resolution, the same slice thickness, no CSF suppression, and similar post-processing steps. The mean ratio of M_{ASE}/M_{HC} across all GM was ≈ 0.9 in that study and ≈ 0.7 here for the 42-ms TE data. The reduced ratio was expected in our study because CSF suppression has been shown to reduce R_2' estimates in GM by ~20–30% [156,157]. This further underscores the importance that SE attenuation likely plays in the resulting underestimation of R_2' and M.

6.7.3 Biophysical Signal Modelling

The q-ASE signal model presented here is complementary to biophysical signal models that propose a Gaussian signal characteristic about the spin echo [5,158,178]. These signal models typically assume perfect SE refocusing and describe a Gaussian-like decay *around* the spin echo with respect to TE or τ, whereas the q-ASE model describes a Gaussian-like decay of the spin echo *itself* as a function of TE. These Gaussian SE signal characteristics are still present in our simulations (see the individual time series in Figure 6.2) since the simulations used no assumptions about the underlying frequency distribution shape (e.g. Lorentzian or Gaussian) other than that the individual fields produced by the vessels are modelled as dipoles from infinite cylinders. The quantitative BOLD model is one such model of Gaussian signal decay around the SE, and it is used to relate R_2' to deoxygenated-CBV and SO_2 [158]. Since this model ignores the effects of diffusion, it may benefit from the q-ASE model by correcting its estimate of R_2'.

Deriving more physiological quantities from the q-ASE model may be possible since $(R_{2,diff})^2$ does have some vessel-size/diffusion dependence that may be complementary to and overlapping with the dependence of R_2' on SO_2 and CBV [5]. A more thorough investigation spanning a range of CBV, SO_2, field strengths, etc. would be required to ascribe more physiological meaning to $(R_{2,diff})^2$. For now, the q-ASE model provides a means for describing the SE attenuation and we do not expect this conclusion to vary drastically with the normal range of physiological variability for reasons described next.

6.7.4 Limitations and Future Work

Some limitations of the simulations are that they were only performed at a single CBV and a single field offset strength (i.e., combination of B_0, SO_2, and hematocrit). Based on similar analytical signal models that also show SE attenuation that is approximately quadratic-exponential, such as the Gaussian phase approximation [131] or the weak field approximation [136], we expect $(R_{2,diff})^2$ to be directly proportional to CBV. What remains unclear, however, is how the time to transition from quadratic-exponential to linear-exponential decay may vary with changing CBV. The effect of changing the strength of the field offset, $\delta\omega$, is similar to changing the vessel radius, R. Typically this is summarized by the dimensionless quantity $\delta\omega R^2/D$ [60], such that changes in $\delta\omega$ or D can alternatively be considered as a change in R^2. This means that a doubling of $\delta\omega$ would correspond to a shift along the $(R_{2,diff})^2$-R curve by a factor of $\sqrt{2}$. In addition to this shift, by following the reasoning in Weisskoff et al. [54] regarding the expected dependence of ΔR_2 on $\delta\omega$, and defining $(R_{2,diff})^2$ as $d^2 \ln S_{ASE} / dt^2$, then $(R_{2,diff})^2$ would also need to be scaled by 2^2. Altogether, if $\delta\omega$ is scaled by a factor λ, then the new $(R_{2,diff})^2$ can be estimated from

$$\left(R_{2,diff}\right)^2(\lambda \cdot \delta\omega, R, D) = \lambda^2 \cdot \left(R_{2,diff}\right)^2\left(\delta\omega, \sqrt{\lambda}R\,, D\right) \tag{6.12}$$

Since the "true" $(R_{2,diff})^2$ is a monotonic decreasing function of radius, the factor on the right would be sub-linear such that the net proportionality to λ would be less than quadratic.

Another important limitation of this study is that it ignored intravascular (IV) signal. IV signal has a significant contribution to the BOLD effect at field strengths of 1.5 T and 3 T because of hydrogen nuclei's proximity to hemoglobin [9]. IV spins are typically considered to be in the motional narrowing regime [60], which would relate to the smallest radii simulated here. In this case, IV SE attenuation would quickly reach linear-exponential decay and would be irrecoverable.

This would further contribute to the early plateau of $\ln(S_{SE}/S_{ASE})$ vs. TE and the consequent underestimation of M. Applying IV crushers may increase the estimated M values [161].

Despite considerable efforts to reduce R_2' contributions from macroscopic field inhomogeneities in vivo, the results in the frontal and temporal ROIs were still inconsistent with the results in the occipital and parietal ROIs. The M values in the frontal and temporal ROIs were in the range of the other ROIs', suggesting that the bulk effects of the field inhomogeneities were largely avoided; however, the increase in M from the q-ASE model failed to reach statistical significance in the frontal and temporal ROIs, suggesting that there was increased signal variability in these regions that could arise from residual field effects. In future studies, further increasing the spatial resolution and/or performing z-shimming could help alleviate these issues but at the expense of increased readout and/or scan time [179].

This study also did not show any causal relationship between the measured $(R_{2,diff})^2$ and R_2' parameters and blood oxygenation. While beyond the scope of this study, this could be done by repeating the ASE imaging experiments during a hypercapnia or hyperoxia challenge. Given the large variability of $(R_{2,diff})^2$ measured here, either the imaging technique would require further refinement to be more sensitive to the small changes in $(R_{2,diff})^2$ expected from a gas challenge or a larger cohort of participants would be needed.

Ideally, one would like to apply the q-ASE correction using an individual's measured $(R_{2,diff})^2$ parameter. Unfortunately, this measurement added considerable time to the scan and it was quite variable on the individual subject-level – requiring the data from one subject to be excluded from analysis. Although it is expected that $(R_{2,diff})^2$ will have both a CBV and SO_2 dependence, it may be more beneficial to acquire SE and ASE images at a single TE and to apply

the q-ASE correction using an assumed $(R_{2,diff})^2$ value. This would be akin to the calibrated fMRI parameter β, which could be measured in vivo [63,65] but is generally assumed a constant across the brain. Considering the $(R_{2,diff})^2$ values from the simulations and the in vivo measurements, a value around 10–15 s^{-2} may be appropriate.

6.8 Conclusions

In this study, we sought to characterize the attenuation of SE and ASE signals arising from diffusion of water surrounding the microvasculature. Using simulations, we have shown how this attenuation varies for different vessel sizes and how it impacts gas-free calibrated fMRI based on ASE imaging. We have proposed that the initial attenuation be described as a quadratic-exponential decay term, $(R_{2,diff})^2$, such that it can be measured and compensated for by acquiring SE and ASE signals at multiple echo times. This strategy successfully corrected the underestimation of the fMRI calibration constant in the simulations for intermediate vessel radii and above. By replicating these experiments in vivo in healthy subjects, we showed that the M values obtained from the ratio of the SE and ASE images at a single TE could be significantly increased by incorporating the ratios from later TEs; however, they still tended to underestimate the M values obtained from the more common hypercapnic calibration. Future studies of gas-free calibration and R_2' imaging will benefit from incorporating an estimation of $(R_{2,diff})^2$ in their fitting or using an assumed value to compensate for the underestimation of R_2'.

6.9 Acknowledgements

This work was supported by the Canadian Institutes of Health Research [FDN 143290] and the Campus Alberta Innovates Program. The simulations in this study were enabled in part by support provided by WestGrid (www.westgrid.ca) and Compute Canada Calcul Canada (www.computecanada.ca).

Chapter 7

Discussion and Conclusions

7.1 Discussion

7.1.1 Hyperoxic BOLD Signal

HYPEROXIA in MRI has applications ranging from calibrating the BOLD signal [21,22], to measuring OEF, $CMRO_2$, CBV, microvascular venous vessel sizes [36,49,105], to monitoring tumour oxygenation [180]. These studies have assumed that the R_2^* changes during hyperoxia result from the passive increase in *venous* oxygenation and are not influenced by dissolved oxygen in *arterial* blood. By theoretically calculating and experimentally measuring the magnetic susceptibility of dissolved oxygen in plasma, it was argued here that this assumption was valid, save perhaps for conditions such as anemia. In conjunction with this study, Ma et al. [181] measured the R_1 ($1/T_1$), R_2, and R_2^* relaxation rates in oxygenated plasma samples. All relaxation rates were determined to significantly depend on pO_2 and with similar relaxivities (relaxation rate

per mm Hg). However, after incorporating these relaxivities into a detailed analytical BOLD signal model [18], they had a negligible contribution to the BOLD signal and the estimated fMRI calibration constant (M) up to arterial pO_2 levels of 610 mm Hg [181], in agreement with our prediction based on the susceptibility measurements.

At the same time as the studies above were conducted, Ozbay et al. [182] measured the susceptibility across the brain using quantitative susceptibility mapping during the breathing of medical air and of 100% O_2. CSF is an excellent model for in vivo validation of our measurements because it has a leaky barrier with the brain [39], allowing excess oxygen to diffuse from capillaries to parenchyma to CSF, and it lacks hemoglobin that would contribute to the susceptibility measurement. The choroid plexus, where CSF is produced, would also permit excess oxygen from capillaries to diffuse into ventricular CSF [39]; however, the vascularization of the choroid plexus itself could confound the susceptibility measurement from ventricles. In a section of brain that included the ventricles, the combined sulcal and ventricular CSF susceptibility was found to change by (3.8 ± 1.8) ppb across 14 healthy volunteers [182]. Using the oxygen solubility in water and the susceptibility of O_2 measured here (4.24×10^{-8} ml O_2/ml H_2O/mm Hg and 1040 ppm, extrapolated to 37 °C), this would correspond to a pO_2 increase of approximately (80 ± 40) mm Hg. In comparison, Zaharchuk et al. [98] measured the pO_2 of human bodily fluids in vivo using the pO_2 dependence of R_1 and found that sulcal CSF increased by ~100 mm Hg and ventricular CSF had no significant increase in pO_2 after 100% O_2 inhalation. The estimate of ΔpO_2 = (80 ± 40) mm Hg is in good agreement with these findings, although how much of that comes from ventricles vs. sulci is unclear.

This mounting experimental evidence from our own measurements and from other labs would suggest that the susceptibility of dissolved oxygen, while certainly measurable, is

insufficient to significantly confound the BOLD effect at the concentrations normally attained under hyperoxia. Other studies have reported negative BOLD signal changes in CSF and white matter during 100% hyperoxia and positive BOLD changes in cortical grey matter [106,183]. In one of these studies, performed in rats and mice, they attributed the negative BOLD change in white matter to the accumulation of oxygen in the extravascular space [183]. This explanation, while plausible, seems unlikely to be able to explain the whole effect considering the experimental findings discussed above. The negative BOLD change could be due to other factors, such as *hypo*perfusion induced by hyperoxia and/or concomitant decreases in blood CO_2 [153,154] or changes in macroscopic field inhomogeneities resulting from the changing O_2 content in air [106]. In humans, the latter effect is most noticeable around the nasal sinuses and ear canals, but in rodents it could be more extensive given their smaller brain volumes.

7.1.2 Intravascular Signal Modelling

The key findings from the intravascular signal modelling in Chapter 5 were: (1) a closed-form solution to the weak field approximation was derived and it can describe the transverse signal evolution for an FID, spin echo, or CPMG sequence; (2) when the volume fraction of the spherical perturbers was increased, the decay rates did not monotonically increase when sphere overlap was not allowed; (3) the WFA parameters, G_0 and r_c, could be empirically determined by fitting the radial correlation function of the perturbers and, when substituted into the closed-form solution, the signal evolution at high volume fractions could be accurately predicted; and (4) the empirically fitted r_c values deviated from their analytically predicted values when sphere overlap was not allowed and the deviation increased with volume fraction. Finding (2), where the relaxation rate did not monotonically increase, is a well-known phenomenon and had been reported early on by

Thulborn et al. [132] where they measured R_2 with increasing blood hematocrit. Finding (3) is a promising result because it implies that G_0 and r_c can be empirically determined for other perturber geometries (or volume fractions) that cannot easily be described analytically. In this case, any realistic geometry for red blood cells could be used, such as a biconcave disk.

Finding (4), that r_c varies with volume fraction, has potential implications for fitting the weak field approximation to experimental data, regardless if the fit is to the raw data with the closed-form solution or to the measured relaxation rates with the ΔR_2 model from Jensen and Chandra [76], as is typically performed [76,78,80-82]. If the effect is as large as the simulations indicate, then if one is fitting blood relaxometry data from samples with a range of hematocrits, then each sample should be fit for its own r_c value, otherwise, if the samples are simultaneously fitted, some model for how r_c should vary with hematocrit should be included. Given that the change in r_c was also dependent on how the spheres were distributed (randomly non-overlapping or hexagonal close packed), knowing how r_c might vary for realistic red blood cell shapes and distributions *a priori* is still premature. The shapes of RBCs may be adequately described by oblate spheroids or biconcave disks, for example, but their distribution and orientations could be highly variable, to the degree where they could be randomly spaced or they could string together forming a *rouleaux* [184]. This result may help explain why the weak field approximation failed to provide a reasonable fit to relaxometry data from post-natal umbilical cord blood in a recent study [82]. In that study, hematocrit was varied from 20–80% and a wide range of oxygenations were used and the relaxometry results from all blood samples were simultaneously fit to give a single r_c value for the entire set of samples (in addition to other model parameters). Trying to translate this finding to the exchange theory of relaxation, it is parameterized by a characteristic field shift between sites, $\Delta\omega$, and the lifetime between intra-/extra-cellular exchanges, τ_{ex}. $\Delta\omega$ can be considered the root

mean square field inhomogeneity, such that $(\Delta\omega)^2$ should be comparable to $\gamma^2 G_0$. If τ_{ex} is interpreted as a correlation time for field fluctuations, rather than strictly representing the exchange time between intra-/extra-cellular spaces [55,76,143], then it can be related to r_c through $\tau_{ex} \sim r_c^2/D$, such that τ_{ex} might be expected to vary as the volume fraction is increased. In their exchange model fit, Portnoy et al. [82] only fit for a single value of τ_{ex} across all samples, and did so without issue. This may be explained in part by the fact that $\Delta\omega$ was divided into two separate frequency shifts, $(\omega_{dia} + \omega_{oxy})$ and $(\omega_{deo} - \omega_{oxy})$, related to the diamagnetic and paramagnetic contributions to blood susceptibility. Therefore, there was an additional fitting parameter compared to the diffusion model fit that may help explain why the fitting to the diffusion model failed whereas the exchange model succeeded.

7.1.3 Gas-Free Calibrated fMRI

Our overall findings from the gas-free calibration study in Chapter 6 were consistent with previous studies: estimates of the fMRI calibration constant, M, from ASE-based measurements tend to underestimate M relative to hypercapnic calibration [27,185]. This was confirmed using detailed simulations and in vivo human experiments. The underestimation was attributed to the irreversible loss of phase coherence from diffusion surrounding the microvasculature. A method was proposed to correct the underestimation whereby the decay of the SE and ASE signals was described by a quadratic-exponential, with a rate constant $(R_{2,diff})^2$. This manifested as a linear decay of the ratio, $\ln(S_{SE}/S_{ASE})$, such that if this ratio at a single echo time was used as an estimate of M, it would underestimate the true value. This linear decay was observed in vivo and the mean $(R_{2,diff})^2$ values across subjects were consistent with the values predicted by simulations.

A limitation of the proposed quadratic-ASE model is that the decay transitions into a linear-exponential decay, where the SE attenuation becomes unrecoverable under the proposed method, limiting the range of echo times that can be used to measure $(R_{2,diff})^2$. This may explain why the increases in M were smaller when the ASE data from the longest echo time (70 ms) were used as compared to when only echo times up to 60 ms were used. In typical BOLD imaging experiments, SNR is optimized by setting the echo time to match the approximate T_2^* of tissue [186]. Similarly, it has been shown that the SNR of R_2' quantification is optimized when the echo time and ASE offset are approximately equal to the lesser of T_2' or T_2 [157]. Given T_2' ~300 ms [157] and T_2 ~100 ms [187] for grey matter, the SNR optimization of R_2' quantification would be improved at later echo times (~100 ms). This conflicts with the early echo time requirement to capture $(R_{2,diff})^2$ decay such that a compromise between each estimate's bias and precision must be made.

After the q-ASE correction, $M_{\text{q-ASE}}$ was generally still less than the hypercapnic M, M_{HC}. This could be the result of uncorrected SE attenuation from water surrounding capillary vessels and intravascular water. In reality, both estimates of M will have their own mutual bias relative to the "true" M. M_{HC} is influenced by the choice of calibration parameters, α and β [18,177]. α and β of 0.2 and 1.3, respectively, were used in this study, whereas Griffeth and Buxton [18] have suggested the use of empirically optimized values for 3 T of 0.14 and 0.91. Using these optimized values would *increase* M_{HC}, further widening the gap between M_{HC} and $M_{\text{q-ASE}}$. Conversely, an increasing number of studies suggest that hypercapnia results in a slight reduction of $CMRO_2$ [149,150,177,188], violating a fundamental assumption of standard fMRI calibration. In this case, estimates of M that ignore this decrease could *overestimate M* by up to 50% for $\Delta P_{ET}CO_2$ = 8 mm Hg [177]. This magnitude of overestimation could easily account for nearly all the discrepancy between M_{HC} and $M_{\text{q-ASE}}$, if not more.

The aim of this study was to provide an *alternative* means to calibrate the BOLD signal that was accurate and did not require any respiratory challenges or monitoring. The aim was not to replace the use of gases in all fMRI studies. The use of gases in fMRI provides valuable information on cerebrovascular health in a way that is relatively non-invasive and has high specificity to deoxyHb. R_2' alone can give us information related to blood oxygenation and blood volume but it lacks specificity and, unlike a CO_2 challenge, it does not measure vascular reactivity, a critical element of neurovascular coupling. Thus, gases in fMRI are likely to continue playing a valuable role in studying brain physiology.

7.2 Future Work

Regarding the impact of dissolved oxygen on the BOLD signal, this issue was carefully addressed both here and in our other study from Ma et al. [181]. Since those papers, the authors who proposed that dissolved oxygen in arteries would significantly impact the BOLD signal [23], have released a new study with similar simulations that have properly considered the susceptibility of dissolved oxygen [189]. Their new results show a negligible signal change from arteries, as we predicted.

Looking beyond the susceptibility of oxygen, a related topic of interest is the absolute susceptibility difference between arterial blood and parenchyma and how this may vary across tissue types and regionally. In BOLD imaging, it is generally assumed that the susceptibilities of blood and parenchyma are equal when blood is fully oxygenated (SO_2 = 100%). However, myelin and iron have been shown to vary across the cortex [190,191], and depending on the balance of water, lipid, iron, and calcium content, net tissue susceptibility could vary significantly. If one considers at what SO_2 the susceptibilities of blood and tissue are matched, it is conventionally

assumed to be at ~100% [17,52,192], others have estimated this value at 95% [138,193,194], while yet others have cited tissue susceptibility estimates that, based on our calculations, would result in a match at ~90% [23,195] or even ~115% [196] (i.e., tissue would be more diamagnetic than fully saturated blood, ignoring dissolved oxygen). Altogether, the quoted SO_2 offset estimates range from ~90–115%. Knowing this offset has important implications for quantitative techniques such as susceptibility-based SO_2 estimation methods and gas-free fMRI calibration but also for explaining – at least in part – regional differences in the BOLD signal itself. One promising way of exploring this issue is to perform quantitative susceptibility mapping (QSM) under conditions that can tease apart the susceptibility contributions to a voxel from blood and from parenchyma [197]. Since QSM acquisition protocols are on the order of 5 minutes for high resolution, whole brain coverage, using an endogenous contrast agent such as deoxyHb with a hyperoxic challenge could be ideal for this since levels of hyperoxia can easily be maintained over this duration of time.

Obvious next steps for the closed-form solution to the weak field approximation are to test its validity for fitting transverse signal decay experimentally and incorporate it into simulations as a model for intravascular signal decay. The former could be accomplished by fitting CPMG data from ex vivo blood samples to the closed-form solution and comparing the model fits to those obtained from fitting the relaxation rates to the WFA model of ΔR_2. The model's performance could then be examined when fitting data from non-CPMG sequences, which potentially could be used to decrease scan time. Beyond that, some of the predictions made by the simulations should be experimentally studied. This includes the prediction that r_c will decrease as the volume fraction of perturbers is increased, which could be evaluated on the umbilical cord blood data from Portnoy et al. [82]. Finally, the CFS could be incorporated into simulations as a model for intravascular signal by substituting the fitted values for G_0 and r_c from ex vivo blood data. These fits have

already been made at 1.0 T, 1.5 T, and 3 T at room temperature [76,80,81] and at 2.35 T and 7 T at 37° C [78].

Eliminating the gas challenge from calibrated fMRI is far from a settled matter. The contribution to this effort, described here, has perhaps raised more questions than it originally intended to answer. In particular, the quadratic decay term, $(R_{2,diff})^2$, needs to be more thoroughly studied experimentally. Like the measurement of T_1, T_2, or susceptibility, this should be done in a controlled manner using phantoms. By using phantoms with susceptibility inclusions, such as suspensions of polystyrene microbeads in doped water and by using beads of different radii and different concentrations of contrast agent, the magnitude of $(R_{2,diff})^2$ could be probed more systematically. If the sensitivity of the measurement technique can be made high enough, measurements of $(R_{2,diff})^2$ should be repeated in vivo under different conditions, such as under hyperoxia or hypercapnia. This would tell us how much of the $(R_{2,diff})^2$ that is measured is the result of deoxyHb in blood vs. other non-deoxyHb sources of susceptibility, and likewise for R_2'.

Besides these "new" questions, some of the original complications surrounding gas-free calibration remain. Of concern is the contribution of the other non-deoxyHb sources of susceptibility to R_2' and M (and $(R_{2,diff})^2$, perhaps). In healthy aging, the concentration of non-heme iron is known to increase in many brain regions up to early adulthood, with a much higher concentration in deep grey matter structures and relatively low concentrations in cortical GM and in white matter [198]. These trends have been corroborated in vivo using different MR-based measures such as R_2, R_2^*, R_2' and susceptibility [179,199-201], all showing varying degrees of correlation with the average iron concentrations from Hallgren and Sourander [198]. Somewhat reassuring was that the R_2' values in cortical GM from [199] were not in agreement with the linear

regression performed on the subcortical GM R_2' values vs. the literature iron concentrations of [198]. This may suggest that the R_2' of cortical GM is less affected by iron deposition over the course of healthy aging. However, this still precludes gas-free calibration studies in subcortical structures or patient groups, such as hemorrhagic stroke or neurodegenerative disorders with increased iron deposition [202].

The challenge then is to design a heme specific measure of R_2' or, alternatively and of its own utility, a measure of non-heme iron that can be incorporated into a correction factor for M. Heme specificity may be aided by an analysis of the BOLD signal changes that arise from natural fluctuations in $P_{ET}CO_2$ – without using any respiratory challenge or monitoring – which may provide subtle measures of vessel reactivity [203,204]. Non-heme specificity may be feasible with a series of diffusion-weighted acquisitions that estimate the apparent diffusion coefficient with and without accounting for local field inhomogeneities, which is claimed to be sensitive to iron deposition and not to deoxyHb [205].

7.3 Concluding Remarks

Calibrated fMRI, which was originally proposed nearly 20 years ago, is the combined result of theoretical modelling, simulations, and experimental manipulations of the BOLD signal. Over that time, it has helped shed new insights on cerebral physiology in basic neuroscience research [14,15,31,176,206-210] and in cohorts of development and aging, neurovascular and neurological disorders, and pharmacology studies [175,211-215]. At the same time, subsequent experiments and simulations have refined the model parameters with the aim of improved quantitation accuracy [13,18,20,36,67,68,177,216].

This thesis has examined multiple aspects of the underlying theories that contribute to our understanding of the biophysics of the BOLD signal. While this may have seemed like a disparate selection of topics, they are all closely connected: the susceptibility of blood is a cornerstone of BOLD imaging; transverse relaxation of blood is fundamentally dependent on the susceptibility difference between red blood cells and plasma; diffusion of water molecules around red blood cells and around blood vessels impact the signal decay observed from tissue; and calibrating the BOLD signal to obtain quantitative estimates of oxygen metabolism is dependent on all these, whether with hypercapnia, hyperoxia, or without gases. The developed biophysical signal tools and their corresponding measurements will provide improved accuracy for quantitative signal modelling with broad applications in microvascular and intravascular imaging and with specific applications in basic and clinical cerebrovascular physiology.

Appendix A

Macroscopic Inhomogeneity-Induced Dephasing

THIS chapter describes the efforts to make the asymmetric spin echo (ASE) based measurements of the fMRI calibration constant less sensitive to macroscopic field inhomogeneities. This included using a simulated slice profile to calculate the signal attenuation from through-plane inhomogeneities and determining a threshold for in-plane field gradients.

A.1 Through-Plane Dephasing

In the presence of macroscopic field inhomogeneities, the MR signal will generally be scaled by an attenuation factor, F, that is dependent on the magnitude of the inhomogeneities and the total time of dephasing, τ. The measured signal magnitude, S_{meas}, will be related to the true signal, S, by

$$S_{meas} = |S \cdot F(\tau)|\,, \tag{A.1}$$

such that the magnitude of S can be recovered from S_{meas} if F is known. In the case of asymmetric spin echo imaging, this τ and the asymmetric spin echo offset correspond to the same value.

F is frequently estimated by assuming that the field inhomogeneities can be described by linear gradients across the voxel and that only the gradient across the slice-direction, G_s, need be considered [1]. It is often further assumed that the slice profile along the slice direction is a boxcar function with a width Δz. In this case, F is given by

$$F(G_s, \tau) = sinc(\gamma G_s \tau \Delta z / 2\pi)\,. \tag{A.2}$$

In practice, an ideal square slice profile is difficult to achieve. If the slice profile is instead described by the complex function $h(z)$, then F can be modelled by

$$F(G_s, \tau) = \int_{-\infty}^{\infty} dz\; h(z) e^{-i\gamma G_s \tau z}\,. \tag{A.3}$$

Eq. (A.3) can be applied to measured or simulated slice profiles if we assume that $h(z)$ is constant over discrete intervals of width δz, each centred on z_i and denoted by h_{z_i}, in which case

$$F(G_s, \tau) = \sum_{z_i} \left(h_{z_i} \int_{z_i - \frac{\delta z}{2}}^{z_i + \frac{\delta z}{2}} dz\; e^{-i\gamma G_s \tau z} \right). \tag{A.4}$$

Solving the integral in Eq. (A.4) and normalizing it such that $F = 1$ when $G_s = 0$ or $\tau = 0$ gives

$$\begin{aligned} F(G_s, \tau) &= \frac{1}{\sum_{z_i} h_{z_i}} \sum_{z_i} \left[h_{z_i} e^{-i\delta\omega\tau} sinc(\Delta f \tau) \right] \\ &\cong \frac{1}{\sum_{z_i} h_{z_i}} \sum_{z_i} \left[h_{z_i} e^{-i\delta\omega\tau} \right], \end{aligned} \tag{A.5}$$

where $\delta\omega = \gamma G_s z_i$ and $\Delta f = \gamma G_s \delta z / 2\pi$. The approximation $sinc(\Delta f \tau) \approx 1$ that was applied holds if the discretization size, δz, is sufficiently small. In the end, Eq. (A.5) is precisely what one might expect the normalized and discretized version of Eq. (A.3) to be.

Figure A.1 shows a comparison of the attenuation factor from Eq. (A.5) with the sinc attenuation factor when $h(z)$ is a boxcar function of width 2 mm. $h(z)$ was discretized in steps δz = 2 μm and the agreement between to two attenuation factors is excellent.

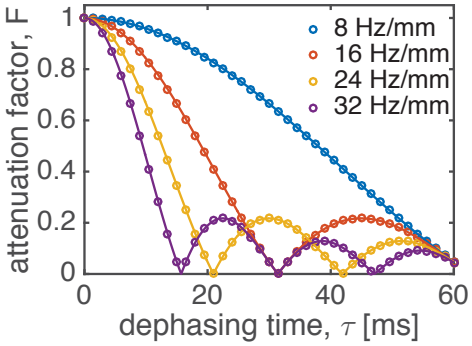

Figure A.1: Sinc attenuation factor vs. discretized attenuation factor.

The attenuation factor from Eq. (A.5) (circle markers) compared to the sinc attenuation factor of Eq. (A.2) (solid lines) for a 2.0-mm square slice profile. Each colour represents a different through-plane gradient magnitude, $\gamma G_s / 2\pi$. These through-plane gradients are on the extreme end of what is observed in areas of significant field inhomogeneity, such as the frontal sinus region.

Next, we calculated the actual spin echo EPI slice profile in MATLAB by running a discretized Bloch simulation using the RF and gradient waveforms exported from the GE pulse programming environment. We validated the simulations against other slice profile simulations using SpinBench (www.spinbench.com) and against measurements in a uniform phantom. To measure the slice profiles in the phantom, the slice select gradient was moved from the slice select

z-gradient board to the readout x-gradient board. The two simulators and the measured slice profiles were all in excellent agreement (results not shown).

Finally, Figure A.2 shows a comparison of the attenuation factor from Eq. (A.5) with the sinc attenuation factor when $h(z)$ is the simulated 2.0-mm slice profile discretized in 2-μm steps. Both positive and negative polarities of through-plane gradients were tested and gave slightly different results due to slice profile asymmetry. The attenuation factors from both polarities were in excellent agreement with the sinc attenuation factor up to the first zero. For this reason and for simplicity, we opted to use the sinc attenuation factor to correct for through-plane dephasing. Beyond the first zero, the attenuation factors from the two polarities did diverge; however, this was not of major significance for this study since only voxels where the sinc attenuation factor was ≥ 0.5 were retained for analysis and this threshold is not met beyond the first zero of the sinc function. This same result was used for the FLAIR-ASE images based on the simulated inversion pulse slice profile, which was reasonably flat across the slice width.

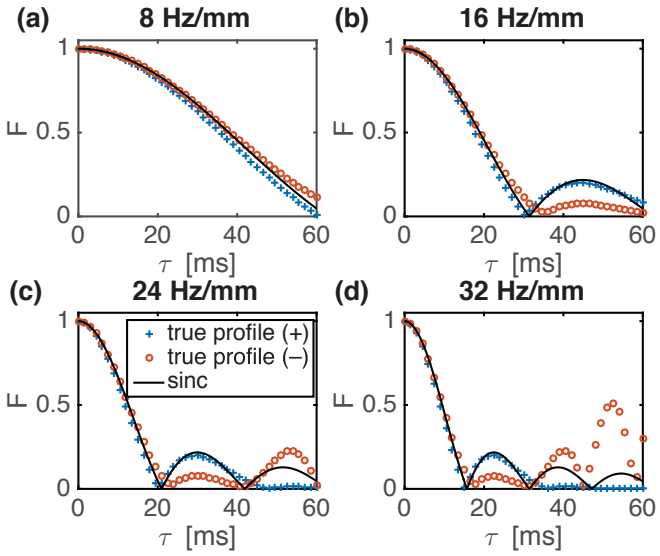

Figure A.2: The attenuation factors for the simulated slice profile.

The attenuation factor from Eq. (A.5) compared to the sinc attenuation factor of Eq. (A.2) for the simulated 2.0-mm slice profile. The discretized attenuation factors were calculated using through-plane gradients that were positive ('+' markers) or negative ('o' markers). The magnitudes of the gradients are 8 Hz/mm (a), 16 Hz/mm (b), 24 Hz/mm (c), and 32 Hz/mm (d). The sinc function is shown with the solid line.

A.2 In-Plane Dephasing

An effect of macroscopic in-plane gradients is to push the EPI echoes further away from the centre of *k*-space; beyond a critical gradient level, the echoes will be pushed out of the *k*-space acquisition window, resulting in an abrupt loss of signal. The critical gradient in the readout direction, $G_{r,c}$, is given by [174]

$$G_{r,c} = \frac{\pi}{\gamma \tau \Delta x} = 168\ \mu T\ m^{-1}, \tag{A.6}$$

where $\Delta x = 2.33$ mm is the resolution along the readout direction. The critical gradient in the phase encode direction, $G_{p,c}$, is given by [173]

$$G_{p,c} = \frac{2\pi}{2\gamma\tau\Delta y + \Delta t\ FOV_y} = 112\ \mu T\ m^{-1}, \quad \text{(A.7)}$$

where Δy = 2.33 mm is the resolution along the phase encode direction, Δt = 310 μs is the spacing between EPI echoes (accounting for parallel acceleration), and FOV_y = 224 mm is the field of view across the phase encode direction. Only voxels whose absolute in-plane gradients were less than 50% of $G_{r,c}$ and $G_{p,c}$ along the respective directions were included for analysis (i.e. $|G_r| < 84$ μT m^{-1} and $|G_p| < 56$ μT m^{-1}) .

Appendix B

Ethics Approval for Human Studies

The human studies in this project were approved by the Conjoint Health Research Ethics Board of the University of Calgary. The following document is the notice of approval.

UNIVERSITY OF CALGARY

Conjoint Health Research Ethics Board
Research Services Office
3rd Floor MacKimmie Library Tower (MLT 300)
2500 University Drive, NW
Calgary AB T2N 1N4
Telephone: (403) 220-7990
chreb@ucalgary.ca

CERTIFICATION OF INSTITUTIONAL ETHICS APPROVAL

Ethics approval for the following research has been renewed by the Conjoint Health Research Ethics Board (CHREB) at the University of Calgary. The CHREB is constituted and operates in compliance with the *Tri-Council Policy Statement: Ethical Conduct for Research Involving Humans* (TCPS 2); Health Canada Food and Drug Regulations Division 5; Part C; ICH Guidance E6: Good Clinical Practice and the provisions and regulations of the Health Information Act, RSA 2000 c H-5.

Ethics ID:	REB13-1299_REN2
Principal Investigator:	G. Bruce Pike
Co-Investigator(s):	Bradley Gordon Goodyear Marc Poulin Eric Smith
Student Co-Investigator(s):	Jaimie Bird Erin Mazerolle
Study Title:	Functional MRI of Brain Physiology
Sponsor (if applicable):	Canadian Institutes of Health Research

Effective: March 7, 2016 **Expires:** March 7, 2017

Restrictions:

This Certification is subject to the following conditions:

1. Approval is granted only for the research and purposes described in the application.
2. Any modification to the approved research must be submitted to the CHREB for approval.
3. An annual application for renewal of ethics certification must be submitted and approved by the above expiry date.
4. A closure request must be sent to the CHREB when the research is complete or terminated.

Approved By: **Date:**

Stacey A. Page, PhD, Chair , CHREB February 23, 2016

References

[1] Yablonskiy DA. Quantitation of intrinsic magnetic susceptibility-related effects in a tissue matrix. Phantom study. *Magn Reson Med* 1998;39(3):417-428.

[2] Wang Y, Liu T. Quantitative susceptibility mapping (QSM): Decoding MRI data for a tissue magnetic biomarker. *Magn Reson Med* 2014.

[3] Bloembergen N, Purcell EM, Pound RV. Relaxation Effects in Nuclear Magnetic Resonance Absorption. *Physical Review* 1948;73(7):679-712.

[4] Fuchs VR, Sox HC, Jr. Physicians' views of the relative importance of thirty medical innovations. *Health affairs* 2001;20(5):30-42.

[5] Yablonskiy DA, Haacke EM. Theory of NMR signal behavior in magnetically inhomogeneous tissues: the static dephasing regime. *Magn Reson Med* 1994;32(6):749-763.

[6] Ogawa S, Tank DW, Menon R, Ellermann JM, Kim SG, Merkle H, Ugurbil K. Intrinsic signal changes accompanying sensory stimulation: functional brain mapping with magnetic resonance imaging. *Proceedings of the National Academy of Sciences of the United States of America* 1992;89(13):5951-5955.

[7] Kwong KK, Belliveau JW, Chesler DA, Goldberg IE, Weisskoff RM, Poncelet BP, Kennedy DN, Hoppel BE, Cohen MS, Turner R, et al. Dynamic magnetic resonance imaging of human brain activity during primary sensory stimulation. *Proceedings of the National Academy of Sciences of the United States of America* 1992;89(12):5675-5679.

[8] Bandettini PA, Wong EC, Hinks RS, Tikofsky RS, Hyde JS. Time course EPI of human brain function during task activation. *Magn Reson Med* 1992;25(2):390-397.

[9] Donahue MJ, Hoogduin H, van Zijl PC, Jezzard P, Luijten PR, Hendrikse J. Blood oxygenation level-dependent (BOLD) total and extravascular signal changes and DeltaR2* in human visual cortex at 1.5, 3.0 and 7.0 T. *NMR Biomed* 2011;24(1):25-34.

[10] Boxerman JL, Bandettini PA, Kwong KK, Baker JR, Davis TL, Rosen BR, Weisskoff RM. The intravascular contribution to fMRI signal change: Monte Carlo modeling and diffusion-weighted studies in vivo. *Magn Reson Med* 1995;34(1):4-10.

[11] Ogawa S, Lee TM, Nayak AS, Glynn P. Oxygenation-sensitive contrast in magnetic resonance image of rodent brain at high magnetic fields. *Magn Reson Med* 1990;14(1):68-78.

[12] Fox PT, Raichle ME, Mintun MA, Dence C. Nonoxidative glucose consumption during focal physiologic neural activity. *Science* 1988;241(4864):462-464.

[13] Chen JJ, Pike GB. BOLD-specific cerebral blood volume and blood flow changes during neuronal activation in humans. *NMR Biomed* 2009;22(10):1054-1062.

[14] Hoge RD, Atkinson J, Gill B, Crelier GR, Marrett S, Pike GB. Investigation of BOLD signal dependence on cerebral blood flow and oxygen consumption: the deoxyhemoglobin dilution model. *Magn Reson Med* 1999;42(5):849-863.

[15] Davis TL, Kwong KK, Weisskoff RM, Rosen BR. Calibrated functional MRI: mapping the dynamics of oxidative metabolism. *Proceedings of the National Academy of Sciences of the United States of America* 1998;95(4):1834-1839.

[16] Hoge RD. Calibrated FMRI. *Neuroimage* 2012;62(2):930-937.

[17] Boxerman JL, Hamberg LM, Rosen BR, Weisskoff RM. MR Contrast Due to Intravascular Magnetic-Susceptibility Perturbations. *Magn Reson Med* 1995;34(4):555-566.

[18] Griffeth VE, Buxton RB. A theoretical framework for estimating cerebral oxygen metabolism changes using the calibrated-BOLD method: modeling the effects of blood volume distribution, hematocrit, oxygen extraction fraction, and tissue signal properties on the BOLD signal. *Neuroimage* 2011;58(1):198-212.

[19] Gagnon L, Sakadzic S, Lesage F, Musacchia JJ, Lefebvre J, Fang Q, Yucel MA, Evans KC, Mandeville ET, Cohen-Adad J, Polimeni JR, Yaseen MA, Lo EH, Greve DN, Buxton RB, Dale AM, Devor A, Boas DA. Quantifying the Microvascular Origin of BOLD-fMRI from First Principles with Two-Photon Microscopy and an Oxygen-Sensitive Nanoprobe. *The Journal of neuroscience : the official journal of the Society for Neuroscience* 2015;35(8):3663-3675.

[20] Gagnon L, Sakadzic S, Lesage F, Pouliot P, Dale AM, Devor A, Buxton RB, Boas DA. Validation and optimization of hypercapnic-calibrated fMRI from oxygen-sensitive two-photon microscopy. *Philosophical transactions of the Royal Society of London Series B, Biological sciences* 2016;371(1705).

[21] Chiarelli PA, Bulte DP, Wise R, Gallichan D, Jezzard P. A calibration method for quantitative BOLD fMRI based on hyperoxia. *Neuroimage* 2007;37(3):808-820.

[22] Mark CI, Fisher JA, Pike GB. Improved fMRI calibration: precisely controlled hyperoxic versus hypercapnic stimuli. *Neuroimage* 2011;54(2):1102-1111.

[23] Schwarzbauer C, Deichmann R. Vascular component analysis of hyperoxic and hypercapnic BOLD contrast. *Neuroimage* 2012;59(3):2401-2412.

[24] Kida I, Kennan RP, Rothman DL, Behar KL, Hyder F. High-resolution CMR(O2) mapping in rat cortex: a multiparametric approach to calibration of BOLD image contrast at 7 Tesla. *J Cereb Blood Flow Metab* 2000;20(5):847-860.

[25] Fujita N, Matsumoto K, Tanaka H, Watanabe Y, Murase K. Quantitative study of changes in oxidative metabolism during visual stimulation using absolute relaxation rates. *NMR Biomed* 2006;19(1):60-68.

[26] Blockley NP, Griffeth VE, Buxton RB. A general analysis of calibrated BOLD methodology for measuring CMRO2 responses: comparison of a new approach with existing methods. *Neuroimage* 2012;60(1):279-289.

[27] Blockley NP, Griffeth VE, Simon AB, Dubowitz DJ, Buxton RB. Calibrating the BOLD response without administering gases: comparison of hypercapnia calibration with calibration using an asymmetric spin echo. *Neuroimage* 2015;104:423-429.

[28] Shu CY, Herman P, Coman D, Sanganahalli BG, Wang H, Juchem C, Rothman DL, de Graaf RA, Hyder F. Brain region and activity-dependent properties of M for calibrated fMRI. *Neuroimage* 2015;125:848-856.

[29] Purves D. *Neuroscience*. Sunderland, Mass.: Sinauer; 2008. xvii, 857, G-816, IC-857, I-829 p. p.

[30] Buxton RB. Chapter 1: Neural activity and energy metabolism. *Introduction to functional magnetic resonance imaging : principles and techniques.* 2nd ed. Cambridge ; New York: Cambridge University Press; 2009.

[31] Lin AL, Fox PT, Hardies J, Duong TQ, Gao JH. Nonlinear coupling between cerebral blood flow, oxygen consumption, and ATP production in human visual cortex. *Proceedings of the National Academy of Sciences of the United States of America* 2010;107(18):8446-8451.

[32] Severinghaus JW. Simple, accurate equations for human blood O2 dissociation computations. *Journal of applied physiology* 1979;46(3):599-602.

[33] Pittman RN. In: Granger DN, Granger JP, editors. *Regulation of Tissue Oxygenation*, Colloquium Series on Integrated Systems Physiology: From Molecule to Function to Disease. San Rafael (CA): Morgan & Claypool Life Sciences; 2009-2011.

[34] Ito H, Kanno I, Kato C, Sasaki T, Ishii K, Ouchi Y, Iida A, Okazawa H, Hayashida K, Tsuyuguchi N, Ishii K, Kuwabara Y, Senda M. Database of normal human cerebral blood flow, cerebral blood volume, cerebral oxygen extraction fraction and cerebral metabolic

rate of oxygen measured by positron emission tomography with 15O-labelled carbon dioxide or water, carbon monoxide and oxygen: a multicentre study in Japan. *European journal of nuclear medicine and molecular imaging* 2004;31(5):635-643.

[35] Gauthier CJ, Desjardins-Crepeau L, Madjar C, Bherer L, Hoge RD. Absolute quantification of resting oxygen metabolism and metabolic reactivity during functional activation using QUO2 MRI. *Neuroimage* 2012;63(3):1353-1363.

[36] Bulte DP, Kelly M, Germuska M, Xie J, Chappell MA, Okell TW, Bright MG, Jezzard P. Quantitative measurement of cerebral physiology using respiratory-calibrated MRI. *Neuroimage* 2012;60(1):582-591.

[37] Raichle ME, MacLeod AM, Snyder AZ, Powers WJ, Gusnard DA, Shulman GL. A default mode of brain function. *Proceedings of the National Academy of Sciences of the United States of America* 2001;98(2):676-682.

[38] MacDonald ME, Frayne R. Cerebrovascular MRI: a review of state-of-the-art approaches, methods and techniques. *NMR Biomed* 2015;28(7):767-791.

[39] Cipolla MJ. The cerebral circulation. Integrated systems physiology : from molecule to function #2. San Rafael, Calif.: Morgan & Claypool Life Sciences,; 2010. p 1 online resource (x, 59 p.) ill.

[40] Sakadzic S, Mandeville ET, Gagnon L, Musacchia JJ, Yaseen MA, Yucel MA, Lefebvre J, Lesage F, Dale AM, Eikermann-Haerter K, Ayata C, Srinivasan VJ, Lo EH, Devor A, Boas DA. Large arteriolar component of oxygen delivery implies a safe margin of oxygen supply to cerebral tissue. *Nat Commun* 2014;5:5734.

[41] Weber B. Chapter 5: Neurovascular Coupling. In: Uludag K, Ugurbil K, Berliner L, editors. *fMRI: From Nuclear Spins to Brain Functions.* 1st ed, Biological Magnetic Resonance. New York: Springer US; 2015. p 72–73.

[42] Duvernoy HM, Delon S, Vannson JL. Cortical blood vessels of the human brain. *Brain research bulletin* 1981;7(5):519-579.

[43] Weber B, Keller AL, Reichold J, Logothetis NK. The microvascular system of the striate and extrastriate visual cortex of the macaque. *Cerebral cortex* 2008;18(10):2318-2330.

[44] Buxton RB. Chapter 2: Cerebral blood flow and brain activation. *Introduction to functional magnetic resonance imaging : principles and techniques.* 2nd ed. Cambridge ; New York: Cambridge University Press; 2009.

[45] van Zijl PC, Eleff SM, Ulatowski JA, Oja JM, Ulug AM, Traystman RJ, Kauppinen RA. Quantitative assessment of blood flow, blood volume and blood oxygenation effects in functional magnetic resonance imaging. *Nature medicine* 1998;4(2):159-167.

[46] Lauwers F, Cassot F, Lauwers-Cances V, Puwanarajah P, Duvernoy H. Morphometry of the human cerebral cortex microcirculation: general characteristics and space-related profiles. *Neuroimage* 2008;39(3):936-948.

[47] Pawlik G, Rackl A, Bing RJ. Quantitative capillary topography and blood flow in the cerebral cortex of cats: an in vivo microscopic study. *Brain research* 1981;208(1):35-58.

[48] Stefanovic B, Hutchinson E, Yakovleva V, Schram V, Russell JT, Belluscio L, Koretsky AP, Silva AC. Functional reactivity of cerebral capillaries. *J Cereb Blood Flow Metab* 2008;28(5):961-972.

[49] Germuska MA, Meakin JA, Bulte DP. The influence of noise on BOLD-mediated vessel size imaging analysis methods. *J Cereb Blood Flow Metab* 2013;33(12):1857-1863.

[50] Pauling L, Coryell CD. The Magnetic Properties and Structure of Hemoglobin, Oxyhemoglobin and Carbonmonoxyhemoglobin. *Proceedings of the National Academy of Sciences of the United States of America* 1936;22(4):210-216.

[51] Weisskoff RM, Kiihne S. MRI susceptometry: image-based measurement of absolute susceptibility of MR contrast agents and human blood. *Magn Reson Med* 1992;24(2):375-383.

[52] Ogawa S, Menon RS, Tank DW, Kim SG, Merkle H, Ellermann JM, Ugurbil K. Functional brain mapping by blood oxygenation level-dependent contrast magnetic resonance imaging. A comparison of signal characteristics with a biophysical model. *Biophysical journal* 1993;64(3):803-812.

[53] Bandettini PA, Wong EC. Effects of biophysical and physiologic parameters on brain activation-induced R2* and R2 changes: Simulations using a deterministic diffusion model. *Int J Imaging Syst Technol* 1995;6:133-152.

[54] Weisskoff RM, Zuo CS, Boxerman JL, Rosen BR. Microscopic susceptibility variation and transverse relaxation: theory and experiment. *Magn Reson Med* 1994;31(6):601-610.

[55] Kennan RP, Zhong J, Gore JC. Intravascular susceptibility contrast mechanisms in tissues. *Magn Reson Med* 1994;31(1):9-21.

[56] Einstein A. *Investigations on the theory of the Brownian movement*. Cowper AD, translator. New York: Dover Publications; 1956. 119 p. p.

[57] Le Bihan D, Turner R, Patronas N. Chapter 8: Diffusion MR imaging in normal brain and in brain tumors. In: Le Bihan D, editor. *Diffusion and perfusion magnetic resonance imaging applications to functional MRI*. New York: Raven Press; 1995. p xxi, 374 p.

[58] Ni JM, Chen S, Liu JJ, Huang G, Shen TZ, Chen XR. Regional diffusion changes of cerebral grey matter during normal aging--a fluid-inversion prepared diffusion imaging study. *European journal of radiology* 2010;75(2):134-138.

[59] Fox RJ, Sakaie K, Lee JC, Debbins JP, Liu Y, Arnold DL, Melhem ER, Smith CH, Philips MD, Lowe M, Fisher E. A validation study of multicenter diffusion tensor imaging: reliability of fractional anisotropy and diffusivity values. *AJNR American journal of neuroradiology* 2012;33(4):695-700.

[60] Gillis P, Koenig SH. Transverse relaxation of solvent protons induced by magnetized spheres: application to ferritin, erythrocytes, and magnetite. *Magn Reson Med* 1987;5(4):323-345.

[61] Zhao F, Wang P, Kim SG. Cortical depth-dependent gradient-echo and spin-echo BOLD fMRI at 9.4T. *Magn Reson Med* 2004;51(3):518-524.

[62] Goense JB, Logothetis NK. Laminar specificity in monkey V1 using high-resolution SE-fMRI. *Magnetic resonance imaging* 2006;24(4):381-392.

[63] Shu CY, Sanganahalli BG, Coman D, Herman P, Rothman DL, Hyder F. Quantitative beta mapping for calibrated fMRI. *Neuroimage* 2016;126:219-228.

[64] Berman AJ, Pike GB. Breaking beta: Understanding the beta-value in calibrated fMRI. 2016; Singapore. p 506.

[65] Croal PL, Driver ID, Francis ST, Gowland PA. Field strength dependence of grey matter R2* on venous oxygenation. *Neuroimage* 2017;146:327-332.

[66] Grubb RL, Jr., Raichle ME, Eichling JO, Ter-Pogossian MM. The effects of changes in PaCO2 on cerebral blood volume, blood flow, and vascular mean transit time. *Stroke; a journal of cerebral circulation* 1974;5(5):630-639.

[67] Chen JJ, Pike GB. MRI measurement of the BOLD-specific flow-volume relationship during hypercapnia and hypocapnia in humans. *Neuroimage* 2010;53(2):383-391.

[68] Gauthier CJ, Hoge RD. Magnetic resonance imaging of resting OEF and CMRO(2) using a generalized calibration model for hypercapnia and hyperoxia. *Neuroimage* 2012;60(2):1212-1225.

[69] Ma J, Wehrli FW. Method for image-based measurement of the reversible and irreversible contribution to the transverse-relaxation rate. *Journal of magnetic resonance Series B* 1996;111(1):61-69.

[70] Martindale J, Kennerley AJ, Johnston D, Zheng Y, Mayhew JE. Theory and generalization of Monte Carlo models of the BOLD signal source. *Magn Reson Med* 2008;59(3):607-618.

[71] Klassen LM, Menon RS. NMR simulation analysis of statistical effects on quantifying cerebrovascular parameters. *Biophysical journal* 2007;92(3):1014-1021.

[72] Christen T, Lemasson B, Pannetier N, Farion R, Segebarth C, Remy C, Barbier EL. Evaluation of a quantitative blood oxygenation level-dependent (qBOLD) approach to map local blood oxygen saturation. *NMR Biomed* 2010;24:393-403.

[73] Pannetier NA, Debacker CS, Mauconduit F, Christen T, Barbier EL. A simulation tool for dynamic contrast enhanced MRI. *PloS one* 2013;8(3):e57636.

[74] Yablonskiy DA, Sukstanskii AL, He X. Blood oxygenation level-dependent (BOLD)-based techniques for the quantification of brain hemodynamic and metabolic properties - theoretical models and experimental approaches. *NMR Biomed* 2013;26(8):963-986.

[75] Luz Z, Meiboom S. Nuclear Magnetic Resonance Study of Protolysis of Trimethylammonium Ion in Aqueous Solution - Order of Reaction with Respect to Solvent. *J Chem Phys* 1963;39(2):366-&.

[76] Jensen JH, Chandra R. NMR relaxation in tissues with weak magnetic inhomogeneities. *Magn Reson Med* 2000;44(1):144-156.

[77] Cokelet GR, Meiselman HJ. Macro- and Micro-Rheological Properties of Blood. In: Baskurt OK, Hardeman MR, Rampling MW, Meiselman HJ, editors. *Handbook of hemorheology and hemodynamics*. Amsterdam ; Washington, DC: IOS Press; 2007. p x, 455 p.

[78] Gardener AG, Francis ST, Prior M, Peters A, Gowland PA. Dependence of blood R2 relaxivity on CPMG echo-spacing at 2.35 and 7 T. *Magn Reson Med* 2010;64(4):967-974.

[79] Kiselev VG, Novikov DS. Transverse NMR relaxation as a probe of mesoscopic structure. *Physical review letters* 2002;89(27).

[80] Stefanovic B, Pike GB. Human whole-blood relaxometry at 1.5 T: Assessment of diffusion and exchange models. *Magn Reson Med* 2004;52(4):716-723.

[81] Chen JJ, Pike GB. Human whole blood T2 relaxometry at 3 Tesla. *Magn Reson Med* 2009;61(2):249-254.

[82] Portnoy S, Osmond M, Zhu MY, Seed M, Sled JG, Macgowan CK. Relaxation properties of human umbilical cord blood at 1.5 Tesla. *Magn Reson Med* 2017;77(4):1678-1690.

[83] Bandettini PA, Wong EC. Effects of Biophysical and Physiological-Parameters on Brain Activation-Induced R(2)Asterisk and R(2) Changes - Simulations Using a Deterministic Diffusion-Model. *Int J Imag Syst Tech* 1995;6(2-3):133-152.

[84] Fisel CR, Ackerman JL, Buxton RB, Garrido L, Belliveau JW, Rosen BR, Brady TJ. MR contrast due to microscopically heterogeneous magnetic susceptibility: numerical simulations and applications to cerebral physiology. *Magn Reson Med* 1991;17(2):336-347.

[85] Marques JP, Bowtell R. Application of a fourier-based method for rapid calculation of field inhomogeneity due to spatial variation of magnetic susceptibility. *Concept Magn Reson B* 2005;25B(1):65-78.

[86] Cheng YC, Neelavalli J, Haacke EM. Limitations of calculating field distributions and magnetic susceptibilities in MRI using a Fourier based method. *Physics in medicine and biology* 2009;54(5):1169-1189.

[87] Salomir R, De Senneville BD, Moonen CTW. A fast calculation method for magnetic field inhomogeneity due to an arbitrary distribution of bulk susceptibility. *Concept Magn Reson B* 2003;19B(1):26-34.

[88] Miller KL, Jezzard P. Modeling SSFP functional MRI contrast in the brain. *Magn Reson Med* 2008;60(3):661-673.

[89] Ross S. Chapter 10: Simulation. *A First Course in Probability*. 7th ed. Upper Saddle River, New Jersey: Pearson Prentice Hall; 2006.

[90] Pflugfelder D, Vahedipour K, Uludag K, Shah NJ, Stocker T. On the numerically predicted spatial BOLD fMRI specificity for spin echo sequences. *Magnetic resonance imaging* 2011;29(9):1195-1204.

[91] Christen T, Schmiedeskamp H, Straka M, Bammer R, Zaharchuk G. Measuring brain oxygenation in humans using a multiparametric quantitative blood oxygenation level dependent MRI approach. *Magn Reson Med* 2011.

[92] Lindeberg T. Scale-Space for Discrete Signals. *Ieee T Pattern Anal* 1990;12(3):234-254.

[93] Oppenheim AV, Schafer RW. *Digital Signal Processing*. Englewood Cliffs, NJ: Prentice-Hall, Inc.; 1975. 533-539 p.

[94] Christen T, Zaharchuk G, Pannetier N, Serduc R, Joudiou N, Vial JC, Remy C, Barbier EL. Quantitative MR estimates of blood oxygenation based on T(2) *: A numerical study of the impact of model assumptions. *Magn Reson Med* 2012;67(5):1458-1468.

[95] Pannetier NA, Sohlin M, Christen T, Schad L, Schuff N. Numerical modeling of susceptibility-related MR signal dephasing with vessel size measurement: Phantom validation at 3T. *Magn Reson Med* 2014;72(3):646-658.

[96] Young IR, Clarke GJ, Bailes DR, Pennock JM, Doyle FH, Bydder GM. Enhancement of relaxation rate with paramagnetic contrast agents in NMR imaging. *The Journal of computed tomography* 1981;5(6):543-547.

[97] Tadamura E, Hatabu H, Li W, Prasad PV, Edelman RR. Effect of oxygen inhalation on relaxation times in various tissues. *J Magn Reson Imaging* 1997;7(1):220-225.

[98] Zaharchuk G, Busse RF, Rosenthal G, Manley GT, Glenn OA, Dillon WP. Noninvasive oxygen partial pressure measurement of human body fluids in vivo using magnetic resonance imaging. *Acad Radiol* 2006;13(8):1016-1024.

[99] Matsumoto K, Bernardo M, Subramanian S, Choyke P, Mitchell JB, Krishna MC, Lizak MJ. MR assessment of changes of tumor in response to hyperbaric oxygen treatment. *Magn Reson Med* 2006;56(2):240-246.

[100] O'Connor JP, Naish JH, Jackson A, Waterton JC, Watson Y, Cheung S, Buckley DL, McGrath DM, Buonaccorsi GA, Mills SJ, Roberts C, Jayson GC, Parker GJ. Comparison of normal tissue R1 and R*2 modulation by oxygen and carbogen. *Magn Reson Med* 2009;61(1):75-83.

[101] Haddock B, Larsson HB, Hansen AE, Rostrup E. Measurement of brain oxygenation changes using dynamic T(1)-weighted imaging. *Neuroimage* 2013;78:7-15.

[102] Magnetic susceptibility of the elements and inorganic compounds. In: Haynes WM, editor. *CRC Handbook of Chemistry and Physics.* 93rd ed. Boca Raton, FL: CRC Press/Taylor and Francis; (Internet Version 2013).

[103] Berman AJ, Ma Y, Hoge RD, Pike GB. The effect of dissolved oxygen on the susceptibility of blood. *Magn Reson Med* 2016;75(1):363-371.

[104] Reichenbach JR, Essig M, Haacke EM, Lee BC, Przetak C, Kaiser WA, Schad LR. High-resolution venography of the brain using magnetic resonance imaging. *Magma* 1998;6(1):62-69.

[105] Blockley NP, Griffeth VE, Germuska MA, Bulte DP, Buxton RB. An analysis of the use of hyperoxia for measuring venous cerebral blood volume: comparison of the existing method with a new analysis approach. *Neuroimage* 2013;72:33-40.

[106] Pilkinton DT, Gaddam SR, Reddy R. Characterization of paramagnetic effects of molecular oxygen on blood oxygenation level-dependent-modulated hyperoxic contrast studies of the human brain. *Magn Reson Med* 2011;66(3):794-801.

[107] Yeung DK, Griffith JF, Li AF, Ma HT, Yuan J. Air pressure-induced susceptibility changes in vascular reactivity studies using BOLD MRI. *J Magn Reson Imaging* 2012.

[108] Spees WM, Yablonskiy DA, Oswood MC, Ackerman JJH. Water proton MR properties of human blood at 1.5 Tesla: magnetic susceptibility, T1, T2, T2*, and non-Lorentzian signal behavior. *Magn Reson Med* 2001;45:533-542.

[109] Schenck JF. The role of magnetic susceptibility in magnetic resonance imaging: MRI magnetic compatibility of the first and second kinds. *Medical physics* 1996;23(6):815-850.

[110] van Slyke DD, Hiller A, Phillips RA, Hamilton PB, Dole VP, Archibald RM, Eder HA. The Estimation of Plasma Protein Concentration from Plasma Specific Gravity. *Journal of Biological Chemistry* 1950;183(1):331-347.

[111] Jain V, Abdulmalik O, Propert KJ, Wehrli FW. Investigating the magnetic susceptibility properties of fresh human blood for noninvasive oxygen saturation quantification. *Magn Reson Med* 2012;68(3):863-867.

[112] Roughton FJ, Severinghaus JW. Accurate determination of O2 dissociation curve of human blood above 98.7 percent saturation with data on O2 solubility in unmodified human blood from 0 degrees to 37 degrees C. *Journal of applied physiology* 1973;35(6):861-869.

[113] Robinson S, Grabner G, Witoszynskyj S, Trattnig S. Combining phase images from multi-channel RF coils using 3D phase offset maps derived from a dual-echo scan. *Magn Reson Med* 2011;65(6):1638-1648.

[114] Gudbjartsson H, Patz S. The Rician distribution of noisy MRI data. *Magn Reson Med* 1995;34(6):910-914.

[115] Langham MC, Magland JF, Floyd TF, Wehrli FW. Retrospective correction for induced magnetic field inhomogeneity in measurements of large-vessel hemoglobin oxygen saturation by MR susceptometry. *Magn Reson Med* 2009;61(3):626-633.

[116] Wapler MC, Leupold J, Dragonu I, von Elverfeld D, Zaitsev M, Wallrabe U. Magnetic properties of materials for MR engineering, micro-MR and beyond. *J Magn Reson* 2014;242(0):233-242.

[117] Langham MC, Magland JF, Epstein CL, Floyd TF, Wehrli FW. Accuracy and precision of MR blood oximetry based on the long paramagnetic cylinder approximation of large vessels. *Magn Reson Med* 2009;62(2):333-340.

[118] Li C, Langham MC, Epstein CL, Magland JF, Wu J, Gee J, Wehrli FW. Accuracy of the cylinder approximation for susceptometric measurement of intravascular oxygen saturation. *Magn Reson Med* 2012;67(3):808-813.

[119] Williamson JH. Least-Squares Fitting of a Straight Line. *Can J Phys* 1968;46(16):1845-1847.

[120] Jackson PGG, Cockcroft PD. Appendix 3: Laboratory Reference Values: Biochemistry. *Clinical Examination of Farm Animals*. Malden, MA: Wiley-Blackwell; 2002. p 303-305.

[121] May EF, Moldover MR, Schmidt JW. Electric and magnetic susceptibilities of gaseous oxygen: Present data and modern theory compared. *Phys Rev A* 2008;78(3):032522.

[122] Tsubomura H, Mulliken RS. Molecular Complexes and Their Spectra .12. Ultraviolet Absorption Spectra Caused by the Interaction of Oxygen with Organic Molecules. *Journal of the American Chemical Society* 1960;82(23):5966-5974.

[123] Solubility of selected gases in water. In: Haynes WM, editor. *CRC Handbook of Chemistry and Physics*. 93rd ed. Boca Raton, FL: CRC Press/Taylor and Francis; (Internet Version 2013).

[124] Harvey AH, Kaplan SG, Burnett JH. Effect of dissolved air on the density and refractive index of water. *Int J Thermophys* 2005;26(5):1495-1514.

[125] Philo JS, Fairbank WM. Temperature-Dependence of the Diamagnetism of Water. *J Chem Phys* 1980;72(8):4429-4433.

[126] Apelblat A, Manzurola E. Apparent Molar Volumes of Organic-Acids and Salts in Water at 298.15 K. *Fluid Phase Equilibr* 1990;60(1-2):157-171.

[127] Millero FJ. Apparent and Partial Molal Volume of Aqueous Sodium Chloride Solutions at Various Temperatures. *J Phys Chem-Us* 1970;74(2):356-362.

[128] Jensen JH, Chandra R, Ramani A, Lu H, Johnson G, Lee SP, Kaczynski K, Helpern JA. Magnetic field correlation imaging. *Magn Reson Med* 2006;55(6):1350-1361.

[129] Wehrli FW, Song HK, Saha PK, Wright AC. Quantitative MRI for the assessment of bone structure and function. *NMR Biomed* 2006;19(7):731-764.

[130] Carr HY, Purcell EM. Effects of Diffusion on Free Precession in Nuclear Magnetic Resonance Experiments. *Physical Review* 1954;94(3):630-638.

[131] Sukstanskii AL, Yablonskiy DA. Gaussian approximation in the theory of MR signal formation in the presence of structure-specific magnetic field inhomogeneities. *J Magn Reson* 2003;163(2):236-247.

[132] Thulborn KR, Waterton JC, Matthews PM, Radda GK. Oxygenation dependence of the transverse relaxation time of water protons in whole blood at high field. *Biochim Biophys Acta* 1982;714(2):265-270.

[133] Wismer GL, Buxton RB, Rosen BR, Fisel CR, Oot RF, Brady TJ, Davis KR. Susceptibility induced MR line broadening: applications to brain iron mapping. *Journal of computer assisted tomography* 1988;12(2):259-265.

[134] Yablonskiy DA, Haacke EM. An MRI method for measuring T2 in the presence of static and RF magnetic field inhomogeneities. *Magn Reson Med* 1997;37(6):872-876.

[135] Storey P, Chung S, Ben-Eliezer N, Lamberskiy G, Lui YW, Novikov DS. Signatures of microstructure in conventional gradient and spin echo signals. 2015; Toronto. 23rd International Society of Magnetic Resonance in Medicine Annual Meeting. p 14.

[136] Berman AJ, Pike GB. A general solution for transverse signal decay under the weak field approximation: theory and validation with spherical perturbers. 2016; Singapore. 24th International Society of Magnetic Resonance in Medicine Annual Meeting. p 506.

[137] Stanisz GJ, Li JG, Wright GA, Henkelman RM. Water dynamics in human blood via combined measurements of T2 relaxation and diffusion in the presence of gadolinium. *Magn Reson Med* 1998;39(2):223-233.

[138] Spees WM, Yablonskiy DA, Oswood MC, Ackerman JJ. Water proton MR properties of human blood at 1.5 Tesla: magnetic susceptibility, T(1), T(2), T*(2), and non-Lorentzian signal behavior. *Magn Reson Med* 2001;45(4):533-542.

[139] Stables LA, Kennan RP, Gore JC. Asymmetric spin-echo imaging of magnetically inhomogeneous systems: theory, experiment, and numerical studies. *Magn Reson Med* 1998;40(3):432-442.

[140] Wilson GJ, Springer CS, Jr., Bastawrous S, Maki JH. Human whole blood 1 H2 O transverse relaxation with gadolinium-based contrast reagents: Magnetic susceptibility and transmembrane water exchange. *Magn Reson Med* 2017;77(5):2015-2027.

[141] Novikov DS, Kiselev VG. Transverse NMR relaxation in magnetically heterogeneous media. *Journal of magnetic resonance* 2008;195(1):33-39.

[142] Novikov DS, Jensen JH, Helpern JA, Fieremans E. Revealing mesoscopic structural universality with diffusion. *Proceedings of the National Academy of Sciences of the United States of America* 2014;111(14):5088-5093.

[143] Gillis P, Peto S, Moiny F, Mispelter J, Cuenod CA. Proton transverse nuclear magnetic relaxation in oxidized blood: a numerical approach. *Magn Reson Med* 1995;33(1):93-100.

[144] Benga G, Borza V, Popescu O, Pop VI, Muresan A. Water exchange through erythrocyte membranes: nuclear magnetic resonance studies on resealed ghosts compared to human erythrocytes. *J Membr Biol* 1986;89(2):127-130.

[145] Ni W, Christen T, Zun Z, Zaharchuk G. Comparison of R2' measurement methods in the normal brain at 3 tesla. *Magn Reson Med* 2014.

[146] Fujita N, Shinohara M, Tanaka H, Yutani K, Nakamura H, Murase K. Quantitative mapping of cerebral deoxyhemoglobin content using MR imaging. *Neuroimage* 2003;20(4):2071-2083.

[147] Stefanovic B, Sled JG, Pike GB. Quantitative T2 in the occipital lobe: the role of the CPMG refocusing rate. *J Magn Reson Imaging* 2003;18(3):302-309.

[148] Dickson JD, Ash TW, Williams GB, Sukstanskii AL, Ansorge RE, Yablonskiy DA. Quantitative phenomenological model of the BOLD contrast mechanism. *J Magn Reson* 2011;212(1):17-25.

[149] Xu F, Uh J, Brier MR, Hart J, Jr., Yezhuvath US, Gu H, Yang Y, Lu H. The influence of carbon dioxide on brain activity and metabolism in conscious humans. *J Cereb Blood Flow Metab* 2011;31(1):58-67.

[150] Hall EL, Driver ID, Croal PL, Francis ST, Gowland PA, Morris PG, Brookes MJ. The effect of hypercapnia on resting and stimulus induced MEG signals. *Neuroimage* 2011;58(4):1034-1043.

[151] Bulte DP, Drescher K, Jezzard P. Comparison of hypercapnia-based calibration techniques for measurement of cerebral oxygen metabolism with MRI. *Magn Reson Med* 2009;61(2):391-398.

[152] Chen JJ, Pike GB. Global cerebral oxidative metabolism during hypercapnia and hypocapnia in humans: implications for BOLD fMRI. *J Cereb Blood Flow Metab* 2010;30(6):1094-1099.

[153] Croal PL, Hall EL, Driver ID, Brookes MJ, Gowland PA, Francis ST. The effect of isocapnic hyperoxia on neurophysiology as measured with MRI and MEG. *Neuroimage* 2015;105:323-331.

[154] Bulte DP, Chiarelli PA, Wise RG, Jezzard P. Cerebral perfusion response to hyperoxia. *J Cereb Blood Flow Metab* 2007;27(1):69-75.

[155] Blockley NP, Stone AJ. Improving the specificity of R2' to the deoxyhaemoglobin content of brain tissue: Prospective correction of macroscopic magnetic field gradients. *Neuroimage* 2016;135:253-260.

[156] Simon AB, Dubowitz DJ, Blockley NP, Buxton RB. A novel Bayesian approach to accounting for uncertainty in fMRI-derived estimates of cerebral oxygen metabolism fluctuations. *Neuroimage* 2016;129:198-213.

[157] Stone AJ, Blockley NP. A streamlined acquisition for mapping baseline brain oxygenation using quantitative BOLD. *Neuroimage* 2016;147:79-88.

[158] He X, Yablonskiy DA. Quantitative BOLD: mapping of human cerebral deoxygenated blood volume and oxygen extraction fraction: default state. *Magn Reson Med* 2007;57(1):115-126.

[159] Gauthier CJ, Madjar C, Tancredi FB, Stefanovic B, Hoge RD. Elimination of visually evoked BOLD responses during carbogen inhalation: implications for calibrated MRI. *Neuroimage* 2011;54(2):1001-1011.

[160] Krieger SN, Ivanov D, Huber L, Roggenhofer E, Sehm B, Turner R, Egan GF, Gauthier CJ. Using carbogen for calibrated fMRI at 7Tesla: comparison of direct and modelled estimation of the M parameter. *Neuroimage* 2014;84:605-614.

[161] An H, Lin W. Impact of intravascular signal on quantitative measures of cerebral oxygen extraction and blood volume under normo- and hypercapnic conditions using an asymmetric spin echo approach. *Magn Reson Med* 2003;50(4):708-716.

[162] Mugler JP, 3rd, Brookeman JR. Three-dimensional magnetization-prepared rapid gradient-echo imaging (3D MP RAGE). *Magn Reson Med* 1990;15(1):152-157.

[163] Tancredi FB, Lajoie I, Hoge RD. A simple breathing circuit allowing precise control of inspiratory gases for experimental respiratory manipulations. *BMC Res Notes* 2014;7:235.

[164] Jenkinson M, Beckmann CF, Behrens TE, Woolrich MW, Smith SM. Fsl. *Neuroimage* 2012;62(2):782-790.

[165] Smith SM. Fast robust automated brain extraction. *Human brain mapping* 2002;17(3):143-155.

[166] Jezzard P, Balaban RS. Correction for geometric distortion in echo planar images from B0 field variations. *Magnetic Resonance in Medicine* 1995;34(1):65-73.

[167] Liu T, Wisnieff C, Lou M, Chen W, Spincemaille P, Wang Y. Nonlinear formulation of the magnetic field to source relationship for robust quantitative susceptibility mapping. *Magn Reson Med* 2013;69(2):467-476.

[168] Wang Z. Improving cerebral blood flow quantification for arterial spin labeled perfusion MRI by removing residual motion artifacts and global signal fluctuations. *Magnetic resonance imaging* 2012;30(10):1409-1415.

[169] Jenkinson M, Smith S. A global optimisation method for robust affine registration of brain images. *Med Image Anal* 2001;5(2):143-156.

[170] Greve DN, Fischl B. Accurate and robust brain image alignment using boundary-based registration. *Neuroimage* 2009;48(1):63-72.

[171] Ashburner J, Friston KJ. Unified segmentation. *Neuroimage* 2005;26(3):839-851.

[172] Mazziotta J, Toga A, Evans A, Fox P, Lancaster J, Zilles K, Woods R, Paus T, Simpson G, Pike B, Holmes C, Collins L, Thompson P, MacDonald D, Iacoboni M, Schormann T, Amunts K, Palomero-Gallagher N, Geyer S, Parsons L, Narr K, Kabani N, Le Goualher G, Boomsma D, Cannon T, Kawashima R, Mazoyer B. A probabilistic atlas and reference system for the human brain: International Consortium for Brain Mapping (ICBM). *Philosophical transactions of the Royal Society of London Series B, Biological sciences* 2001;356(1412):1293-1322.

[173] Deichmann R, Josephs O, Hutton C, Corfield DR, Turner R. Compensation of susceptibility-induced BOLD sensitivity losses in echo-planar fMRI imaging. *Neuroimage* 2002;15(1):120-135.

[174] Weiskopf N, Hutton C, Josephs O, Turner R, Deichmann R. Optimized EPI for fMRI studies of the orbitofrontal cortex: compensation of susceptibility-induced gradients in the readout direction. *Magma* 2007;20(1):39-49.

[175] Mazerolle EL, Ma Y, Sinclair D, Pike GB. Impact of abnormal cerebrovascular reactivity on BOLD fMRI: a preliminary investigation of moyamoya disease. *Clinical physiology and functional imaging* 2016.

[176] Uludag K, Dubowitz DJ, Yoder EJ, Restom K, Liu TT, Buxton RB. Coupling of cerebral blood flow and oxygen consumption during physiological activation and deactivation measured with fMRI. *Neuroimage* 2004;23(1):148-155.

[177] Driver ID, Wise RG, Murphy K. Graded Hypercapnia-Calibrated BOLD: Beyond the Iso-metabolic Hypercapnic Assumption. *Frontiers in neuroscience* 2017;11:276.

[178] Mulkern RV, Balasubramanian M, Mitsouras D. On the lorentzian versus Gaussian character of time-domain spin-echo signals from the brain as sampled by means of gradient-echoes: Implications for quantitative transverse relaxation studies. *Magn Reson Med* 2014.

[179] Ordidge RJ, Gorell JM, Deniau JC, Knight RA, Helpern JA. Assessment of relative brain iron concentrations using T2-weighted and T2*-weighted MRI at 3 Tesla. *Magn Reson Med* 1994;32(3):335-341.

[180] Remmele S, Sprinkart AM, Muller A, Traber F, von Lehe M, Gieseke J, Flacke S, Willinek WA, Schild HH, Senegas J, Keupp J, Murtz P. Dynamic and simultaneous MR measurement of R1 and R2* changes during respiratory challenges for the assessment of blood and tissue oxygenation. *Magn Reson Med* 2013;70(1):136-146.

[181] Ma Y, Berman AJ, Pike GB. The effect of dissolved oxygen on the relaxation rates of blood plasma: Implications for hyperoxia calibrated BOLD. *Magn Reson Med* 2016;76(6):1905-1911.

[182] Ozbay PS, Rossi C, Kocian R, Redle M, Boss A, Pruessmann KP, Nanz D. Effect of respiratory hyperoxic challenge on magnetic susceptibility in human brain assessed by quantitative susceptibility mapping (QSM). *NMR Biomed* 2015;28(12):1688-1696.

[183] Song Y, Cho G, Chun SI, Baek JH, Cho H, Kim YR, Park SB, Kim JK. Oxygen-induced frequency shifts in hyperoxia: a significant component of BOLD signal. *NMR Biomed* 2014.

[184] Baskurt OK. *Handbook of hemorheology and hemodynamics*. Amsterdam ; Washington, DC: IOS Press; 2007. x, 455 p. p.

[185] Blockley NP, Griffeth VE, Simon AB, Buxton RB. A review of calibrated blood oxygenation level-dependent (BOLD) methods for the measurement of task-induced changes in brain oxygen metabolism. *NMR Biomed* 2012.

[186] Buxton RB. *Introduction to functional magnetic resonance imaging : principles and techniques*. Cambridge ; New York: Cambridge University Press; 2009. xi , 457 p., 458 p. of plates p.

[187] Wansapura JP, Holland SK, Dunn RS, Ball WS. NMR relaxation times in the human brain at 3.0 tesla. *J Magn Reson Imaging* 1999;9(4):531-538.

[188] Driver ID, Whittaker JR, Bright MG, Muthukumaraswamy SD, Murphy K. Arterial CO2 Fluctuations Modulate Neuronal Rhythmicity: Implications for MEG and fMRI Studies of Resting-State Networks. *The Journal of neuroscience : the official journal of the Society for Neuroscience* 2016;36(33):8541-8550.

[189] Dani KA, Moreton FC, Santosh C, Lopez R, Brennan D, Schwarzbauer C, Goutcher C, O'Hare K, Macrae IM, Muir KW. Oxygen challenge magnetic resonance imaging in healthy human volunteers. *J Cereb Blood Flow Metab* 2016.

[190] Glasser MF, Coalson TS, Robinson EC, Hacker CD, Harwell J, Yacoub E, Ugurbil K, Andersson J, Beckmann CF, Jenkinson M, Smith SM, Van Essen DC. A multi-modal parcellation of human cerebral cortex. *Nature* 2016.

[191] Cohen-Adad J. What can we learn from T2* maps of the cortex? *Neuroimage* 2014;93 Pt 2:189-200.

[192] Fan AP, Bilgic B, Gagnon L, Witzel T, Bhat H, Rosen BR, Adalsteinsson E. Quantitative oxygenation venography from MRI phase. *Magn Reson Med* 2014;72(1):149-159.

[193] Uludag K, Muller-Bierl B, Ugurbil K. An integrative model for neuronal activity-induced signal changes for gradient and spin echo functional imaging. *Neuroimage* 2009;48(1):150-165.

[194] Blockley NP, Griffeth VE, Stone AJ, Hare HV, Bulte DP. Sources of systematic error in calibrated BOLD based mapping of baseline oxygen extraction fraction. *Neuroimage* 2015.

[195] He X, Yablonskiy DA. Biophysical mechanisms of phase contrast in gradient echo MRI. *Proceedings of the National Academy of Sciences of the United States of America* 2009;106(32):13558-13563.

[196] Peprah MK, Astary GW, Mareci TH, Meisel MW. Absolute magnetic susceptibility of rat brain tissue. *Magn Reson Med* 2014;72(3):876-879.

[197] Zhang J, Liu T, Gupta A, Spincemaille P, Nguyen TD, Wang Y. Quantitative mapping of cerebral metabolic rate of oxygen (CMRO2) using quantitative susceptibility mapping (QSM). *Magn Reson Med* 2015;74(4):945-952.

[198] Hallgren B, Sourander P. The effect of age on the non-haemin iron in the human brain. *J Neurochem* 1958;3(1):41-51.

[199] Sedlacik J, Boelmans K, Lobel U, Holst B, Siemonsen S, Fiehler J. Reversible, irreversible and effective transverse relaxation rates in normal aging brain at 3T. *Neuroimage* 2014;84:1032-1041.

[200] Stuber C, Morawski M, Schafer A, Labadie C, Wahnert M, Leuze C, Streicher M, Barapatre N, Reimann K, Geyer S, Spemann D, Turner R. Myelin and iron concentration in the human brain: a quantitative study of MRI contrast. *Neuroimage* 2014;93 Pt 1:95-106.

[201] Li W, Wu B, Batrachenko A, Bancroft-Wu V, Morey RA, Shashi V, Langkammer C, De Bellis MD, Ropele S, Song AW, Liu C. Differential developmental trajectories of magnetic susceptibility in human brain gray and white matter over the lifespan. *Human brain mapping* 2014;35(6):2698-2713.

[202] Zecca L, Youdim MB, Riederer P, Connor JR, Crichton RR. Iron, brain ageing and neurodegenerative disorders. *Nat Rev Neurosci* 2004;5(11):863-873.

[203] Christen T, Jahanian H, Ni WW, Qiu D, Moseley ME, Zaharchuk G. Noncontrast mapping of arterial delay and functional connectivity using resting-state functional MRI: a study in Moyamoya patients. *J Magn Reson Imaging* 2015;41(2):424-430.

[204] Kazan SM, Mohammadi S, Callaghan MF, Flandin G, Huber L, Leech R, Kennerley A, Windischberger C, Weiskopf N. Vascular autorescaling of fMRI (VasA fMRI) improves sensitivity of population studies: A pilot study. *Neuroimage* 2015.

[205] Fujiwara S, Uhrig L, Amadon A, Jarraya B, Le Bihan D. Quantification of iron in the non-human primate brain with diffusion-weighted magnetic resonance imaging. *Neuroimage* 2014.

[206] Stefanovic B, Warnking JM, Pike GB. Hemodynamic and metabolic responses to neuronal inhibition. *Neuroimage* 2004;22(2):771-778.

[207] Stefanovic B, Warnking JM, Rylander KM, Pike GB. The effect of global cerebral vasodilation on focal activation hemodynamics. *Neuroimage* 2006;30(3):726-734.

[208] Leontiev O, Buracas GT, Liang C, Ances BM, Perthen JE, Shmuel A, Buxton RB. Coupling of cerebral blood flow and oxygen metabolism is conserved for chromatic and luminance stimuli in human visual cortex. *Neuroimage* 2013;68:221-228.

[209] Liang CL, Ances BM, Perthen JE, Moradi F, Liau J, Buracas GT, Hopkins SR, Buxton RB. Luminance contrast of a visual stimulus modulates the BOLD response more than the cerebral blood flow response in the human brain. *Neuroimage* 2013;64:104-111.

[210] Moradi F, Buracas GT, Buxton RB. Attention strongly increases oxygen metabolic response to stimulus in primary visual cortex. *Neuroimage* 2012;59(1):601-607.

[211] Stefanovic B, Warnking JM, Kobayashi E, Bagshaw AP, Hawco C, Dubeau F, Gotman J, Pike GB. Hemodynamic and metabolic responses to activation, deactivation and epileptic discharges. *Neuroimage* 2005;28(1):205-215.

[212] Gauthier CJ, Madjar C, Desjardins-Crepeau L, Bellec P, Bherer L, Hoge RD. Age dependence of hemodynamic response characteristics in human functional magnetic resonance imaging. *Neurobiology of aging* 2013;34(5):1469-1485.

[213] Perthen JE, Lansing AE, Liau J, Liu TT, Buxton RB. Caffeine-induced uncoupling of cerebral blood flow and oxygen metabolism: a calibrated BOLD fMRI study. *Neuroimage* 2008;40(1):237-247.

[214] Schmithorst VJ, Vannest J, Lee G, Hernandez-Garcia L, Plante E, Rajagopal A, Holland SK, The CAC. Evidence that neurovascular coupling underlying the BOLD effect increases with age during childhood. *Human brain mapping* 2014.

[215] De Vis JB, Hendrikse J, Bhogal A, Adams A, Kappelle LJ, Petersen ET. Age-related changes in brain hemodynamics; A calibrated MRI study. *Human brain mapping* 2015;36(10):3973-3987.

[216] Mark CI, Pike GB. Indication of BOLD-specific venous flow-volume changes from precisely controlled hyperoxic vs. hypercapnic calibration. *J Cereb Blood Flow Metab* 2012;32(4):709-719.